

# RPC Science User Guide

## Version 1

- *Asked by ESA to have a common RPC user guide*
- *To include both the “default” and “enhanced” activities*
- *OK to point to technical documents (e.g., EAICD) to be provided by individual sensors*

### **TABLE OF CONTENT**

RPC SCIENCE USER GUIDE .....	1
<b>1. Brief overview of the sensors .....</b>	<b>2</b>
<b>2. Brief summary of operational modes linked to science data produced .....</b>	<b>10</b>
<b>3. Typical scientific analysis that can be performed on the data .....</b>	<b>19</b>
<b>4. Description of the data present in the PSA .....</b>	<b>36</b>
<b>5. Recommended software for visualisation/analysis of the RPC science data.....</b>	<b>47</b>
<b>6. Guide on how to process the data including calibrations to be applied .....</b>	<b>65</b>
<b>7. Example dataset time period which can be used to learn processing steps .....</b>	<b>68</b>
<b>8. List of caveats - problems with data contents, format .....</b>	<b>73</b>
<b>9. List of science papers where further information can be found .....</b>	<b>83</b>

## 1. Brief overview of the sensors

The Rosetta Plasma Consortium (RPC) includes five sensors: the Ion and Electron Sensor (IES), the Ion Composition Analyser (ICA), the Langmuir Probe (LAP), the Mutual Impedance Probe (MIP) and the Magnetometer (MAG). The joint Plasma Interface Unit (PIU) is acting as instrument control, spacecraft interface, and power management unit.

### The Ion Composition Analyzer (RPC-ICA)

RPC-ICA is an ion spectrometer with limited mass resolving capabilities operating in an energy from a few eV up to 40 keV. The instrument has a limited three-dimensional field of view covering approximately  $2\pi$  sr. RPC-ICA can distinguish between  $H^+$ ,  $He^{2+}$ ,  $He^+$ , and heavy ions of cometary origin with a mass corresponding to water group ions and above.

RPC-ICA is described in the instrument paper (Nilsson et al. 2007), though the information in that paper is somewhat outdated. The most important aspects not covered by the instrument paper are:

- The lower energy limit of RPC-ICA is a few eV, not 25 eV as stated in the instrument paper, see also (Nilsson et al., 2015a,b, Odelstad et al. 2017)
- A new way of operating the instrument was introduced during the mission, where RPC-ICA provided two-dimensional data in a restricted energy range of up to about 100 eV with a temporal resolution of 1s or 4s. These modes are described in more detail in Stenberg Wieser et al. (2017).
- In the first few month of the active mission, ICA suffered shut-offs due to high instrument temperature events, which led the team to strongly restrict the operation time of the instrument. Furthermore RPC-ICA suffered from data corruption leading to lost data and therefore intermittent data coverage. Both these aspects improved with time, so the later in the mission, the less data gaps and better coverage (Nilsson et al. 2015b, 2017).
- For low instrument temperatures, the energy scale may drift (Nilsson et al. 2017)

Working with the data is described in more detail in the RPC-ICA User Guide.

### The Ion and Electron Sensor (RPC-IES)

The IES for Rosetta is designed to measure the ion and electron flux as function of energy and direction. The instrument is an electrostatic analyzer (ESA), featuring electrostatic angular deflection to obtain a field of view of  $90^\circ \times 360^\circ$ . The instrument objective is to obtain ion and

electron distribution functions over the energy range extending from 4.32 eV/e up to 17.67 keV/e. The angular resolution for electrons is  $5^\circ \times 22.5^\circ$  (16 azimuthal and 16 polar-angle sectors). For ions the angular resolution is  $5^\circ \times 45^\circ$  (16 azimuthal and 8 polar-angle sectors) with additional segmentation to  $5^\circ \times 5^\circ$  in the  $45^\circ$  polar-angle sector most likely to contain the solar wind (giving a total of 16 polar-angle sectors for ions). The back-to-back top hat geometry of the IES electrostatic analyzer allows it to analyze both electrons and positive ions with a single entrance aperture. The IES top hat analyzers have toroidal geometry with a smaller radius of curvature in the deflection plane than in the orthogonal plane. This toroidal feature results in a flat deflection plate geometry at the poles of the analyzers and has the advantage that the focal point is located outside the analyzers rather than within them, as is the case with spherical top hat analyzers. Particles within a narrow 8% energy pass band will pass through the analyzers and be focused onto the electron and ion microchannel plates (MCPs), which produce charge pulses on 16 discrete anodes, which define the azimuth acceptance angles. In addition, the IES entrance aperture contains electrostatic deflection electrodes, which expand its elevation angle field of view to  $\pm 45^\circ$ . With the typical top hat polar-angle field of view of  $360^\circ$ , the IES acquires a total solid angle of  $2.8 \pi$  steradians.

Operation of IES is controlled by its on-board software in conjunction with sets of (selectable) look up tables. A table in one set determines the sequence of voltages applied to the electrostatic analyzer, thereby selecting the energy/charge of electrons and ions entering the sensor. Likewise, a table in another set determines the sequence of voltages applied to the deflector plates, thereby defining the acceptance angle of the particles. In the typical operating mode, for each deflector voltage chosen the ESA is stepped over its range, the deflector voltage is stepped to its next value, and so on. A complete 2-voltage sequence thus determines a complete measurement cycle. Several versions of each table are stored in the instrument so different operating modes can be easily chosen. In addition, new tables can be uploaded if desired.

During a measurement cycle the instrument obtains a full measurement of ion and electron flux within 16 azimuthal bins, 16 elevation bins and 128 energy bins, for a total of 65536 values ( $2 \times 16 \times 16 \times 128$ ) per measurement. To fit within the data volume allocated to IES, blocks of adjacent angle/energy bins are summed together. The details of this summation are mode-dependent, but this collapse and the 128 or 1024 second accumulation time are the only differences between IES operations in different modes.

Details of IES can be found in the Instrument paper by Burch et al. (Space Sci. Rev., 2007) and in the EAICD.

## The Langmuir Probe (RPC-LAP)

The purpose of the dual Langmuir probe instrument LAP is the measurement of the plasma density, electron temperature, ion flow speed, spacecraft potential and wave electric field in the plasma around comet 67P and the other targets of the Rosetta mission. Not all these quantities can be accessed at the same time, depending on instrument settings as well as on the plasma parameters.

LAP uses two spherical Langmuir probes (diameter 50 mm) mounted at the tips of the two solid booms protruding nonsymmetrically from the spacecraft (Figure X). Details of the boom mounting, including coordinates, can be found in the LAP instrument description (Eriksson et al., 2007), together with other technical documentation. The fundamental principle of a Langmuir probe is that the more charged particles there are in the plasma, the more can the probe collect, so the current flowing to the probe is proportional to the plasma density. However, as the probe currents also depend on the energy distribution in the plasma, on the applied bias voltage and on the spacecraft potential (which in turn depends on the density), the interpretation of the data is not always straightforward. It is the prime intention of the LAP sections of this document to guide a prospective user in the art of selecting the most suitable data set for the purpose at hand.

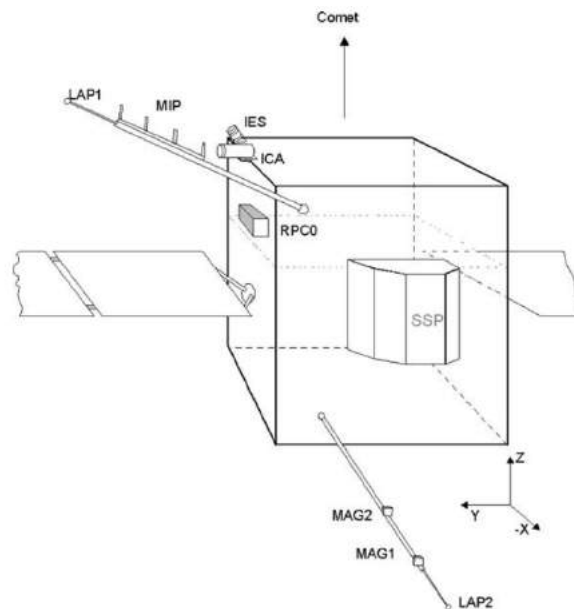


**Figure X. Mounting of the RPC sensors on the Rosetta spacecraft. The two LAP probes are seen at the boom tips.**

The LAP electronics, located inside the RPC common electronics box inside the spacecraft body, can either apply a voltage to each of the probes and measure the resulting current due to plasma particles hitting the probes (or photo- and secondary electrons leaving it), or send a bias current to the probe and measure its voltage. In bias voltage mode, the voltage can be stepped over some range from -30 to +30 V in what is known as a probe bias sweep, usually done in a few seconds at intervals which are multiples of 32 seconds (160 s being the most common). Between these

sweeps, the probes are kept at constant bias voltage, sampling the current at various rates. In an ideal case, the plasma density, electron temperature, ion flow speed, spacecraft potential and photoelectron emission can all be derived from the bias sweeps, and then the current sampled between sweeps can be used to monitor variations of the plasma density at high time resolution (Eriksson et al, 2017; Johansson et al, 2017). The range of currents that can be measured is usually  $\pm 10 \mu\text{A}$ . A low gain range was sometimes used close to perihelion, spanning  $\pm 200 \mu\text{A}$ .

The other bias mode, in which a bias current is sent to a probe and its voltage is measured, can be used to monitor the spacecraft potential at high time resolution (Odelstad et al, 2015; 2017). The spacecraft potential depends on the plasma density and can thus be used as a density proxy, with calibration to density values from other sources, like bias voltage sweeps on the other probe or (more typically) the mutual impedance probe instrument RPC-MIP (Odelstad et al, 2015; Engelhardt et al, 2018). When both probes are in this mode, the difference of their voltages equals the line integral of the electric field between them, so division by the interprobe distance of 5 m gives this component of the electric field. At lowest frequencies, this will be dominated by spurious fields induced by the spacecraft-plasma interaction. There is no firm frequency limit always applicable, but at least for floating probes (zero bias current) in the relatively dense plasma around perihelion the signal appears dominated by the real electric field in the plasma down to surprisingly (given the asymmetry of the boom mounting) low frequencies, below 1 Hz (Karlsson et al, 2017; André et al, 2017). There are no bias current sweeps implemented in the flight software, but the bias currents to the probes were a few times stepped by time-tagged commands.

The LAP electronics allow sampling of all signals at rates up to 18.75 kHz. Due to telemetry (TM) limitations, such high frequency (HF) sampling is available only in short snapshots. Low frequency (LF) sampling can be (almost) continuous, at downsampled from 57.8 Hz to fit TM availability. LAP has two TM modes: normal mode (NM, 55 bits/s) and burst mode (BM, 2.2 kbit/s). Resolution is always 16 bits in HF, but some of the LF data at 57.8 Hz have 20 bit resolution. The LAP probes could be operated independently of each other, with the limitation that simultaneous sweeps were not possible. LAP2 could be handed over to MIP for its Long Debye Length mode (LDL), useful for MIP measurements in the plasma density range 50-300  $\text{cm}^{-3}$  (CHECK WITH MIP).

Figure X shows the mounting of the LAP probes as well as the other RPC sensors on Rosetta and the coordinate axes of the s/c coordinate system. The nominal nucleus direction is indicated. To keep the solar panels orthogonal to the Sun, the solar direction is almost always perpendicular to the s/c Y axis but may vary in the X-Z plane. This means that LAP2 can sometimes come into shadow behind the spacecraft body or the high gain antenna, and LAP1 behind the solar panels.

## The Magnetometer (RPC-MAG)

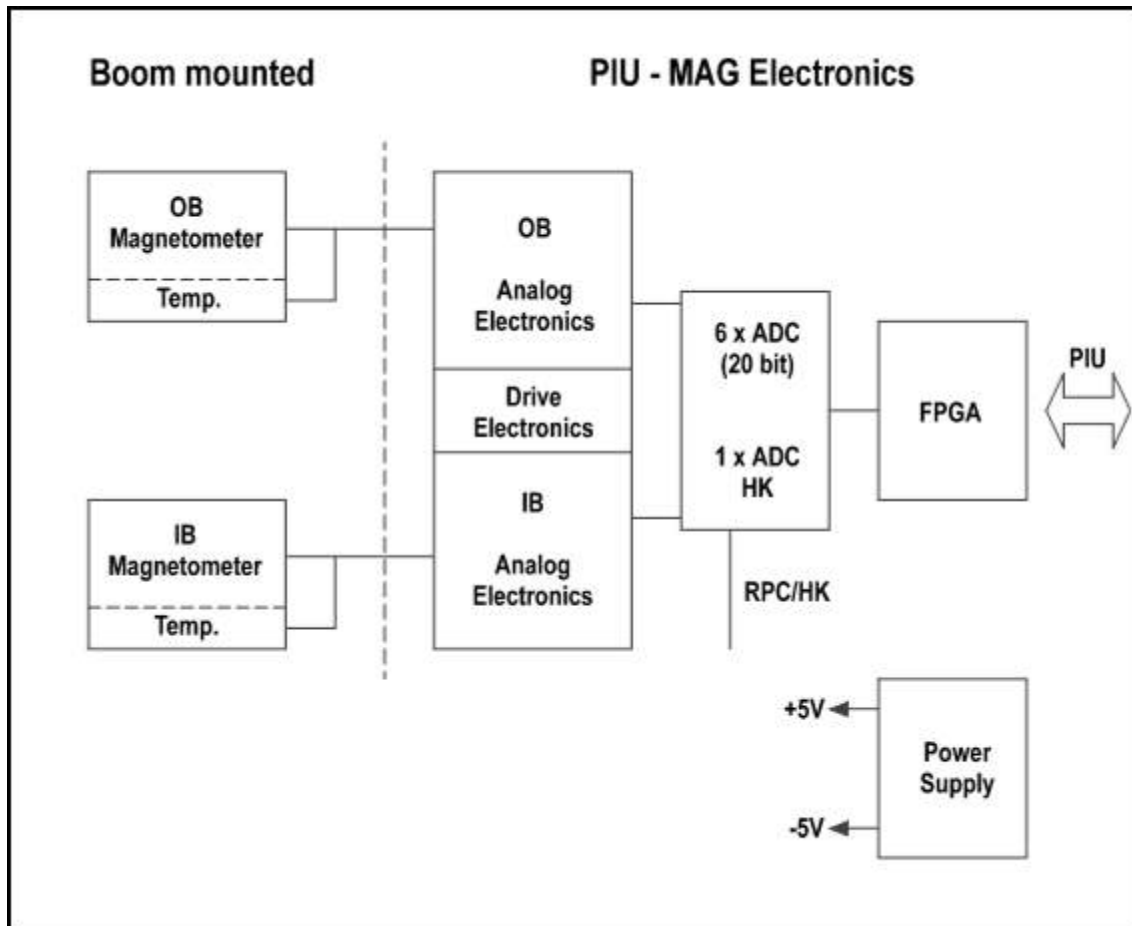
The purpose of the magnetometer is the measurement of the interplanetary magnetic field close to different targets visited by the ROSETTA spacecraft.

To measure the magnetic field, a system of two ultra light triaxial fluxgate magnetometers (about 28 g each) is used, with the outboard (OB) sensor mounted close to the tip of the about 1.55 m long spacecraft boom pointing away from s/c and with the inboard (IB) sensor on the same boom about 15 cm closer to the spacecraft body. The OB position on the boom is at 1.48m, the IB position is at 1.33m distance from the spacecraft.

In order to provide an exact timing, 6 A/D converters (one for each of the six sensor channels) are used synchronously. The A/D converters have a resolution of 20 bits each. MAG can be operated with a maximum temporal resolution of about 20 vectors/sec outboard and 1 vector/sec inboard. The raw vectors are transmitted from MAG to PIU with this constant vector rate. PIU is undersampling and filtering the raw vectors according to the current mode which is set according to the actual telemetry budget available.

RPC-MAG can be characterized by the following features:

- Fluxgate-Magnetometer with a resolution of +/- 31 pT
- Measurement Range ; +/- 16384 nT
- 2 Sensors: Outboard (OB) / Inboard (IB)
- 6 \* 20 Bit ADCs
- Measuring B-Field in 3 components with a maximum vector rate of 20 Hz.
- The temperature at Outboard and Inboard sensor is monitored in MAG housekeeping data.
- The instrument delivers time series of the 3 dimensional magnetic field vector.



**Block diagram of the RPCMAG Instrument**

More details of the RPC-MAG instrument can be found in the Instrument Paper in Glassmeier et al. (Space Sci. Rev., 2007).

### **The Mutual Impedance Probe (RPC-MIP)**

The purpose of the Mutual Impedance Probe (RPC-MIP) onboard Rosetta is to measure in situ the plasma density.

RPC-MIP is an active electric sensor that measures the transfer impedance between a transmitter (monopole or dipole) and a receiving dipole. The instrument operates at different time resolutions and in different frequency bands comprised in the [7-3500] kHz frequency range. RPC-MIP was operated either in passive mode i.e. with transmitter(s) off thus acting as a passive electric antenna, either in active mode with transmitter(s) actually triggering the surrounding plasma. In active mode, different electrodes can be used as a transmitter: two dedicated electrodes on the RPC-MIP bar can be used independently (as monopoles) or conjointly (as a dipole), such operational modes are called SDL, and the RPC-LAP probe LAP2 can also serve as a monopole transmitter, these operational modes are then called LDL. This latter mode of operations, while preventing RPC-LAP to fully operate, enables to trigger the plasma from a farther distance from

the receivers in order to access lower plasma densities than those measurable in SDL mode. Reception is always performed by the two receiving dipoles at the edges of the RPC-MIP bar mounted on the upper spacecraft boom.

Measuring the transmission properties of the electric field in the plasma enables to access some of the characteristics of the sounded plasma. From the on-ground analysis of the mutual impedance frequency spectra acquired on-board and depending on plasma conditions (among which the plasma Debye length), one may retrieve plasma bulk properties, such as the electron plasma density and potentially the electron temperature. Given the characteristic plasma conditions encountered by Rosetta and the design of the MIP sensor, while the electron density can be derived from the characteristic features of the RCP-MIP electric spectra (in particular the identification of the electron plasma frequency, upon considerations on the instrument response and hypotheses on the shape of the electron velocity distribution function), it is less straightforward to derive the electron temperature from the MIP active spectra only.

Combining measurements from different instruments, for instance RPC-MIP and RPC-LAP, enables to better constrain extra bulk plasma parameters, such as the electron temperature and the ion bulk velocity, under certain hypothesis. This is described in further details the MIP-LAP cross-calibration report [TBD].

RPC-MIP is fully described in the instrument paper Trotignon et al., 2007. Working with data is described in details in the RPC-MIP user guide.

## The Plasma Interface Unit (RPC-PIU)

The RPC consortium approach was chosen to simplify the technical interfaces between the five RPC sensors and the spacecraft whilst also minimising the overall mass and power resources. The Plasma Interface Unit (RPC-PIU) provides power-conversion and data-processing functions which are shared by all of the five sensors. PIU also provides a single-point interface to the spacecraft such that, with regard to telemetry and tele-commanding, the RPC is operated as a single instrument with multiple sub-instrument, each of which can be separately powered, controlled, and operated in numerous sensor-specific modes.

### **Technical Overview**

The Block diagram of the PIU is shown in figure TBD. Spacecraft-provided primary power (nominally +28V) is converted to regulated secondary voltages as required by the sensor units. Per sensor, each voltage line is individually controlled on/off by a switch which senses the current-draw and switches off the entire sensor unit in case of over-current. The switches are also controlled by telecommand. Thus by controlling the power-status of the sensors, the overall power consumption of the RPC can be adjusted to meet operational and scientific needs.

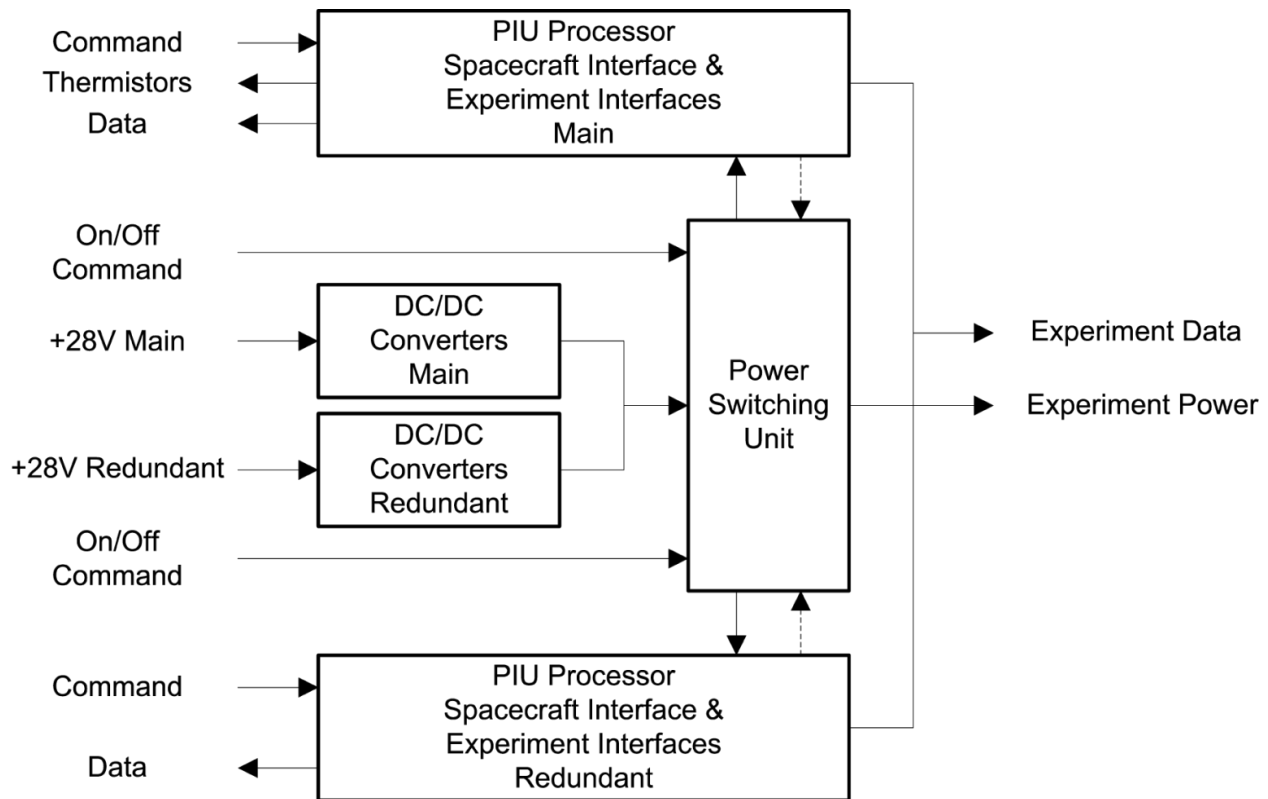


Figure TBD, block diagram for the RPC-PIU (Carr et al., 2007)

The PIU processor receives telecommands from the spacecraft on-board data-handling system and - depending on the destination 'application ID' in the packet header - either forwards the commands onto the relevant sensor for further processing, or executes the commands within the PIU. Command acknowledgements are returned to the spacecraft. The packet-services protocol is implemented within the PIU, including the patching of instrument (or PIU) onboard software. Telemetry data (housekeeping and science) received from the sensor units is assembled and formatted into packets and transmitted to the spacecraft at a 32 second cadence.

Due to the centralisation of these essential services the PIU design criterion was to avoid any single-point failure-mode propagating to (or from) more than one sensor unit. This required duplication of the power conversion and data-processing units, but not the power switches. At the commissioning of RPC the redundant power converter was tested and found to be non-operational. Consequently, the main power converter (and main data-processor) was used throughout the mission, and this failure had no operational impact.

More details on the PIU design and the consortium approach may be found in the RPC instrument paper (Carr et al., 2007).

## 2. Brief summary of operational modes linked to science data produced

### The Ion Composition Analyzer (RPC-ICA)

RPC-ICA has basically only one operational mode, It scans energy and angular space and records detection of ions of different mass. What is called a mode on ICA only relates to the on-board binning of the ion data, which is done in order to reduce the telemetry rate. The data binning is automatically adjusted so that data production stays within available telemetry limits. The data binning in burst mode could be chosen to prioritise mass or angular resolution. Once it was found out that the data corruption giving rise to data loss did not occur for the high angular resolution mode, this was mostly used from summer 2015 and onward. [Add ref to ICA user guide for instrument mode?]

Independent of the instrument mode, RPC-ICA could also be run using different on-board tables, known internally as different software versions. Of these two stand out, software versions 7 and 8. These two software versions use repeating patterns in the energy table reaching only up to about 100 eV, and fixed elevation values, to achieve two-dimensional data with 32 and 8 energy steps respectively. This corresponds to 4s and 1s temporal resolution as compared to the standard full energy range 3D distribution in 192s. Therefore software versions 7 and 8 are necessary to use when studying fast variations in the relatively low energy cometary plasma, whereas they cannot be used to study solar wind dynamics because of the limited energy and angular range. The high time resolution modes were described in Stenberg Wieser et al. (2017). An overview of the full energy and angular range data from the full mission was given in Nilsson et al. (2017). The high time resolution data was regularly used from June 2015 and onward. The ICA mode is a variable in the PSA data, and varies all the time depending on the efficiency of onboard lossless compression and available telemetry. Apart from modes prioritizing mass resolution being used up to May 2015 and thereafter mostly modes prioritizing angular resolution, the use of different modes was just determined by available telemetry, and is not related to any particular mission phases or science goals.

### The Ion and Electron Sensor (RPC-IES)

During a measurement cycle, the RPC-IES instrument obtains a full measurement of ion and electron counts by sweeping the electrostatic analyzers through 128 energy steps. Within each

energy step, the deflectors sweep through 16 elevation steps, and at each step, counts from 16 anodes are recorded simultaneously from the ion and electron detectors. The complete cycle duration may be one of four – 128 seconds, 256 seconds, 512 seconds or 1024 seconds with the integration time at each step varying with the cycle duration increases. Additional contingency modes with 96 energy steps were developed and tested in flight, but were not used for acquiring science data.

To fit within the data rates allocated to the instrument, even though data are always acquired over the complete measurement cycle, the range of energy steps for which the counts are returned may be limited. Additionally, counts acquired at discrete adjacent energy steps, elevation steps and azimuths are summed together and telemetered. The Mode ID of the cycle determines cycle duration, accumulation time, energy range and collapse, elevation range, and azimuth range, and collapse. Mode IDs have three non-zero characters and are specified for each cycle within the data files. **Details for each mode are listed as tables in DOCUMENT/IES\_MODES directory and CALIB directory which are located in any data IES folder in the RPCIES folder.** The tables list all modes used in flight including modes that were used only for commissioning and special in flight tests. Mode tables were updated during the cruise phase as well as comet phase as needs were realized. The last sets of tables were uplinked on 29 April 2015.

In Level 2 products, cycles with Mode IDs that have four non-zero characters may appear. These infrequently appearing cycles are called transition cycles and are not listed explicitly in mode tables. A transition cycle mode is constructed in-flight when IES switches from a longer duration mode to a shorter mode. It is identified by a four-character mode ID. It has the duration of the preceding longer cycle and collapse properties of the following shorter cycle.

## The LAngmuir Probe (RPC-LAP)

Most users should not have to bother about all technical details of the LAP mode concept. However, some orientation is useful to understand what data are available, to make it possible to locate time intervals with mode settings particularly useful for the problem at hand. This section therefore contains first a brief introduction to the LAP mode concept with a typical example, and then some remarks on how to find data suitable to your needs.

## LAP macros

As described above, LAP has several different kinds of “modes”, of which the main are:

- **Bias modes** for each probe (bias voltage sweeps, fixed bias voltage, or fixed bias current);
- **High or low sampling frequency range** (HF downsampled from 18.75 kHz and LF downsampled from 57.8 Hz)
- **Telemetry (TM) mode** (normal mode NM or burst mode BM)

There were additional analog settings for e.g. gain and internal calibration, and the software could be configured for various kinds of digital filtering, averaging and downsampling. For operational convenience, all these settings were handled by “macros”. These were repetitive command sequences that could be executed by time tagged command. A typical macro provided a mix of bias sweeps with data sampled quasi-continuously between sweeps at low frequency (LF, often 57.8 Hz in BM or 0.9 Hz in NM) and in very short snapshots at high sampling frequency (HF, usually 18.75 kHz). The most common repetition rate was 160 s, making this the typical time between sweeps and HF snapshots. New macros were uploaded to the instrument as new plasma environments were encountered or particular needs arose. All macros are described in the macro table distributed with the LAP documentation in the ESA PSA archive. Each macro is identified by a 3-digit string, e.g. 802, 805 and 914 which we will take as examples below.

Figure FF1 shows an overview of the LAP data collected on Nov 6, 2015. Three different macros were used on this day, providing different data as detailed in Table TT1:

- ❑ 00:00 - 04:00: Macro 802, with both LAP probes floating (zero bias current) and their voltages measured at 57.8 samples/s (32 s averages in panel A). No bias voltage sweeps, so panels D and E are blank. Spectra of the brief snapshots of data sampled at 18.75 kHz are shown in panels F and G. From these data, the **spacecraft potential** can be inferred from the measured probe voltages (Odelstad et al, 2017) and **electric wave fields** from their difference (Karlsson et al, 2017, André et al 2017). The spacecraft potential can in turn be used to derive a **plasma density** estimate (Odelstad et al, 2015), though it is likely MIP has good data here and then it may be more fruitful to use the MIP data for an absolute measure of the plasma density and use the LAP potentials for interpolating this to higher time resolution (Heritier et al, 2017).
- ❑ 04:00 - 06:00: Macro 805, in which LAP2 is handed over to MIP for use in its LDL mode, so there are LAP data only for from LAP1. This probe is at -20 V bias potential (panel A) for sampling ions, and the resulting current is seen in panel B. The bias sweeps are shown in panel D and the spectrum of the short HF snapshots in panel F. The sweeps are used to derive **plasma density**, **electron temperature** and **spacecraft potential** (Eriksson et al, 2017) as well as the **photoemission current** (Johansson et al, 2017), while the ion current in between can be used to follow the **plasma density variations** at high time

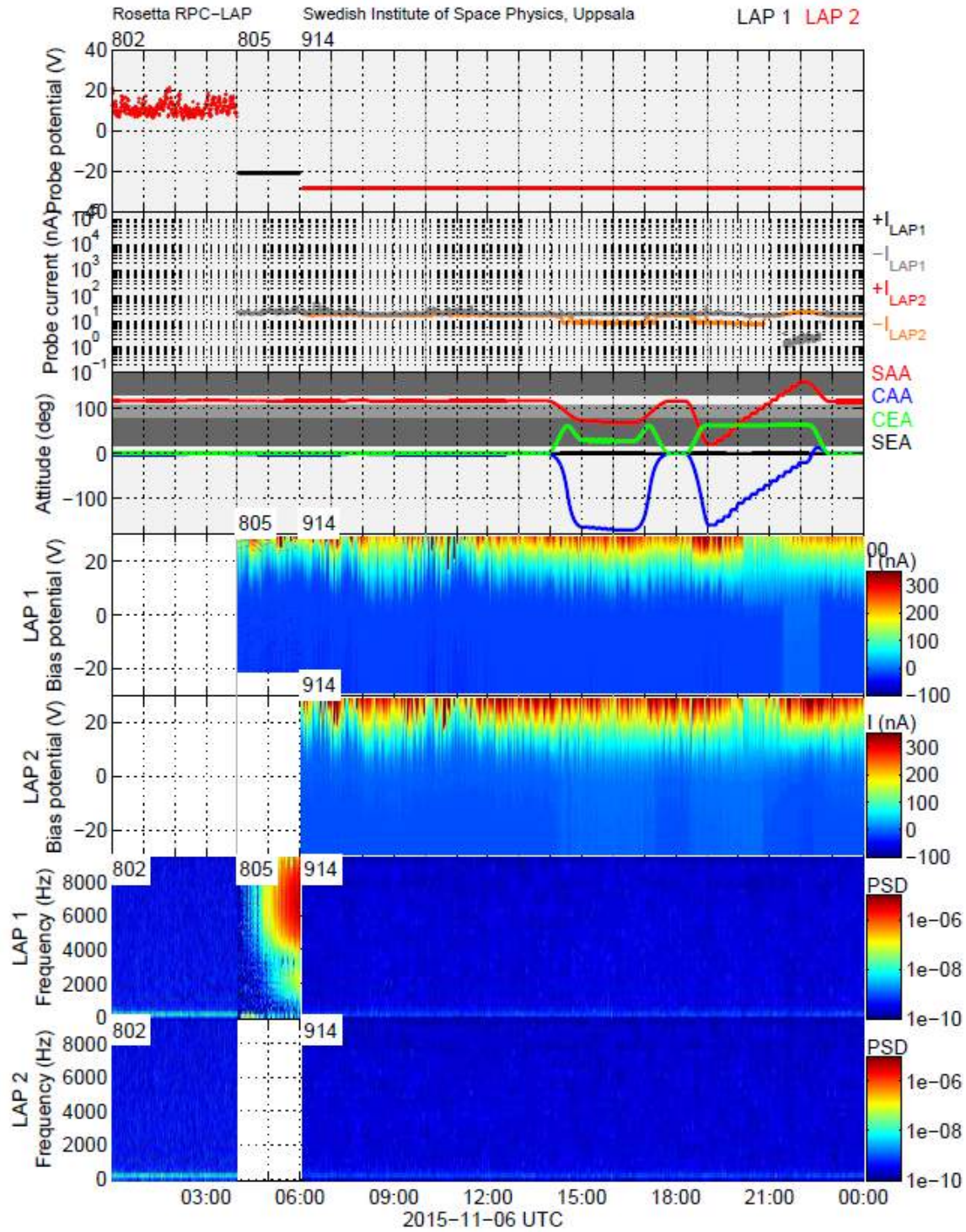
resolution after calibration to density values from sweeps and/or MIP (Engelhardt et al, 2018). However, as this is a normal mode (NM) macro, the time resolution is only 0.9 s. For this macro, the HF data in panel F show lots of MIP interference (typical for LDL modes), and in addition each snapshot is short: only 160 samples, so other modes are more suitable for the study of waves above 20 Hz.

- ❑ 06:00 - 24:00: Macro 914, with both LAP probes at -27 V (panel A), sampling the probe current at 57.8 Hz between the bias sweeps, which are shown in panels D and E. The spectra of the short HF snapshots are shown in panels F and G. The sweeps and the probe current at fixed bias voltage obtained between them can be used to derive **plasma density, electron temperature, spacecraft potential** and **photoemission current** as for macro 805 above. The HF data are useful for **wave studies** (Gunnell et al, 2016, 2017).

How to find intervals with a LAP mode suitable for your needs

Table TT2 summarizes some restrictions on LAP operations modes for given science needs. Note that the MIP column does not mean you need to check the MIP mode: the important issue is if MIP is in LDL or not, and this is clear from the LAP macros. Several restrictions can apply for any given scientific purpose.

When you have identified constraints on LAP operations, you can check in the LAP macro table in the PSA/PDS documentation which macros satisfy these requirements. You can then look at the table of LAP macro usage in the LAP operations reports (in the PSA/PDS documentation) to find intervals where these macros are used, and then turn to the data.



Archive version: RO-C-RPCLAP-5-1511-DERIV-V0.7

Plot date: 01-Dec-2017 13:16

**Figure FF1.** Overview of LAP data obtained on Nov 6, 2015. Panels from top to bottom: (A) Probe voltages, bias or measured. (B) Probe currents, bias or measured. (C) Relevant s/c attitude angles. (D) and (E) Probe bias sweeps. (F) and (G) Spectra of HF snapshots.

**Table TT1.** Excerpt from the LAP macro table, distributed with the LAP PSA/PDS archives, detailing the operations of the three macros run on 2015-11-06 (Figure FF1).

Macro ID	0x802	0x805	0x914
Purpose	Vsc, HF	LDL,N,HF,swp	N, HF, swp
TM mode	BM	NM	NM
Bias mode	EE	N-	NN
Fix bias LAP1	float	-20 V	-30 V
Fix bias LAP2	float	n/a	-30 V
<b>LF quasi-continuous data</b>			
Sampled data	V1, V2	I1	I1, I2
Downsampling	1	64	1
fsamp [Hz]	57.8	0.9	57.8
Bits/sample transmitted	16	20	16
Samples per 32s per probe	1798	28	1798
<b>HF snapshots</b>			
Sampled data	V1, V2	I1	I1, I2
fsamp [Hz]	18750	18750	18750
Samples	432	160	1600
Cadency [s]	32	160	160
<b>Sweeps</b>			
Probes	n/a	LAP1	LAP1, LAP2
Cadency [s]	n/a	160	160
Range [V]	n/a	[-22, 30]	[-30, +30]
Step [V]	n/a	0.25	0.25
Number of steps	n/a	208	240
Sweep duration [s]	n/a	1.47	3.37

**Table TT2.** Restrictions on LAP operational modes for particular science purposes.

Need	Restrictions on macros/operational modes			
	TM	Bias	MIP	Notes
High time resolution (50 ms - 2 s)	BM			Same for E-field or density
LF E-field (below 20 Hz)		Both probes in E-field mode (floating or bias current)	SDL	Both probes needed, so MIP cannot use LDL.
HF (kHz range)	BM preferred		SDL preferred	Longer snapshots in BM. MIP interference in LDL.
Two-probe measurements			SDL	Both probes needed, so MIP cannot use LDL.
Electron temperature (eV range, timescale of minutes)	BM preferred	Sweeps (LAP1 preferable)		Sweeps in BM often have better voltage resolution and larger range as more TM is available. LAP2 more often shows effects of wake, shadowing and contamination
Electron density (timescale of minutes)	BM preferred	Sweeps (LAP1 preferable)		LAP2 more often shows effects of wake, shadowing and contamination
Spacecraft potential (timescale of minutes)	BM preferred	Sweeps		Requires probe is illuminated to identify photo-emission knee
Spacecraft potential (higher time resolution)		At least one probe in E-field mode (floating or bias current)		Probe potential is approximately $-V_s$ .
LF (0.1 s to minutes) density fluctuations in tenuous plasmas (up to few hundreds $\text{cm}^{-3}$ )		At least one probe with positive $V_{\text{bias}}$ (LAP1 preferred)		To sample electrons, as ion current is low at low density
LF (0.1 s to minutes) density fluctuations in dense plasmas (above a few 100 $\text{cm}^{-3}$ )		At least one probe with negative $V_{\text{bias}}$		To sample ions, as electron current is sensitive to changing $V_s$ in dense plasmas

## The Magnetometer (RPC-MAG)

The magnetometer is a simple instrument in terms of modes. There are two sensors, the inboard sensor IB and the outboard sensor OB, which are sampled with different sample rates.

All possible operational modes are listed in the table below. Although there are 6 science modes we only used the **NORMAL** mode (SID2) and the **BURST** mode (SID3) during the scientific phases of the mission. This means that the data of the OB sensor are available at a vector rate of 1 Hz (normal mode) or 20 Hz (burst mode). Accordingly the IB data are sampled with 1/32 Hz and 1 Hz respectively.

The modes are reflected in the filenames of our data products. Thus a "M2" in the filename means NORMAL mode data and M3 designates BURST mode data. There is always one data file per sensor per day per mode (if data are available). This means that data files can contain data gaps if mode switches have occurred. If e.g. the instrument was in NORMAL mode from 07:00 - 09:00 and from 13:00 - 24:00 and in BURST mode from 04:00-07:00 and from 09:00 - 13:00 then the NORMAL mode file contains a gap from 09:00- 13:00, whereas the BURST mode file has a gap from 07:00-09:00. All data are there, but they are written to different files in order to avoid mixing different sampling rates and getting wrong results in spectral analyses.

The OB sensor is always sampled with the higher sample rate as this sensor is located further out and should be the one suffering less s/c noise.

Table T3: Summary of modes used in MAG, where the prime operational modes are SID2 and SID3.

<b>Mode</b>	<b>Sample Rate</b>	<b>Vector Rate</b>	<b>Name</b>
SID 1 SCIENCE	1/32 Hz	0.03125 vec/s 0.000976 vec/s	Minimum Mode
SID 2 SCIENCE	1 Hz	1 vec/s 0.03125 vec/s	Normal Mode
SID 3 SCIENCE	20 Hz	20 vec/s 1 vec/s	Burst Mode
SID 4 SCIENCE	5 Hz	5 vec/s 0.033125 vec/s	Medium Mode
SID 5 SCIENCE	¼ Hz	0.25 vec/s 0.007812 vec/s	Low Mode
SID 6 SCIENCE	20 Hz	20 vec/s 0.0625 vec/s	Test Mode
HK	1280 Hz Internal		House Keeping

## The Mutual Impedance Probe (RPC-MIP)

The RPC-MIP instrument can operate in active mode (when transmitting) or in passive mode (no transmission).

- in active mode, a sinusoidal signal is transmitted through one or two electrodes at a given frequency while the potential difference is acquired simultaneously on the dedicated receiving electrodes pair and Fourier transformed at the same frequency as the transmission (through a DFT). Several different transmitting frequencies are then scanned following a frequency table, previously chosen by telecommand. The resulting electric spectra (amplitude and phase) are then fully or partly transferred to data packets.

Several transmitting configurations have been implemented:

- dipole transmission in phase on both RPC-MIP transmitters
- dipole transmission in phase opposition on both RPC-MIP transmitters
- monopole transmission on one of the RPC-MIP transmitters
- monopole transmission on RPC-LAP probe LAP2

Active mode with RPC-MIP electrodes transmitting are referred as SDL (Short Debye Length) modes. Active mode with RPC-LAP probe LAP2 transmission are designated as LDL (Long Debye Length). In SDL mode, the physical length of the RPC-MIP bar prevents from measuring plasma density in plasmas with Debye lengths larger than ~50 cm. The LDL mode has been designed to overshoot this limit and access smaller densities.

- in passive mode, no signal is injected and the measured potential difference is processed on-board by a FFT, then obtaining an amplitude spectrum over the whole bandwidth at a 7 kHz frequency resolution. As in active mode, full or part of the information is transmitted to data packets.

Active and passive sub-modes have been designed to adapt on allowed resources or scientific strategies. They result in transferring full or part of the acquired spectra in the telemetry packets and are combined to construct an RPC-MIP sequence with a fixed duration of 32 s (PIU cycle) and a data volume depending on the telemetry mode. A complete description of RPC-MIP sequences, modes and sub-modes is given in the RPC-MIP user guide.

The frequency range of the RPC-MIP instrument depends on the operating mode. In **LDL**, spectra are acquired over the [7 - 168] kHz interval while in **SDL**, spectra can be acquired on several frequency tables, the larger frequency range being [28 - 3472] kHz. The frequency table is selected by telecommand. This results in a working frequency range that can vary with time (i.e. when changing operating parameters). To prevent users from having a precise knowledge of the instrument operating concepts and parameters, RPC-MIP spectra are always given with the corresponding frequency values in the data files available at PSA. The available frequency tables in the different modes (passive, active: SDL and LDL) are given in the RPC-MIP user guide.

As different sub-modes can be combined in different ways to construct fixed-length sequences, some idle periods can exist within a RPC-MIP sequence. This leads to an irregular time resolution that depends on telemetry mode and RPC-MIP operational parameters. Typical values for time resolution for different sub-modes are given in Table T4:

Table T4: RPC-MIP operational sub-modes and associated time resolution.

	normal TM rate	burst TM rate
survey full	32 s	~4.4 s
ldl full	~10.6 s	~2.6 s
passive full	32 s	~4.4 s

All the RPC-MIP operational parameters are described in the RPC-MIP user guide and can also be found in dedicated files of the PSA archive (RPCMIPS3XXX<date>.TAB).

### 3. Typical scientific analysis that can be performed on the data

#### The Ion Composition Analyzer (RPC-ICA)

##### *Measurements of solar wind ions*

RPC-ICA can be used to study solar wind ions and how they are affected by the comet environment. This is in particular described in a series of papers (Behar et al. 2016a,b, 2017) describing the solar wind deflection. Even though significantly deflected, the solar wind mostly forms a well defined beam, and calculating velocity moments is usually straightforward even though one must take the limited field of view into account. ICA can resolve H<sup>+</sup>, He<sup>++</sup> and He<sup>+</sup>. The density can typically also be well determined.

##### *Estimates of the neutral atmosphere*

Charge exchange of He<sup>2+</sup> to He<sup>+</sup> allows for studies of the neutral atmosphere (Nilsson et al. 2015a, Simon Wedlund et al. 2016, Hansen et al. 2016) as the He<sup>+</sup> to He<sup>++</sup> ratio is a measure of the integrated atmospheric density the He<sup>++</sup> ions has passed through.

##### *Measurements of cometary ions*

RPC-ICA can also be used to study cometary ions and how they are affected by the solar wind and other phenomena. The first pick up detection of ions was described in Nilsson et al. (2015a) with further descriptions of the cometary ion flow directions shown in Nilsson et al. (2015b, 2017). The latter studies established that most observed ions have a significant anti-sunward component. The relation between cometary and solar wind ion flow was described in a case study Behar et

al. (2016a), whereas Berčić et al. (2018) described how cometary ions at low energy and observed relatively close to the nucleus were expanding radially in the  $Y_{\text{CSEQ}} - Z_{\text{CSEQ}}$  plane, while more energetic pick-up ion motion in the same plane was controlled by the solar wind electric field direction. Both ion populations had a significant anti-sunward motion. In another study, Nicolaou et al. (2017) studied energy-angular dispersion of cometary ions, and found that these only sometimes were consistent with a gyration of the ions. In other cases they suggested that inhomogeneity of the electric and magnetic fields along the particle orbit could give rise to the observed dispersion.

#### *Studying fast changes in the unstable cometary environment*

High time resolution data from RPC-ICA can also shed light on variations in the spacecraft potential (Stenberg Wieser et al. 2017, Odelstad et al. 2017) and other fast variations in the comet environment. Frequently a co-variation between magnetic field strength, plasma density as determined from the LAP or MIP instruments and ion fluxes as observed by RPC-ICA can be observed (Stenberg Wieser et al. 2017).

#### *Density at low energy*

Measurements of low energy ions are affected by the spacecraft potential, by the lower limit of the energy range of RPC-ICA and by the restricted angular coverage of the instrument at low energy. Therefore studies of low energy ions represents a special challenge. Flow directions are almost certainly strongly affected by the spacecraft potential when the ion energy and the spacecraft potential are in the same range.

## The Ion and Electron Sensor (RPC-IES)

### **Accessing the IES data**

IES data are accessible from both the ESA (PSA) and NASA (PDS) web sites.

There is an electron and an ion data file for each day, e.g.:

**RPCIES2016245\_ELC\_V3.TAB for L2**

**RPCIES2016245\_L3ELC\_FLUX\_V1.TAB for L3**

are electron files for the day 1 Sept. 2016, which can be found at:

<ftp://psa.esac.esa.int/pub/mirror/INTERNATIONAL-ROSETTA-MISSION/RPCIES/>

These files can be read directly with any favorite software (e.g. IDL) to produce other products, such as energy distribution plots.

## IES Data Illustrations

All data files are in columns of ASCII (See EIACD)

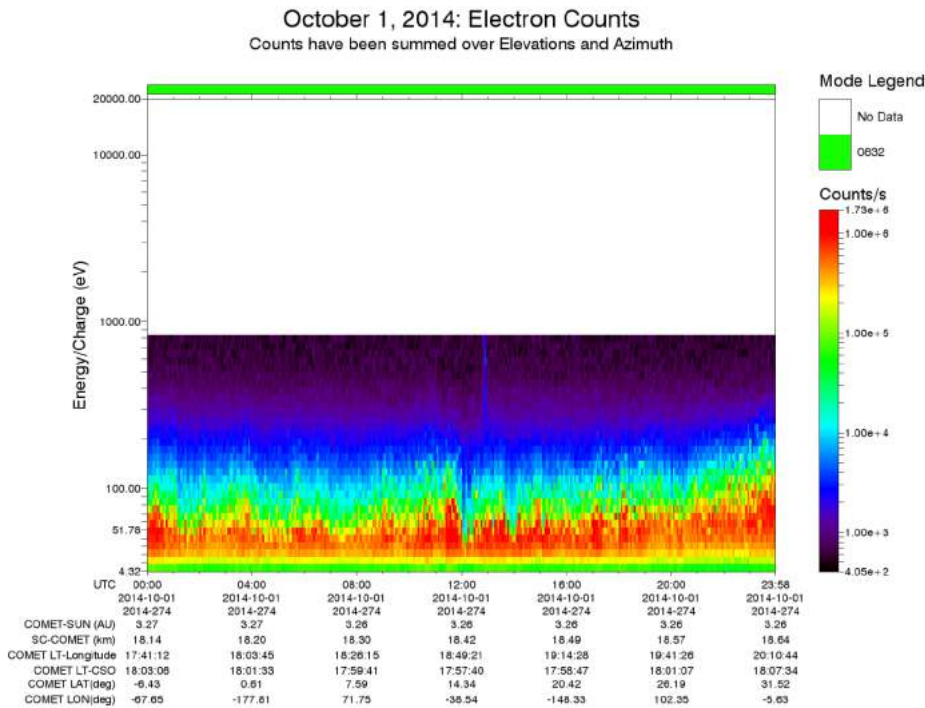
L2: ion and electron counts/s

L3: ion and electron differential energy flux

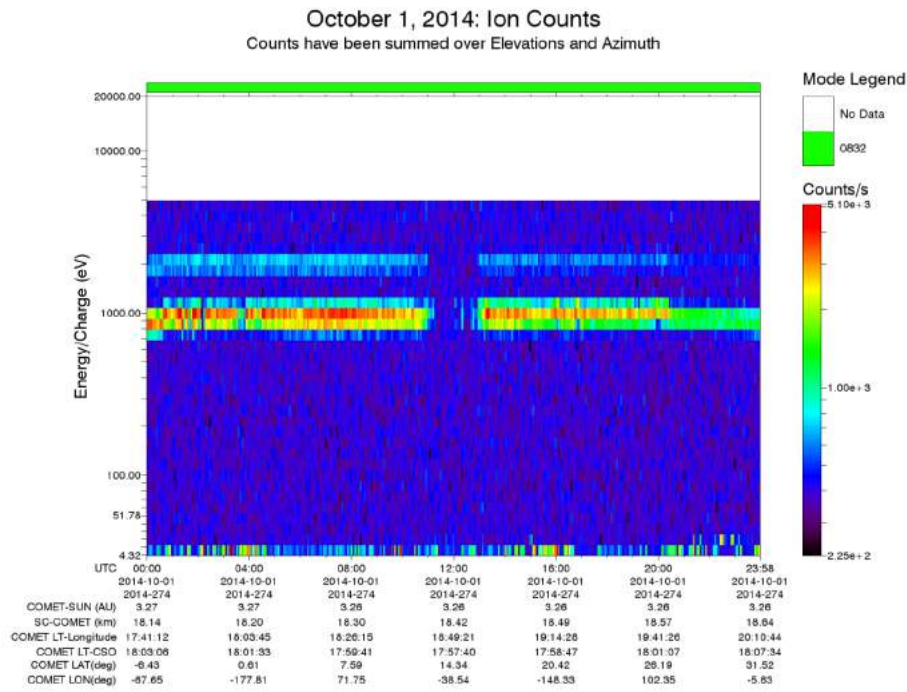
The columns are (Left to Right):

UTC, Mode, Start energy step, stop energy step, start elevation angle step, end elevation angle step, azimuthal angle 00...to 15, quality flags.

Examples of energy-time spectrograms for electrons and ions measured by IES on 1 Oct 2014 are shown here.



Generated by IES v2.6.11.0007 on Thu Feb 16 2017 (21:04:47) at 00:26:12



Generated by IES 08 v2.5 (1/0007) on Thu Feb 16, 2017 03:17:09 (UTC) at 00:26:50

See also the IES discussion in Section 7.

Examples of the results of analysis can be found in the following published papers:

**Relevant publications:**

Broiles, T. W. et al., (2015). Rosetta observations of solar wind interaction with the comet 67P/Churyumov-Gerasimenko. *Astronomy & Astrophysics*, 583, A21, doi: 10.1051/0004-6361/201526046.

It is shown that the solar wind is strongly deflected in the weak coma. The average ion velocity slows from the mass loading of newborn cometary ions, which also slows the interplanetary magnetic field (IMF) relative to the solar wind ions and subsequently creates a Lorentz force in the frame of the solar wind. The Lorentz force in the solar wind frame accelerates ions in the opposite direction of cometary pickup ion flow, and is necessary to conserve momentum.

Burch, J. L. et al., (2015), Charge exchange in cometary coma: Discovery of H<sup>-</sup> ions in the solar wind close to comet 67P/Churyumov-Gerasimenko, *Geophys. Res. Lett.*, 42, 5125–5131, doi:10.1002/2015GL064504.

As Rosetta was orbiting Comet 67P/Churyumov-Gerasimenko, the Ion and Electron Sensor detected negative particles with angular distributions like those of the concurrently-measured

solar-wind protons but with fluxes of only about 10% of the proton fluxes and energies of about 90% of the proton energies. Using well-known cross sections and energy-loss data, it is determined that the fluxes and energies of the negative particles are consistent with the production of H<sup>-</sup> ions in the solar wind by double charge exchange with molecules in the coma.

Clark, G. et al. (2015), Suprathermal electron environment of comet 67P/Churyumov-Gerasimenko: Observations from the Rosetta Ion and Electron Sensor, *Astron. Astrophys.*, 583, A24, doi:10.1051/0004-6361/201526351.

In this study, using data from the Rosetta Ion and Electron Sensor, we characterize the suprathermal electron environment around comet 67P/Churyumov-Gerasimenko between 2.5-3.5 AU. We find that the solar-wind interaction with comet 67P is stronger than expected at large heliocentric distances, especially for such a weakly outgassing comet, and is highly turbulent.

Goldstein, R. et al. (2015). The Rosetta Ion and Electron Sensor (IES) measurement of the development of pickup ions from comet 67P/Churyumov-Gerasimenko, *Geophys. Res. Lett.*, 42, 3093–3099, doi: 10.1002/2015GL063939.

On 19 August, when Rosetta was ~80 km from the comet 67P/Churyumov-Gerasimenko, which was ~3.5 AU from the Sun, IES began to see ions at its lowest energy range, ~4–10 eV. We identify these as ions created from neutral species emitted by the comet nucleus, photoionized by solar UV radiation in the neighborhood of the Rosetta spacecraft (S/C), and attracted by the small negative potential of the S/C resulting from the population of thermal electrons. Later, IES began to see higher-energy ions that we identify as having been picked up and accelerated by the solar wind

Goldstein, R. et al. (2017). Two years of solar wind and pickup ion measurements at Comet 67P/Churyumov-Gerasimenko, *MNRAS* 469, S262–S267, doi:10.1093/mnras/stx1571.

Within a month after comet arrival, while Rosetta was <100 km from CG, we began to observe low-energy (<20 eV) positive ions. We believe that these are newly formed from cometary neutrals near Rosetta and attracted to the negative spacecraft (S/C) potential. These ions were in the early phase of pickup and had not yet reached the energy they would after at least one full gyration about the magnetic field. As CG increased its activity the flux and energy of the measured pickup ions increased intermittently while the solar wind appeared intermittently as well. By about the end of April 2015 the solar wind had become very faint until it eventually disappeared from the IES field of view. We then began to see ions at the highest energy levels of IES, >10 keV for a few days then intermittently through the remainder of the mission, but lower energy ( few keV) pickup ions were also observed.

Madanian, H. et al. (2016), Suprathermal electrons near the nucleus of comet 67P/Churyumov-Gerasimenko at 3 AU: Model comparisons with Rosetta data, *J. Geophys. Res. Space Physics*, 121, doi:10.1002/2016JA022610.

This paper reports on electron energy spectra measured by IES near the nucleus as well as approximate densities and average energies for the suprathermal electrons when the comet was at a heliocentric distance of about 3 AU. Comparisons are made with electron densities measured by other instruments; IES-derived electron densities are found to be significantly lower than and anti-correlated to those observed by LAP and MIP. Reasons behind the differences are discussed.

Mandt, K. E. et al. (2016), RPC observation of the development and evolution of plasma interaction boundaries at 67P/Churyumov-Gerasimenko, *MNRAS*, 2016, 462, S9, doi:10.1093/mnras/stw1736

Observations made between April 2015 and February 2016 show that solar wind-cometary plasma interaction boundaries and regions formed around mid-April 2015 and lasted through early January 2016. At least two regions were observed, separated by a boundary. The inner region was located on the nucleus side of the boundary and was characterized by low energy water-group ions, reduced magnetic field pileup and enhanced electron densities. The outer region was located outside of the boundary and was characterized by reduced electron densities, water-group ions that are accelerated to energies above 100 eV and enhanced magnetic field pileup compared to the inner region.

## The Langmuir probe instrument (RPC-LAP)

### Low time resolution measurements of plasma density and electron temperature

These fundamental quantities can be derived from the LAP bias voltage sweeps, typically performed every 160 s in most operational modes but sometimes more often. Much discussion of this method can be found in Eriksson et al (2017). It has also been used e.g. by Edberg et al (2015) for plasma density profiles close to the nucleus, by Vigren et al (2016) for modeling the early activity phase and by Yang et al (2016) for the first activity of the comet.

It should be noted that plasma density values can also be obtained from MIP, ICA and IES. The relation between the various RPC plasma density values is discussed in Section 4.

### High time resolution measurements of plasma density variations

The LAP measurements of probe currents in between sweeps, or of probe voltage when the probes are in bias current (E-field) mode, can be used to follow the plasma density variations at high time resolution (up to 57.8 samples/s). Calibrations to LAP sweeps, MIP density values or assumptions on particle energy (electron temperature or ion drift speed and composition) are needed for converting these to plasma densities. This has been used by e.g. Heritier et al (2017, using probe voltages) and Engelhardt et al (2018, using voltages and currents) at the comet, and by Edberg et al (2009, using voltages) at the Rosetta Mars flyby.

### Measurement of ion energy/flow speed

The Langmuir probe bias voltage sweeps can be used to derive the ratio of ion density to ion momentum. With density either from the electron side of the sweep or from MIP and with an assumption on ion mass, an effective ion speed can be derived, combining bulk and thermal motion. This has been done by Vigren et al (2017) and Odelstad et al (2018).

### Measurements of low frequency E-fields

With two probes in E-field mode, measuring voltage at fixed bias current (which at the comet mostly was zero, i.e. floating probes), the electric field between them can be derived. The use of this for LF data (approximately 1 Hz - 20 Hz) is described by Karlsson et al (2017) and André et al (2017).

### Measurements of high frequency E-fields

At sufficiently high frequency, the current to a probe will be dominated by the displacement current due to the capacitive coupling of the probe to the plasma. This means that even if the probe has a bias voltage applied so that the probe current is the quantity sampled, it is the wave electric field which is measured. This has been used to study ion acoustic waves to kHz frequencies by Gunnell et al (2016, 2017).

### Measurements of spacecraft potential

This can be derived at a time resolution of minutes from the probe bias sweeps, or to fractions of a second by use of a probe in E-field mode. The fundamental reference here is Odelstad et al (2017), who also compare and cross-calibrate these data to ICA measurements. The spacecraft potential can provide information on plasma density (Odelstad et al, 2015; 2017) but also be used for interpreting and calibrating particle data (e.g. Galand et al, 2017; Heritier et al, 2017).

### Probe photoelectron emission

The photoelectron saturation current depends on the EUV flux, and thus is of interest also for understanding ionization in the coma. Its measurement is discussed in detail, including validation by several different methods, in Johansson et al (2017).

## The Magnetometer (RPC-MAG)

### Analysis of Magnetometer Data

The magnetometer delivers timeseries of the magnetic field vector data. All the scientific usable data (data in celestial coordinates like ECLIPJ2000 or CSEQ) contain the actual position of the s/c and the measured 3-component magnetic field vector. Basic magnetic field analyses are

- plotting of the timeseries,
- filtering using suitable filters (Low pass, Band pass, High pass)
- spectral analyses e.g., computation of Power Spectral density, dynamic spectra, cross spectral density using IB, OB and possible ROMAP Lander data)
- minimum variance analyses (in order to study wave properties)
- plotting hodographs (to investigate polarization phenomena)
- compare IB and OB signatures (to assess s/c disturbance and extract external field effects)
- comparing data with simulations
- reconstructing s/c attitudes using magnetic field data measured onboard two different spacecraft under the assumption of equal signatures.

The following list shows examples of published papers using, analyzing and interpreting RPC-MAG magnetic field data.

### Relevant publications:

#### ***The nonmagnetic nucleus of comet 67P/Churyumov-Gerasimenko***

Auster, H.-U. et al. Science,349,2015

*Knowledge of the magnetization of planetary bodies constrains their origin and evolution, as well as the conditions in the solar nebular at that time. Based on magnetic field measurements during the descent and subsequent multiple touchdown of the Rosetta lander Philae on the comet 67P/Churyumov-Gerasimenko, we show that no global magnetic field was detected within the limitations of analysis. The ROMAP suite of sensors measured an upper magnetic field magnitude of less than 2 nT at the cometary surface at multiple locations with the upper specific magnetic moment being  $< 3.1 \cdot 10^{-5} \text{ Am}^2/\text{kg}$  for meter-size homogeneous magnetized boulders. The maximum dipole moment of 67P/Churyumov-Gerasimenko is  $1.6 \cdot 10^8 \text{ Am}^2$ . We conclude that on the meter-scale, magnetic alignment in the pre-planetary nebula is of minor importance.*

## **Attitude reconstruction of ROSETTA's Lander PHILAE using two-point magnetic field observations by ROMAP and RPC-MAG**

Heinisch, P. et al. Acta Astronautica,125,2016

*As part of the European Space Agency's ROSETTA Mission the Lander PHILAE touched down on comet 67P/Churyumov–Gerasimenko on November 12,2014. The magnetic field has been measured on board the orbiter and the lander. The orbiter's triaxial fluxgate magnetometer RPC-MAG is one of five sensors of the ROSETTA Plasma Consortium. The lander is also equipped with a tri-axial fluxgate magnetometer as part of the ROSETTA Lander Magnetometer and Plasma-Monitor package (ROMAP). This unique setup makes a two point measurement between the two spacecraft in are relatively small distance of less than 50 km possible. Both magnetometers were switched on during the entire descent, the initial touchdown, the bouncing between the touchdowns and after the final touchdown. We describe a method for attitude determination by correlating magnetic low-frequency waves, which was tested under different conditions and finally used to reconstruct PHILAE's attitude during descent and after landing. In these cases the attitude could be determined with an accuracy of better than  $\pm 5^\circ$ . These results were essential not only for PHILAE operations planning but also for the analysis of the obtained scientific data, because nominal sources for this information, like solar panel currents and camera pictures could not provide sufficient information due to the unexpected landing position.*

## **First detection of a diamagnetic cavity at comet 67P/Churyumov-Gerasimenko**

Goetz, C. et al. A&A,588,2016

Context: The Rosetta magnetometer RPC-MAG has been exploring the plasma environment of comet 67P/Churyumov-Gerasimenko since August 2014. The first months were dominated by low-frequency waves which evolved into more complex features. However, at the end of July 2015, close to perihelion, the magnetometer detected a region that did not contain any magnetic field at all. Aims: These signatures match the appearance of a diamagnetic cavity as was observed at comet 1P/Halley in 1986. The cavity here is more extended than previously predicted by models and features unusual magnetic field configurations, which need to be explained.

Methods: The onboard magnetometer data were analyzed in detail and used to estimate the outgassing rate. A minimum variance analysis was used to determine boundary normals.

*Results:* Our analysis of the data acquired by the Rosetta Plasma Consortium instrumentation confirms the existence of a diamagnetic cavity. The size is larger than predicted by simulations, however. One possible explanation are instabilities that are propagating along the cavity boundary and possibly a low magnetic pressure in the solar wind. This conclusion is supported by a change in sign of the Sun-pointing component of the magnetic field. Evidence also indicates that the cavity boundary is moving with variable velocities ranging from 230 - 500m/s.

### **Observation of a new type of low frequency waves at comet 67P/Churyumov-Gerasimenko**

Richter, I et al. Ann. Geophys, 33, 2015

*We report on magnetic field measurements made in the innermost coma of 67P/Churyumov-Gerasimenko in its low-activity state. Quasi-coherent, large-amplitude ( $\delta B/B \sim 1$ ), compressional magnetic field oscillations at 40 mHz dominate the immediate plasma environment of the nucleus. This differs from previously studied cometary interaction regions where waves at the cometary ion gyrofrequencies are the main feature. Thus classical pickup-ion-driven instabilities are unable to explain the observations. We propose a cross-field current instability associated with newborn cometary ion currents as a possible source mechanism.*

### **Mass-loading, pile-up, and mirror-mode waves at comet 67P/Churyumov-Gerasimenko**

Volwerk, M. et al. Ann. Geophys., 34, 2016, <https://doi.org/10.5194/angeo-34-1-2016>

*The data from all Rosetta plasma consortium instruments and from the ROSINA COPS instrument are used to study the interaction of the solar wind with the outgassing cometary nucleus of 67P/Churyumov-Gerasimenko. During 6 and 7 June 2015, the interaction was first dominated by an increase in the solar wind dynamic pressure, caused by a higher solar wind ion density. This pressure compressed the draped magnetic field around the comet, and the increase in solar wind electrons enhanced the ionization of the outflow gas through collisional ionization. The new ions are picked up by the solar wind magnetic field, and create a ring/ringbeam distribution, which, in a high- plasma, is unstable for mirror mode wave generation. Two different kinds of mirror modes are observed: one of small size generated by locally ionized water and one of large size generated by ionization and pick-up farther away from the comet.*

## **Two-point observations of low-frequency waves at 67P/Churyumov-Gerasimenko during the descent of PHILAE: comparison of RPC-MAG and ROMAP**

Richter, I. et al. *Annales Geophysicae*, 34, 2016

*The European Space Agency's spacecraft ROSETTA has reached its final destination, comet 67P/Churyumov-Gerasimenko. Whilst orbiting in the close vicinity of the nucleus the ROSETTA magnetometers detected a new type of low-frequency wave possibly generated by a cross-field current instability due to freshly ionized cometary water group particles. During separation, descent and landing of the lander PHILAE on comet 67P/Churyumov-Gerasimenko, we used the unique opportunity to perform combined measurements with the magnetometers onboard ROSETTA (RPCMAG) and its lander PHILAE (ROMAP). New details about the spatial distribution of wave properties along the connection line of the ROSETTA orbiter and the lander PHILAE are revealed. An estimation of the observed amplitude, phase and wavelength distribution will be presented as well as the measured dispersion relation, characterizing the new type of low-frequency waves. The propagation direction and polarization features will be discussed using the results of a minimum variance analysis. Thoughts about the size of the wave source will complete our study.*

## **Low-frequency waves at comet 67P/Churyumov-Gerasimenko-Observations compared to numerical simulations**

Koenders, C. et al., *A&A*, 594, 2016

Context: A new type of low-frequency wave was detected by the magnetometer of the Rosetta Plasma Consortium at the comet during the initial months after the arrival of the Rosetta spacecraft at comet 67P/Churyumov-Gerasimenko. This large-amplitude, nearly continuous wave activity is observed in the frequency range from 30 mHz to 80 mHz where 40 mHz to 50 mHz is the dominant frequency. This type of low frequency is not closely related to the gyrofrequency of newborn cometary ions, which differs from previous wave activity observed in the interaction region of comets with the solar wind.

Aims: This work aims to reveal a global view on the wave activity region using simulations of the comet-solar wind interaction region. Parameters, such as wavelength, propagation direction, and propagation patterns, are within the focus of this study. While the Rosetta observations only provide local information, numerical simulations provide further information on the global wave properties.

Methods: Standard hybrid simulations were applied to the comet-solar wind interaction scenario. In the model, the ions were described as particles, which allows us to describe kinetic processes of the ions. The electrons were described as a fluid.

*Results: The simulations exhibit a threefold wave structure of the interaction region. A Mach cone and a Whistler wing are observed downstream of the comet. The third kind of wave activity found are low-frequency waves at 97 mHz, which corresponds to the waves observed by Richter et al. (2015, Ann. Geophys., 33, 1031). These waves are caused by the initial pick-up of the cometary ions that are perpendicular to the solar wind flow and in the interplanetary magnetic field direction. The associated electric current becomes unstable. The simulations show that wave activity is only detectable in the +E hemisphere and that the Mach cone and whistler wings need to be distinguished from the newly found instability driven wave activity.*

### ***Interaction of the solar wind with comets: a Rosetta perspective.***

Glassmeier K.-H., Philos Trans A Math Phys Eng Sci.;375(2097), 2017  
doi: 10.1098/rsta.2016.0256.

*The ROSETTA mission provides for an unprecedented possibility to study the interaction of comets with the solar wind. As the spacecraft accompanies comet 67P/Churyumov-Gerasimenko from its very low-activity stage through its perihelion phase the physics of mass loading is witnessed for various activity levels of the nucleus. While observations at other comets provided snapshots of the interaction region and its various plasma boundaries, ROSETTA observations allow a detailed study of the temporal evolution of the innermost cometary magnetosphere. Due to the short passage time of the solar wind through the interaction region, plasma instabilities such as ring-beam and non-gyrotropic instabilities are of less importance during the early life of the magnetosphere. Large-amplitude ULF waves, the singing of the comet, is probably due to a modified ion Weibel instability. This instability drives a cross field current of implanted cometary ions unstable. The initial pick-up of these ions causes a major deflection of the solar wind protons. Proton deflection, cross-field current and the instability induce a threefold structure of the innermost interaction region with the characteristic Mach cone and Whistler wings as stationary interaction signatures as well as the ULF waves representing the dynamic aspect of the interaction.*

### ***Structure and Evolution of the Diamagnetic Cavity at Comet 67P/Churyumov-Gerasimenko***

Goetz, C. et al., MNRAS, 2016

*The long duration of the Rosetta mission allows us to study the evolution of the diamagnetic cavity at comet 67P/Churyumov-Gerasimenko in detail. From April 2015 to February 2016 665 intervals could be identified where Rosetta was located in a zero-*

*magnetic-eld region. We study the temporal and spatial distribution of this cavity and its boundary and conclude that the cavity properties depend on the long-term trend of the outgassing rate, but do not respond to transient events at the spacecraft location, such as outbursts or high neutral densities. Using an empirical model of the outgassing rate, we find a functional relationship between the outgassing rate and the distance of the cavity to the nucleus. There is also no indication that this unexpectedly large distance is related to unusual solar wind conditions. Because the deduced shape of the cavity boundary is roughly elliptical on small scales and the distances of the boundary from the nucleus are much larger than expected we conclude that the events observed by Rosetta are due to a moving instability of the cavity boundary itself.*

***Magnetic field pile-up and draping at intermediately active comets: results from comet 67P/Churyumov–Gerasimenko at 2.0 AU***

Koenders, C. et al., MNRAS, 462, 2016

*The interaction between a comet and the impinging solar wind leads to modifications of the magnetic field in the environment of a comet. Among those, one finds magnetic field pile-up and draping, which reveal properties of the interaction and are known from previous cometary spacecraft missions. This work studies the magnetic field configuration at comet 67P/Churyumov–Gerasimenko at 2.0 AU. The data reveal a pile-up of the magnetic field and a draping signature nearly perpendicular to the original solar wind flow and the plane containing the solar wind flow and the interplanetary magnetic field. A comparison of the magnetic field data with a hybrid plasma simulation supports this idea of a plasma flow which is strongly deflected from the Sun–comet direction and which is in line with other plasma observations by the Rosetta Plasma Consortium.*

***Fluxgate magnetometer offset vector determination by the 3D mirror mode method***

F. Plaschke et al., MNRAS, 469, 2017, doi:10.1093/mnras/stx2532

*Fluxgate magnetometers on-board spacecraft need to be regularly calibrated in flight. In low fields, the most important calibration parameters are the three offset vector components, which represent the magnetometer measurements in vanishing ambient magnetic fields. In case of three-axis stabilized spacecraft, a few methods exist to determine offsets: (i) by analysis of Alfvénic fluctuations present in the pristine interplanetary magnetic field, (ii) by rolling the spacecraft around at least two axes, (iii) by cross-calibration against measurements from electron drift instruments or absolute magnetometers, and (iv) by taking measurements in regions of well-known magnetic fields, e.g. cometary diamagnetic cavities. In this paper, we introduce a fifth option, the 3-*

*dimensional (3D) mirror mode method, by which 3D offset vectors can be determined using magnetic field measurements of highly compressional waves, e.g. mirror modes in the Earth's magnetosheath. We test the method by applying it to magnetic field data measured by the following: the Time History of Events and Macroscale Interactions during Substorms-C spacecraft in the terrestrial magnetosheath, the Cassini spacecraft in the Jovian magnetosheath and the Rosetta spacecraft in the vicinity of comet 67P/Churyumov–Gerasimenko. The tests reveal that the achievable offset accuracies depend on the ambient magnetic field strength (lower strength meaning higher accuracy), on the length of the underlying data interval (more data meaning higher accuracy) and on the stability of the offset that is to be determined.*

### **Current sheets in comet 67P/Churyumov-Gerasimenko's coma**

Volwerk, M. et al., JGR,122, 2017

*The Rosetta Plasma Consortium (RPC) data are used to investigate the presence of current sheets in the coma of comet 67P/Churyumov-Gerasimenko. The interaction of the interplanetary magnetic field (IMF) transported by the solar wind toward the outgassing comet consists amongst others of mass loading and field line draping near the nucleus. The draped field lines lead to so-called nested draping because of the constantly changing direction of the IMF. It is shown that the draping pattern is strongly variable over the period of one month. Nested draping results in neighbouring regions with oppositely directed magnetic fields, which are separated by current sheets. Selected events on 5 and 6 June 2015 are studied, which show that there are strong rotations of the magnetic field with associated current sheets that have strengths from several tens up to hundreds of nA/m<sup>2</sup>. Not all discussed current sheets show the characteristic peak in plasma density at the centre of the sheet, which might be related to the presence of a guide field. There is no evidence for different kinds of plasmas on either side of a current sheet, and no strongly accelerated ions have been observed which could have been an indication of magnetic reconnection in the current sheets.*

### **Joint two-point observations of LF-waves at 67P/Churyumov—Gerasimenko**

Heinisch, P. et al., MNRAS, 469, 2017, [doi.org/10.1093/mnras/stx1175](https://doi.org/10.1093/mnras/stx1175)

*After the Rosetta mission reached its target comet 67P/Churyumov–Gerasimenko, the lander Philae touched down on the surface on 2014 November 12. During the First-Science-Sequence after touchdown the lander magnetometer ROMAP and the orbiter magnetometer RPC-MAG were both operating simultaneously which allowed for in situ magnetic two-point observations of the comet. This analysis aims at determining the*

characteristics of the low-frequency plasma waves present in the nucleus surface region, including frequency, propagation direction and velocity. These waves propagate predominantly from the nucleus towards the Sun with a mean phase velocity of  $\approx 5.3$  km/s, a wavelength of  $\approx 660$  km and an average frequency of  $\approx 8$  mHz.

### **Evolution of the magnetic field at comet 67P/Churyumov–Gerasimenko**

Goetz, C. et al., MNRAS, 469, 2017, [doi.org/10.1093/mnras/stx1570](https://doi.org/10.1093/mnras/stx1570)

*The magnetic field at a comet is significantly influenced by the solar wind on one side and the outgassing rate on the other. There are no simple spatial models for the magnetic field direction, neither at a comet with low outgassing rates ( $\sim 10^{25}$  s $^{-1}$ ) where ion gyroradius effects are non-negligible, nor at high outgassing rates ( $\sim 10^{27}$  s $^{-1}$ ) where plasma boundaries form. However, the long duration of the ESA Rosetta mission has made it possible to track the evolution of the magnetic field while comet 67P/Churyumov-Gerasimenko approaches the Sun. Herein we present a simple model that fits the data quite well, depending on input parameters. The study also includes the influence of the comet's gas production rate and the solar wind conditions, which both have complex effects on the magnetic field, but are clearly recognizable. The evolution of the magnetic field direction related to draping is more complex than previously suggested. Classical draping only exists at the comet for high outgassing rates, for lower rates, the magnetic field roughly follows the Parker angle. It is shown that the interaction of the solar wind with the comet can be roughly divided into three main classes.*

### **A tail like no other: RPC-MAG's view of Rosetta's tail excursion at comet 67P/Churyumov-Gerasimenko**

Volwerk, M. et al., 2017, [doi.org/10.1051/0004-6361/201732198](https://doi.org/10.1051/0004-6361/201732198)

Context: The Rosetta Plasma Consortium (RPC) magnetometer (MAG) data during the tail excursion in March - April 2016 are used to investigate the magnetic structure of and activity in the tail region of the weakly outgassing comet 67P/Churyumov-Gerasimenko (67P/CG).

Aims: The goal of this study is to compare the large scale (near) tail structure with that of earlier missions to strong outgassing comets, and the small scale turbulent energy cascade (un)related to the singing comet phenomenon.

Methods: The usual methods of space plasma physics are used to analyse the magnetometer data, such as minimum variance analysis, spectral analysis, and power law fitting. Also the cone angle and clock angle of the magnetic field are

calculated to interpret the data.

Results: It is found that comet 67P/CG does not have a classical draped magnetic field and no bilobal tail structure at this late stage of the mission when the comet is already at 2.7 AU distance from the Sun. The main magnetic field direction seems to be more across the tail direction, which may implicate an asymmetric pick-up cloud. During periods of singing comet activity the propagation direction of the waves is at large angles with respect to the magnetic field and to the radial direction towards the comet. Turbulent cascade of magnetic energy from large to small scales is different in the presence of singing as without it.

## The Mutual Impedance Probe (RPC-MIP)

Basic data analysis are:

→ Mutual impedance spectra (L3 data):

- Use mutual impedance spectrograms (electric field spectrograms in active mode) to identify time variations of the plasma frequency, and therefore variations of the plasma density.
- Analysis of mutual impedance spectra to extract bulk plasma parameters, other than the total plasma density available in the PSA.

→ Plasma density (L5 data):

- Time series analysis of derived MIP plasma density based on irregularly sampled time series spectral analysis, e.g. nonuniform discrete Fourier transform (NDFT), Lomb-Scargle periodogram, etc.
- Spatial analysis of plasma density: vertical profiles, mapping.
- Data/simulation comparisons.
- Combine MIP plasma density measurements with other sensor observations (e.g. RPC-LAP) to extract bulk plasma parameters, other than those available in the PSA.

## Relevant publications:

Some relevant publications showing examples of RPC-MIP data analysis, for both mutual impedance spectrograms (L3) and plasma density (L5):

- Trotignon et al., Space Sci. Rev. (2007) → *Description of RPC-MIP sensor design.*
- Gilet et al., Electrostatic potential radiated by a pulsating charge in a two-electron temperature plasma, Radio Sci., 52, 1432 (2017) → *Modeling of the instrumental response of RPC-MIP in a two-electron temperature plasma and application to Rosetta data.*

- Henri et al., Diamagnetic region(s): Structure of the Unmagnetised Plasma around Comet 67P/CG, Mon. Not. R. Astron. Soc., 469, 372 (2017) → *Example of Analysis of plasma density inside the diamagnetic regions.*
- Vigren et al., Model-observations Comparisons of Electron Number Densities in the Coma of 67P/Churyumov-Gerasimenko during January 2015, The Astronomical Journal, 152, 59, 2016. → *Example of derivation of plasma density time series from RPC-MIP active spectrograms and comparisons with expected plasma densities from a photo-ionisation only model.*
- Galand et al., Ionospheric plasma of comet 67P probed by Rosetta at 3 au from the Sun, Mon. Not. R. Astron. Soc., 462, 331 (2016) → *Example of derivation of plasma density time series from RPC-MIP active spectrograms and comparisons with expected plasma densities from a ionisation model combining photo-ionisation and ionisation by electron impact.*
- Héritier et al., Vertical structure of the near-surface ionosphere of comet 67P probed by Rosetta: the birth of a cometary ionosphere, Mon. Not. R. Astron. Soc., 469, 118 (2017) → *example of cometary ionospheric plasma density study, including a cross-calibration of RPC-LAP and RPC-MIP density measurements, the extraction of a cometary plasma density vertical profile, and comparisons with expected plasma densities from an ionisation model.*
- Hajra et al. Impact of a cometary outburst on its ionosphere: Rosetta Plasma Consortium observations of the comet 67P/CG outburst on 19 February 2016, Astronomy and Astrophysics, 607, A34 (2017) → *two examples of plasma density extraction from RPC-MIP active spectrograms in the context of cometary plasma increase associated to a cometary outburst [see also Grün et al., The 2016 Feb 19 outburst of comet 67P/CG: an ESA Rosetta multi-instrument study, MNRAS, 462, 220 (2016).*
- Vigren et al., Effective ion speeds at 200-250 km from comet 67P/Churyumov-Gerasimenko near perihelion, Mon. Not. R. Astron. Soc., 469, 142 (2017) → *Example of combined analysis of RPC-MIP and RPC-LAP measurements to extract and study ion bulk velocities.*

## The Plasma Interface Unit (RPC-PIU)

- **Illumination maps:** Examples of the use of illumination maps in order to provide a context in science papers include: Galand et al. 2016; Heritier et al. 2017a; Hoang et al. 2016.

## 4. Description of the data present in the PSA

### Ion energy spectra from RPC-ICA and RPC-IES

**RPC-ICA** measures ions in the energy range from a few eV up to 40 keV per charge. RPC-ICA can distinguish ions of a mass per charge of 1, 2, 4, 8 and 16 and above. The energy resolution is 7%. The angular resolution is 22.5° x 5°. ICA has a 360° field of view in its central plane, and electrostatic deflection provides angular coverage of about +/- 45° out of that plane in 16 steps of about 5.6°. The 3D temporal resolution of RPC-ICA is 192 s. The instrument can also be used to obtain 2D data with an energy range up to about 100 eV with 1s or 4s resolution.

The range and the resolution of **ion** data acquired by the **RPC-IES** instrument are described below. The actual range and the resolution of the data within the data files listed in this section are mode-dependent and may be restricted due to the telemetry limitations as described in section 2 of this document. Further details can be found in the EAICD and the instrument paper as described in section 1 of this document. Note that the ion energy is also influenced by the spacecraft potential; negative values for the latter yield a shift towards higher energies for the positive ions.

Overview of RPC-IES ion spectrometer:

Energy range: 4.32 eV/q to 17.67 keV/q using 124 steps with 4 additional steps for flyback

Energy resolution ( $\Delta E/E$ ): 8% at each step

Elevation range: -45° to +45° using 16 steps

Elevation resolution: 5°

Azimuthal range: 0° to 360° using 16 anodes read simultaneously

Azimuthal resolution: 5° for fine anodes (3 to 11) and 45° for coarse anodes (0 to 2 and 12 to 15)

<b>Ion energy distribution</b>				
<b>Name</b>	<b>Unit</b>	<b>Sensor</b>	<b>Level</b>	<b>Brief description</b>
ICA raw data	Counts per acquisition period	ICA	L2	Raw energy spectrograms for different mass channels, and angular directions. Time resolution of 1,4 or 192 s. PSA: <a href="ftp://psa.esac.esa.int/pub/mirror/INTERNATIONAL-ROSETTA-MISSION/RPCICA/">ftp://psa.esac.esa.int/pub/mirror/INTERNATIONAL-ROSETTA-MISSION/RPCICA/</a> Data set: RAW File name convention: RPCICAYYYYMMDDTHH_xxx_L2.TAB where

				xxx is a running number increasing if there are several data files for the same hour, usually due to a change of software version
ICA differential flux	ions/cm <sup>2</sup> /s/sr/eV	ICA	L3	<p>Calibrated energy spectrograms for different mass channels, and angular directions. Time resolution of 1,4 or 192 s. PSA:  <a href="ftp://psa.esac.esa.int/pub/mirror/INTERNATIONAL-ROSETTA-MISSION/RPCICA/">ftp://psa.esac.esa.int/pub/mirror/INTERNATIONAL-ROSETTA-MISSION/RPCICA/</a>  Data set: CALIBRATED  File name convention:  RPCICAYYYMMDDTHH_xxx_L3.TAB where xxx is a running number increasing if there are several data files for the same hour, usually due to a change of software version</p>
ICA cleaned differential energy spectra	ions/cm <sup>2</sup> /s/sr/eV	ICA	L4	<p>Calibrated energy spectrograms for different mass channels, and angular directions. Corrected for cross talk, different on-board noise reduction settings. Time resolution of 1,4 or 192 s. PSA:  <a href="ftp://psa.esac.esa.int/pub/mirror/INTERNATIONAL-ROSETTA-MISSION/RPCICA/">ftp://psa.esac.esa.int/pub/mirror/INTERNATIONAL-ROSETTA-MISSION/RPCICA/</a>  Data set: L4 CORR  File name convention:  RPCICAYYYMMDDTHH_xxx_L4.TAB where xxx is a running number increasing if there are several data files for the same hour, usually due to a change of software version</p>
ICA mass separated data	ions/cm <sup>2</sup> /s/sr/eV	ICA	L4	<p>Calibrated energy spectrograms for different physical ion mass ranges, and angular directions. A conservative approach was used, so if there was any uncertainty in the ion mass, the corresponding data was removed. Time resolution of 1,4 or 192 s. PSA:  <a href="ftp://psa.esac.esa.int/pub/mirror/INTERNATIONAL-ROSETTA-MISSION/RPCICA/">ftp://psa.esac.esa.int/pub/mirror/INTERNATIONAL-ROSETTA-MISSION/RPCICA/</a>  Data set: L4 PHYS_MASS  File name convention:</p>

				RPCICAYYYYMMDDTHH_xxx_L2_I.TAB where xxx is a running number increasing if there are several data files for the same hour, usually due to a change of software version. I indicates the ion mass, H, He2, He or HVY.
IES ion counts	counts (ions)	ION	L2	Raw ion counts Dataset: RO-*-RPCIES-2-*-V* Files: RPCIES*_ION_V*.TAB
IES Ion Differential Energy Flux (DEF)	$\frac{ions}{m^2*s*sr*(eV/eV)}$	ION	L3	Calibrated differential energy flux of ions Dataset: RO-*-RPCIES-3-*-V* Files: RPCIES*_L3ION_FLUX_V*.TAB
Uncertainty in IES Ion DEF	$\frac{ions}{m^2*s*sr*(eV/eV)}$	ION	L3	Uncertainty in the calculation of differential energy flux of ions Dataset: RO-*-RPCIES-3-*-V* Files: RPCIES*_L3ION_FLUN_V*.TAB

## Electron energy spectra from RPC-IES

The range and the resolution of electron data acquired by the IES instrument are described below. The actual range and the resolution of the data within the data files listed in this section are mode-dependent and may be restricted due the telemetry limitations as described in section 2 of this document. Further details can be found in the EAICD and the instrument paper as described in section 1 of this document. Note that the electron energy is also influenced by the spacecraft potential; negative values for the latter yield a shift towards lower energies for the electrons. Correction for the spacecraft potential is for instance described in Galand et al. (2016).

Energy range: 4.32 eV/q to 17.67 keV/q using 124 steps with 4 additional steps for flyback

Energy resolution ( $\Delta E/E$ ): 8% at each step

Elevation range:  $-45^\circ$  to  $+45^\circ$  using 16 steps

Elevation resolution:  $5^\circ$

Azimuthal range:  $0^\circ$  to  $360^\circ$  using 16 anodes read simultaneously

Azimuthal resolution:  $22.5^\circ$

<b>Electron energy distribution</b>				
<b>Name</b>	<b>Units</b>	<b>Sensor</b>	<b>Level</b>	<b>Brief Description</b>
Electron counts	counts (electrons)	ELC	L2	Raw electron counts Dataset: RO-*-RPCIES-2-*-V* Files: RPCIES*_ELC_V*.TAB
Electron Differential Energy Flux (DEF)	$\frac{electrons}{m^2*s*sr*(eV/eV)}$	ELC	L3	Calibrated differential energy flux of electrons Dataset: RO-*-RPCIES-3-*-V* Files: RPCIES*_L3ELC_FLUX_V*.TAB
Uncertainty in Electron DEF	$\frac{electrons}{m^2*s*sr*(eV/eV)}$	ELC	L3	Uncertainty in the calculation of differential energy flux of electrons Dataset: RO-*-RPCIES-3-*-V* Files: RPCIES*_L3ELC_FLUN_V*.TAB

## Magnetic field from RPC-MAG

Magnetometer Data: RPC-MAG					
<i>Entity</i>	<i>Unit</i>	<i>Sensor</i>	<i>Level</i>	<i>Coordinates</i>	<i>Brief description</i>
Magnetic field	Raw ADC Counts	RPC-MAG-OB RPC-MAG-IB	L2	Instrument	Magnetic field data with original sampling (1Hz or 20Hz, resp. 1/32 Hz or 1Hz). Datasets: RO-{target}-RPCMAG-2-{missionphase}-RAW-V{version} Datafiles: RPCMAG{date}_RAW_{sensor}_M{mode}.*
Magnetic field	nT	RPC-MAG-OB RPC-MAG-IB	L3	Instrument (LEVEL_A)	Magnetic field data with original sampling (1Hz or 20Hz, resp. 1/32 Hz or 1Hz), Datasets: RO-{target}-RPCMAG-3-{missionphase}-CALIBRATED-V{version} Datafiles: RPCMAG{date}_CLA_{sensor}_M{mode}.*
Magnetic field	nT	RPC-MAG-OB RPC-MAG-IB	L3	s/c (LEVEL_B)	Magnetic field data with original sampling (1Hz or 20Hz, resp. 1/32 Hz or 1Hz), Datasets: RO-{target}-RPCMAG-3-{missionphase}-CALIBRATED-V{version} Datafiles: RPCMAG{date}_CLB_{sensor}_M{mode}.*
Magnetic field	nT	RPC-MAG-OB RPC-MAG-IB	L3	CELESTIAL (LEVEL_C)	Magnetic field data with original sampling (1Hz or 20Hz, resp. 1/32 Hz or 1Hz), Data contain s/c positions as well. Datasets: RO-{target}-RPCMAG-3-{missionphase}-CALIBRATED-V{version} Datafiles: RPCMAG{date}_CLC_{sensor}_M{mode}.*
Magnetic field	nT	RPC-MAG-OB RPC-MAG-IB	L4	s/c (LEVEL_F)	Magnetic field data resampled to 1s and 64s averages. Datasets: RO-{target}-RPCMAG-4-{missionphase}-RESAMPLED-V{version} Datafiles: RPCMAG{date}_CLF_{sensor}_A{average}.*
Magnetic field	nT	RPC-MAG-OB RPC-MAG-IB	L4	CELESTIAL (LEVEL_G)	Magnetic field data resampled to 1s and 64s averages. Data contain s/c positions as well. Datasets: RO-{target}-RPCMAG-4-{missionphase}-RESAMPLED-V{version} Datafiles: RPCMAG{date}_CLG_{sensor}_A{average}.*
Magnetic field	nT	RPC-MAG-OB	L4	CELESTIAL (LEVEL_H)	Magnetic field data resampled at original sampling rate of 20 Hz. Reaction Wheel disturbance eliminated. Data contain s/c positions as well. Datasets:

					RO-{target}-RPCMAG-4-{missionphase}-RESAMPLED-V{version} Datafiles: RPCMAG{date}_CLG_OB_M3.*
--	--	--	--	--	--

## Plasma density from RPC-LAP and RPC-MIP (to add RPC-ICA and RPC-IES moments)

This section is dedicated to summarise and clarify the measurements from the different plasma instruments. Each RPC instrument probes different plasma populations (e.g., electrons, cometary ions, solar wind ions) which are associated with different energy ranges. The goal is to identify what the measurements of interest are and/or what the most relevant data projects (from a given sensor or from a combination of sensors) are for detailed analysis.

Hereafter we give a brief summary of the pros and cons of the different instruments:

- RPC-MIP: it provides the electron number density by identifying the plasma resonance frequency  $f_p$  in the mutual impedance spectrum, i.e., the response of the plasma to a weak emitted signal. As  $f_p$  depends on no other plasma parameter than the density [TO BE REVIEWED - FOR WARM ELECTRONS,  $f_p$  ALSO DEPENDS ON  $T_e$ ], this method is considered to provide the most accurate RPC density estimate, for the density range in which MIP can operate. For densities below some 50-100  $\text{cm}^{-3}$ , MIP cannot identify  $f_p$ , and so does not provide any density (data gap). Time average over such a period is not suitable as it would underestimate the density (considering MIP only).
  - Major strength: absolute density value and not sensitive to  $V_S$
  - Major limitation: needs sufficiently high number density (few hundreds  $\text{cm}^{-3}$ )
- RPC-LAP: it has several methods to derive the plasma (ion or electron) density. Only the bias voltage sweeps provide an absolute value, based on the collection of electrons, as electron temperature can be independently measured if in a suitable range (eV). Continuous sampling of probe current or voltage between sweeps needs absolute calibration by sweeps or MIP on case by case basis to bring uncertainty down to factor of two level. The spacecraft potential  $V_S$  can be determined also in very tenuous plasmas, but once again needs calibration to other density measurements to provide absolute values.
  - Major strength: wide dynamic range, from a few to a tens of thousands of  $\text{cm}^{-3}$  by various methods
  - Major limitation: Uncertainties grow large outside the 10-1000  $\text{cm}^{-3}$  range
- RPC-ICA: it is possible to calculate the different moments of the ion distribution function from ICA observations over energies above 4 eV. As the instrument is not boom-mounted like LAP and MIP, the negative (typically -20 V) spacecraft potential  $V_S$  complicates the observations of low energy ions. ICA densities are best in tenuous plasmas like the solar

wind, provided that a directed ion stream falls within the instrument field of view (FoV). This is often but not always the case as both the Sun and the comet nucleus most of the time are within this FoV.

- Major strength: density estimates at low density
  - Major limitation: Field of view and  $V_S$  issues
- RPC-IES: it is possible to calculate the different moments of the electron and ion distribution functions (esp., number density, moment of order 0) from the electron or ion sensor. For electrons, the method used usually is fitting to a population model (i.e., imposing an energy distribution) rather than integration of moments [Broiles et al. 2016]. Being mounted close to ICA, the ion sensor has similar limitations to ICA, though FoV issues are often stronger as the Sun and nucleus often are on the limit of the FoV. When the spacecraft potential  $V_S$  is low (in absolute value), i.e., in tenuous plasmas like the solar wind, the IES electron sensor has a good chance of acquiring the full plasma density. When  $V_S$  is more negative during the active comet phase electrons at low energy cannot reach IES so the density uncertainty grows large.
    - Major strength: density estimates at low electron density
    - Major limitation: Field of view and  $V_S$  issues, limitation on the detection of low energy ions

The next two figures provide an rough overview between instruments in terms of the working range or where most of observations have been made. For instance:

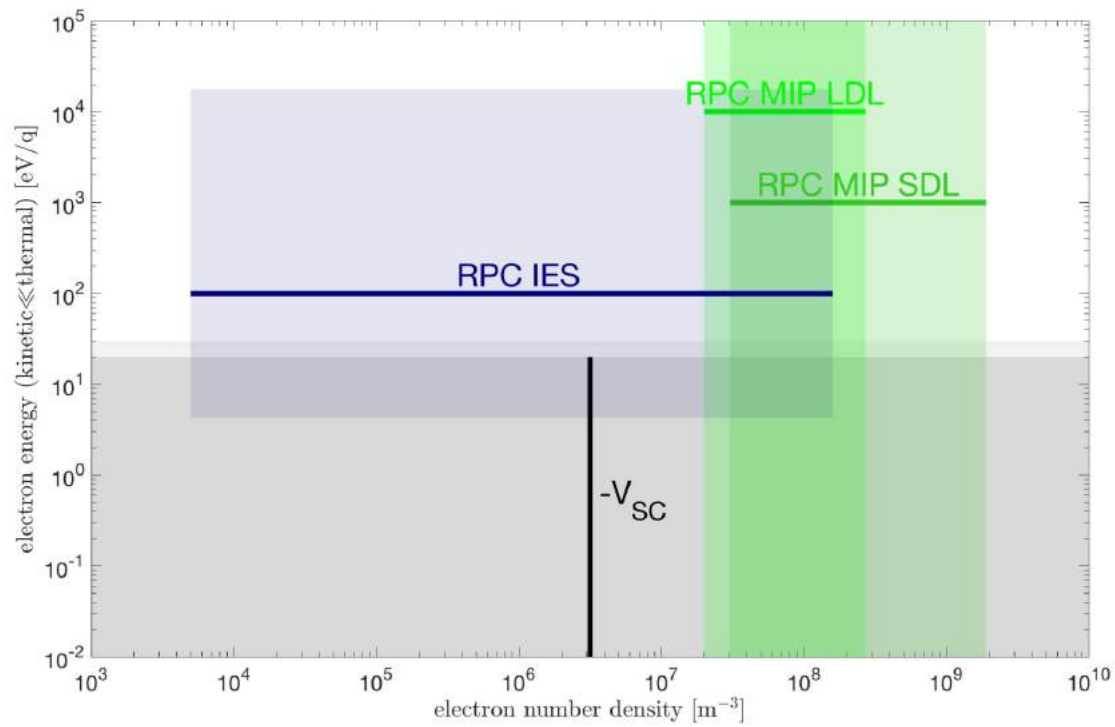
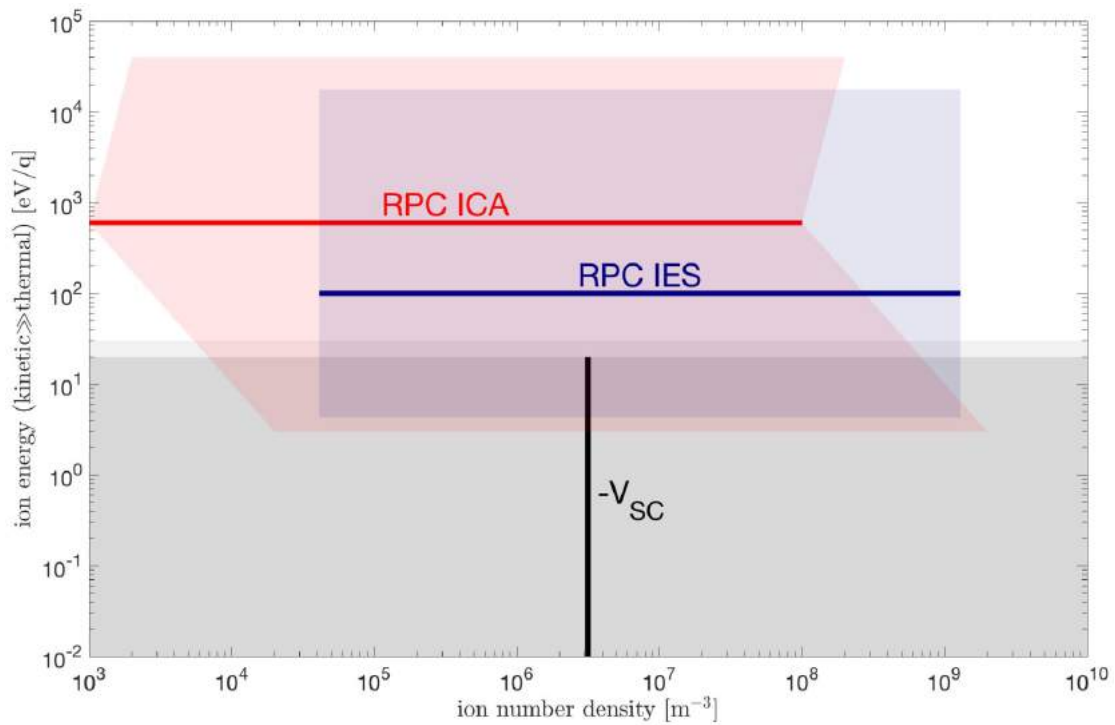
- RPC-MIP: the electron number density from RPC-MIP results from the full escort phase analysis, and highlights that the majority of the observations (within 2 sigma) is in this range. **ENERGY constraint on RPC-MIP missing**
- RPC-IES: The ion and electron density range for RPC-IES is only for ions (resp. electrons) of 1 keV (resp. 10 eV) and probably needs an energy dependence. **DENSITY constraint on RPC-IES is missing for ions and electrons**
- RPC-ICA is directly constrained from the instrument and gives the limits at which ICA is reliable. However, there are strong limitations at low energies because of the spacecraft potential.
- **RPC-LAP missing**

The spacecraft potential has been overplotted to highlight the associated limits of some instruments (e.g., RPC-IES and RPC-ICA).

We would also like to point out that the definition of energy is not the same for ions and electrons:

- For ions, it mainly corresponds to the mean kinetic energy
- For electrons, it mainly corresponds to the mean thermal energy or the dispersion around the mean velocity vector.

**TO ADD OVERVIEW FIGURES WITH ONLY NUMBER DENSITY RELEVANT RANGE**



<b>SOLAR WIND DENSITY</b>				
<b>Name</b>	<b>Unit</b>	<b>Sensor</b>	<b>Level</b>	<b>Brief description</b>
		IES		Moment of order 0
		ICA		Moment of order 0

<b>ION PLASMA DENSITY</b>				
<b>Name</b>	<b>Unit</b>	<b>Sensor</b>	<b>Level</b>	<b>Brief description</b>
		IES		Moment of order 0
		ICA		Moment of order 0

<b>ELECTRON PLASMA DENSITY</b>				
<b>Name</b>	<b>Unit</b>	<b>Sensor</b>	<b>Level</b>	<b>Brief description</b>
LAP_MIP_ne	cm <sup>-3</sup>	LAP, MIP	L5	<p>High time resolution plasma density on selected periods, derived from cross-calibration of RPC-MIP density and RPC-LAP potential or ion current.</p> <p>Time resolution equivalent to RPC-LAP data</p> <p>Provide time resolution, which dataset was combined, where to find it on the PSA</p> <p>PSA dataset: <b>TBD</b></p> <p>Data files: <b>TBD</b></p>

MIP density	cm <sup>-3</sup>	MIP	L5	<p>Plasma electron density, derived from RPC-MIP spectra analysis, with a larger mission coverage than LAP_MIP_n but a lower time resolution (irregular).</p> <p>PSA dataset: RO-C-RPCMIP-5-&lt;missionphase&gt;-V&lt;version&gt;</p> <p>Data files: RPCMIPS5DX_&lt;date&gt;.TAB</p>
LAP density		LAP		XXX

Electric field from RPC-LAP and RPC-MIP

<b>ELECTRIC FIELD</b>				
<b>Name</b>	<b>Unit</b>	<b>Sensor</b>	<b>Level</b>	<b>Brief description</b>
MIP passive spectra	dB	MIP	L3	<p>Electric field spectra</p> <p>Time resolution depends on operational parameters (see section 2 and RPC-MIP user guide)</p> <p>PSA dataset: RO-C-RPCMIP-3-&lt;missionphase&gt;-V&lt;version&gt;</p> <p>Data files: one file type per sub-mode RPCMIPS3E&lt;ab&gt;&lt;date&gt;.TAB</p> <p>where &lt;ab&gt; describes the mode/sub-mode (see RPC-MIP user guide for details)</p>

MIP spectra	active	dB	MIP	L3	<p>Electric field mutual impedance spectra</p> <p>Time resolution depends on operational parameters (see section 2 and RPC-MIP user guide)</p> <p>PSA dataset: RO-C-RPCMIP-3-&lt;missionphase&gt;-V&lt;version&gt;</p> <p>Data files: one file type per sub-mode RPCMIPS3W&lt;ab&gt;&lt;date&gt;.TAB amplitude spectra RPCMIPS3H&lt;ab&gt;&lt;date&gt;.TAB phase spectra</p> <p>where &lt;ab&gt; describes the mode/sub-mode (see RPC-MIP user guide for details)</p>
----------------	--------	----	-----	----	---

Electron temperature from RPC-LAP and RPC-MIP

<b>ELECTRON TEMPERATURE</b>				
<b>Name</b>	<b>Unit</b>	<b>Sensor</b>	<b>Level</b>	<b>Brief description</b>
XX	XX	XX	XX	XX

## 5. Recommended software for visualisation/analysis of the RPC science data

### AMDA

AMDA is a powerful online data visualisation and access tool. It permits multi-sensor visualization within the same browser window, and data selection based on these plots. It permits the user to see products from different instruments plotted on the same time axes. It can be used with pre-defined as well as user defined (and saved) plots designs. Data held on AMDA is publicly available for download if it is publicly available through the PSA.

The AMDA system is accessed at <http://amda.cdpp.eu/> . New users should select the Demo Tour button.

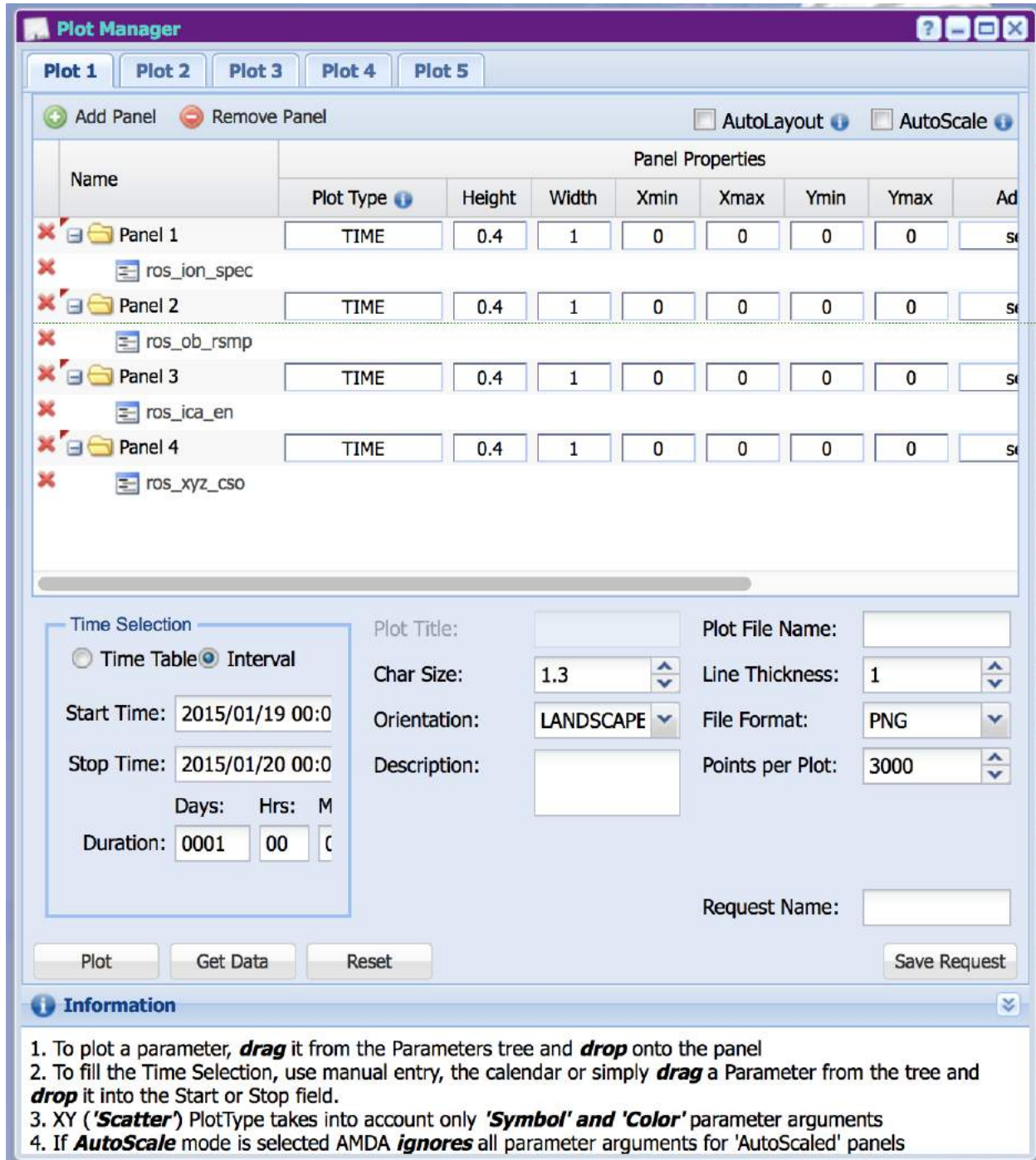
In order to plot a dataset, in the “Workspace Explorer” window, go to:

Resources → Parameters → Amda Database → Rosetta

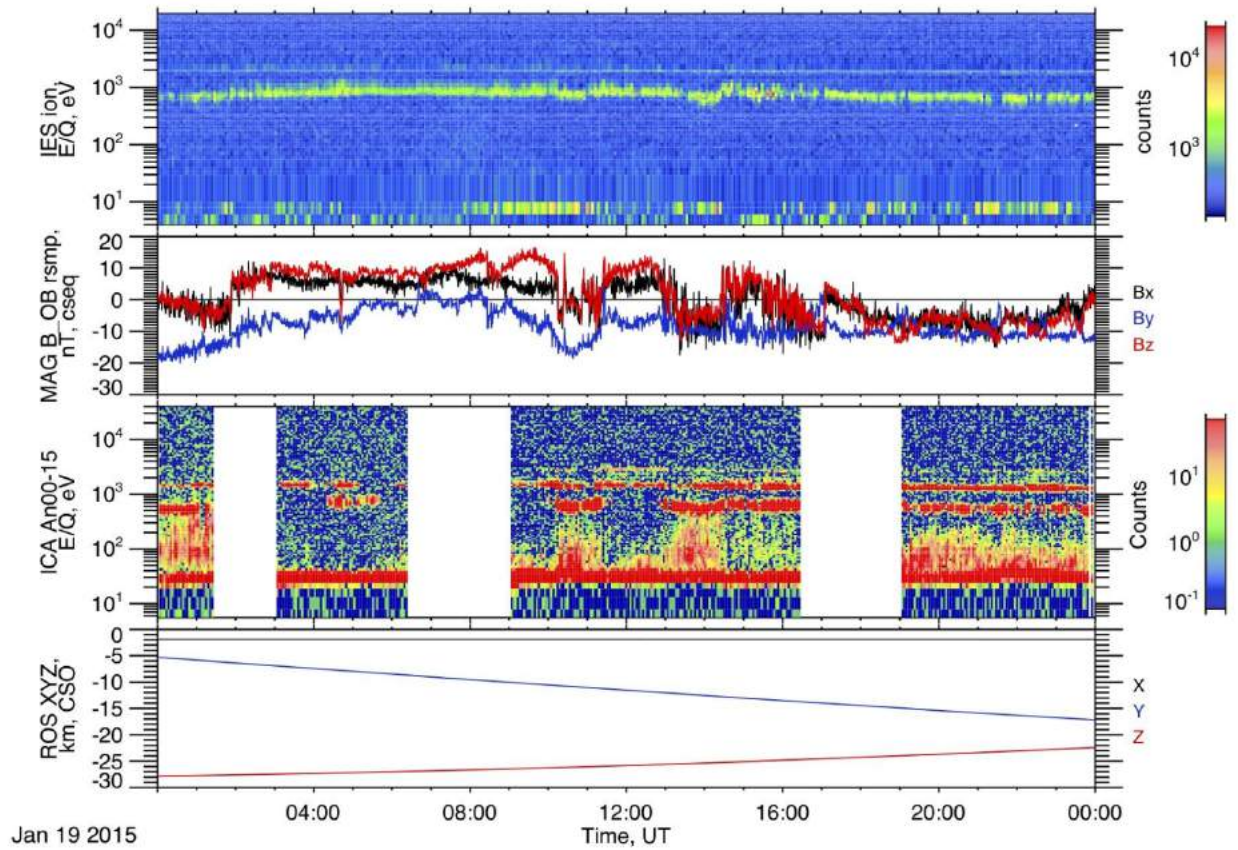
There, you can choose among the various ephemeris, RPC and ROSINA parameters which are available (see full detail in Table XX below).

Next, click on the icon “Plot Data” and drag the relevant parameters to plot from the Workspace Explorer window to the “Plot Manager” window.

One example is given below:



Which generates the following figure of the RPC and Ephemeris dataset:



Rosetta datasets in AMDA which are public to all, as of March 2018:

Instrument	Status	Description
AUX	OK	useful Orbit/Attitude data; Sampling 60 s; Provider Imperial College; Producer WIGNER Research Centre for Physics,Hungary
Ephemeris	OK	cruise; Sampling 1h; calculated by IRAP from SPICE Kernels (PSA)
Ephemeris	OK	orbit; Sampling 60s; calculated by IRAP from SPICE Kernels (PSA)
Ephemeris	OK	sun position in C-G_CK frame; Sampling 60s; calculated by IRAP from SPICE Kernels (PSA)
ICA	Public soon	ion energy spectra; Sampling 192s; Provider Imperial College; Producer IRF
IES	OK	electron azimuthal spectra; Sampling 128 s; Provider Imperial College; Producer Southwest Research Institute, San Antonio
IES	OK	electron elevation spectra; Sampling 128 s; Provider Imperial College;

		Producer Southwest Research Institute, San Antonio
IES	OK	electron energy spectra; Sampling 128 s; Provider Imperial College; Producer Southwest Research Institute, San Antonio
IES	OK	ion azimuthal spectra; Sampling 128 s; Provider Imperial College; Producer Southwest Research Institute, San Antonio
IES	OK	ion elevation spectra; Sampling 128 s; Provider Imperial College; Producer Southwest Research Institute, San Antonio
IES	OK	ion energy spectra; Sampling 128 s; Provider Imperial College; Producer Southwest Research Institute, San Antonio
LAP	TBD	S/C potential [TO BE CHECKED WHEN PUBLICLY ACCESSIBLE]
MAG	OK	inboard sensor, burst mode; Sampling 1s; Provider PSA; ProviderResource RO-C-RPCMAG-3-ESC[1-3],EXT[1-3]-CALIBRATED/IB/LEVEL_C/M3
MAG	OK	inboard sensor, normal mode; Sampling 32s; Provider PSA; ProviderResource RO-C-RPCMAG-3-ESC[1-3],EXT[1-3]-CALIBRATED/IB/LEVEL_C/M2
MAG	OK	inboard sensor; resampled; Sampling 32s; resampled and merged at IRAP from two PSA datasets
MAG	OK	outboard sensor, burst mode; Sampling 0.05s; Provider PSA; ProviderResource RO-C-RPCMAG-3-ESC[1-3],EXT[1-3]-CALIBRATED/OB/LEVEL_C/M3
MAG	OK	outboard sensor, normal mode; Sampling 1s; Provider PSA; ProviderResource RO-C-RPCMAG-3-ESC[1-3],EXT[1-3]-CALIBRATED/OB/LEVEL_C/M2
MAG	OK	outboard sensor; resampled; Sampling 1s; resampled and merged at IRAP from two PSA datasets
MIP	Public soon	LDLFULL; Sampling 2.65s; Provider Imperial College; Producer LPC2E Orleans
MIP	Public soon	LDLFULL_PHASE; Sampling 2.65s; Provider Imperial College; Producer LPC2E Orleans
MIP	Public soon	PASSIVEFULL; Sampling 1.2s; Provider Imperial College; Producer LPC2E Orleans
MIP	Public soon	PASSIVEWINDOW; Sampling 1.2s; Provider Imperial College; Producer LPC2E Orleans
MIP	Public soon	SURVEYFULL; Sampling 4.38s; Provider Imperial College; Producer LPC2E Orleans

MIP	Public soon	SURVEYFULL_PHASE; Sampling 4.38s; Provider Imperial College; Producer LPC2E Orleans
ROSINA	TBC	Total neutral density and pressure nude/ram gauge [TO BE CHECKED IF/WHEN PUBLICLY ACCESSIBLE]

Note that data downloaded from AMDA does not currently come with metadata attached, and it is recommended for data interval selection, but the PSA should be used as primary source of RPC data. AMDA expects to ultimately provide visualisation of all RPC data held at the PSA. It also has Rosina products from the RPC quicklook system.

Note also that AMDA will mirror PSA Rosina neutral density and pressure, which is often of relevance to RPC science.

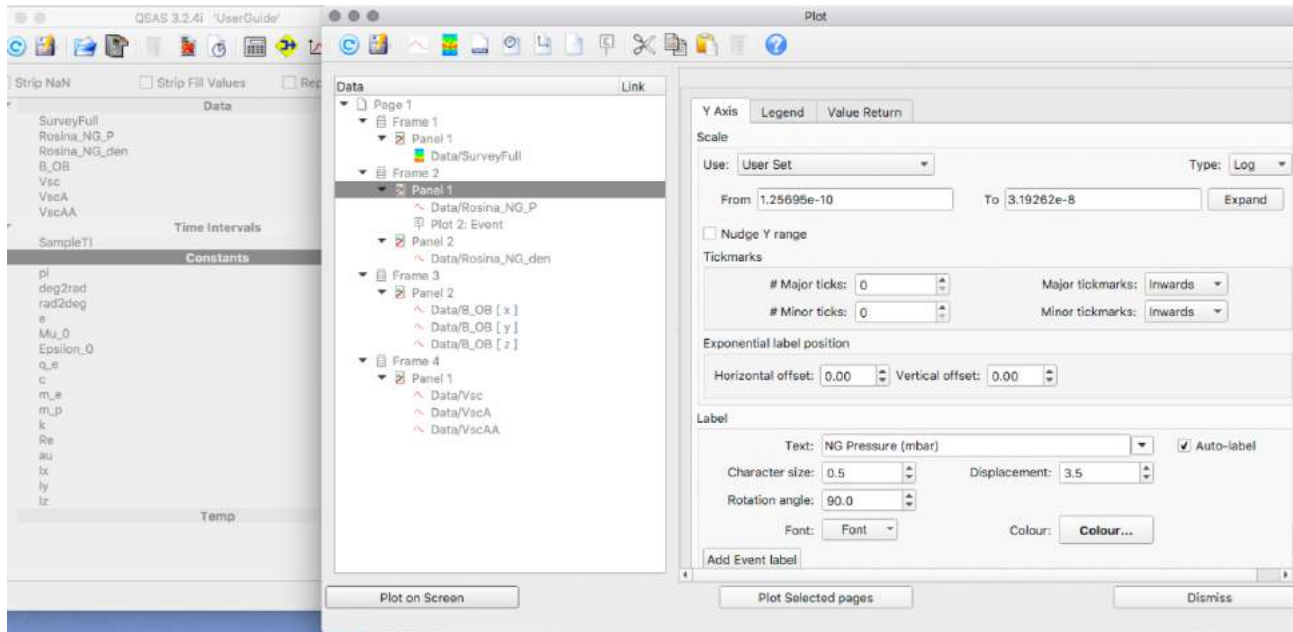
## QSAS

QSAS is a software tool run on the user's own computer. It may be downloaded (available for Mac, Windows and Linux) from <https://sourceforge.net/projects/qsas> and the QSAS homepage is at [http://www.sp.ph.ic.ac.uk/csc-web/QSAS/qsas\\_welcome.html](http://www.sp.ph.ic.ac.uk/csc-web/QSAS/qsas_welcome.html)

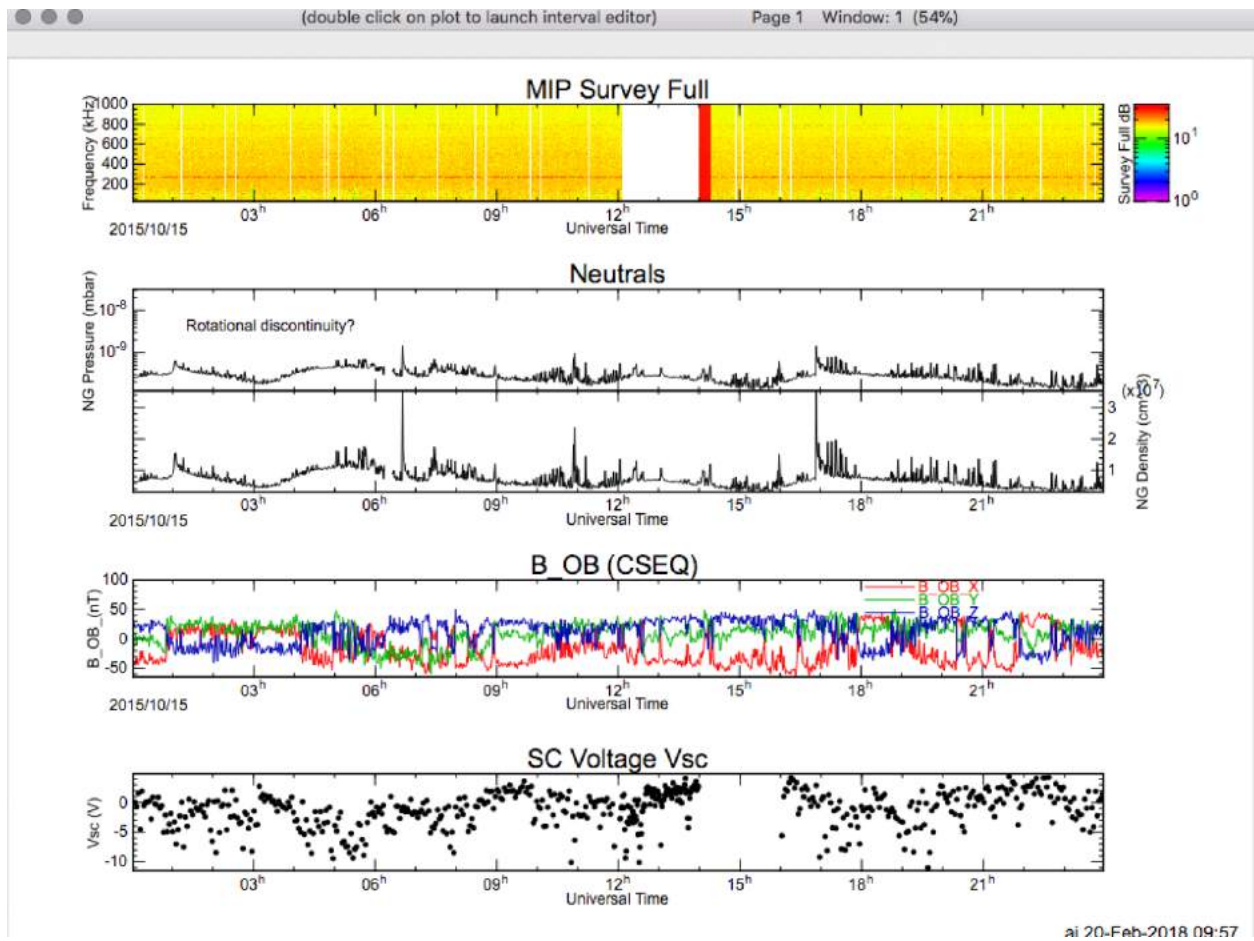
QSAS can read, manipulate and plot multi-instrument and multi-spacecraft time series data.

Data is held in a 'Working List' of data objects, and operations are assembled via simple drag and drop between windows.

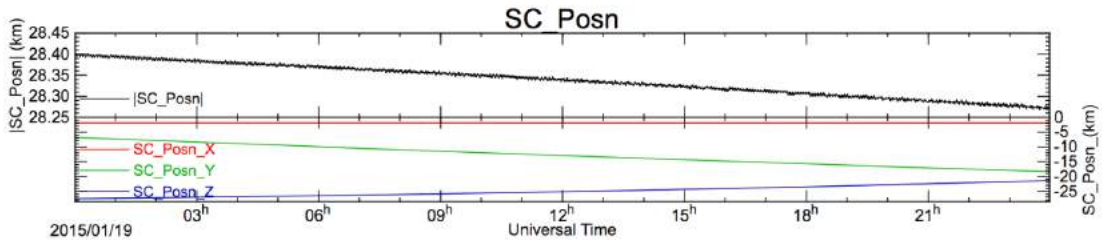
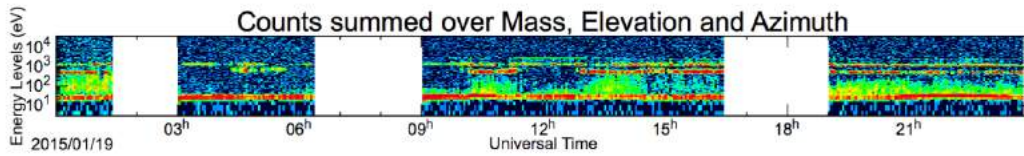
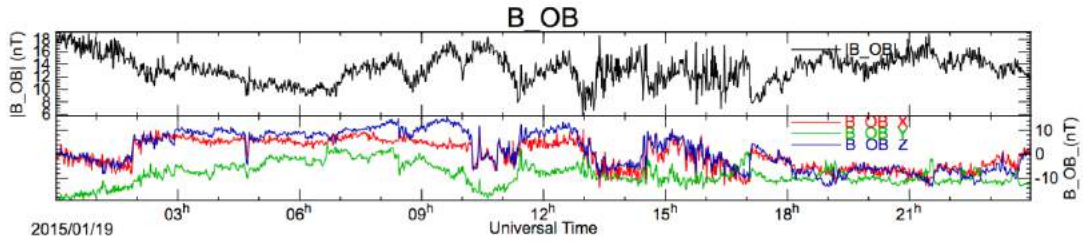
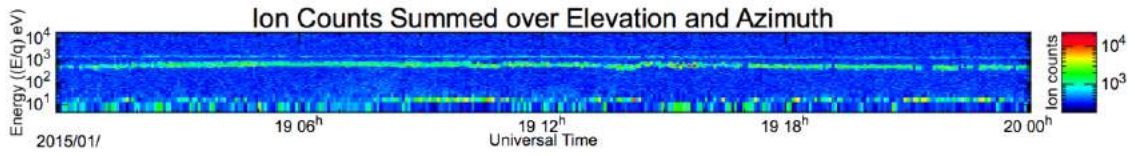
The following figure show the QSAS main window (Working List) and plot interface.



The resulting plot shows traces and spectra combined: From top to bottom: RPC-MIP frequency, Rosetta Orbiter Spectrometer for Ion and Neutral Analysis (ROSINA)-Comet Pressure Sensor (COPS) neutral pressure and total number density and RPC-MAG magnetic field components in the CSEQ reference frame.



For comparison, the same data as the AMDA plot is shown using QSAS, from January 19, 2015:



ai 28-Feb-2018 12:08

Higher dimensional data may be viewed in 2D and 3D as polar or relief plots or as slices through a 3-dimensional distribution. The data input slots in all plot windows allow for sum, average, slice or sub-sample over any of the dimensions to reduce higher dimensional data to be suitable for the selected plot type.

Polar Plot

Data Plot Options Page

Plot Title: ICA counts (summed over elevation and mass)  Auto-Title

Plot Type: Arc-Filled R axis Text: r (eV) Angle axis Text: Angle (deg)

Axis Type: x=0, y=0 only Axis width: 1.0 Axis extent: 1.30

Data Points: No Data Points Label % of points: 100 Label above val: Label All

Add Contours Contour width: 1.0 Contour interval: Default Contour Label: No Contour Label

Log Radius  Auto radius Min Radius: 10 Max Radius: 10000

Log ColourScale  Auto ColourScale Min value: 1 Max value: 2813

Colour Table: Rainbow Extended Colour bar label: sum sum (0,15) (0,15)

Title font size: 1.0 Text font size: 0.5  Phi as local time

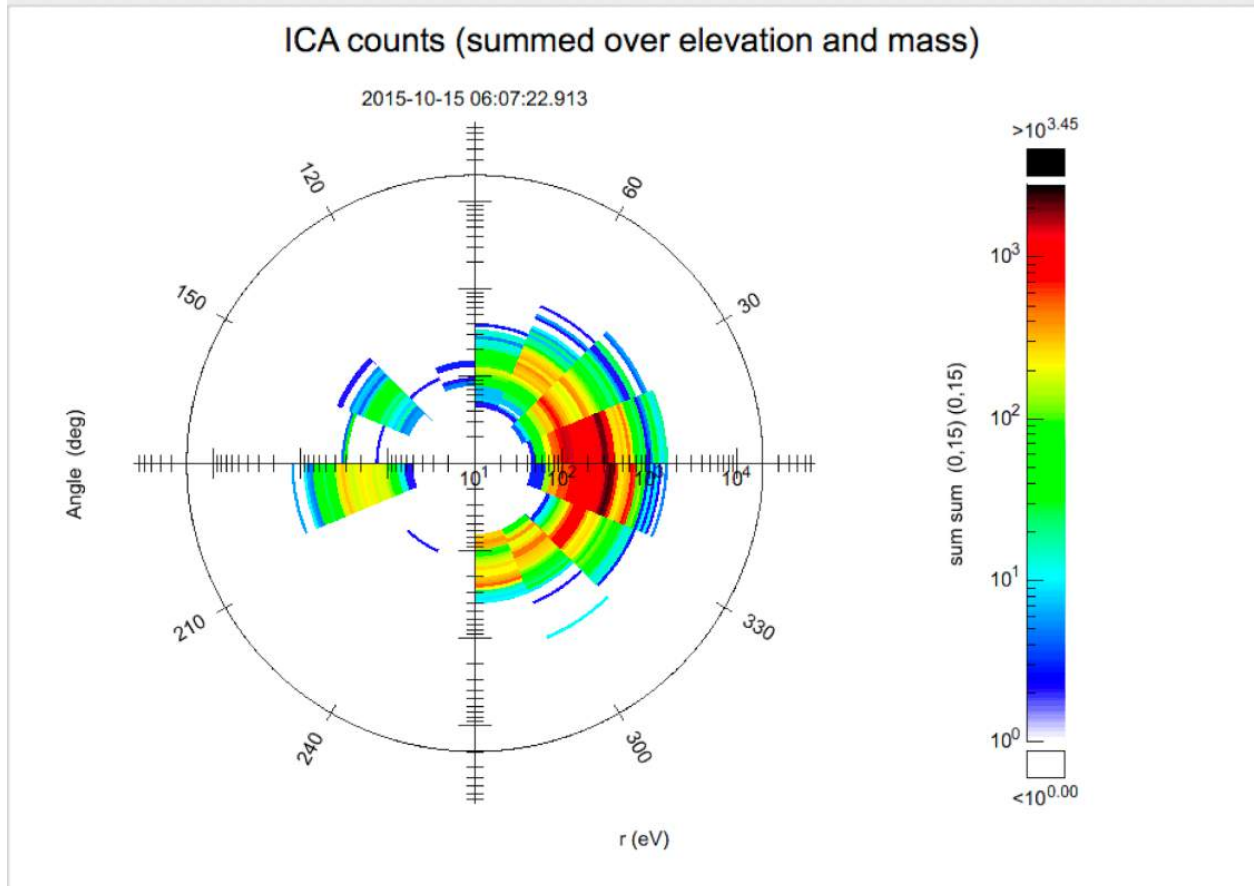
---

Min,Max r values: 0.5, 39975.2

New Plot  
Cannot find Bin Boundaries for radial bins, defining arbitrary boundaries.

Plot Animate Time Dismiss

Polar Plot 1 (52%)



Polar Plot

Data Plot Options Page

Plot Title: IES Elc Counts [ (1,126) Sum(1,16) (1,16) ]  Auto-Title

Plot Type: Arc-Filled R axis Text: Energy ((E/q) eV) Angle axis Text: Azimuth (deg)

Axis Type: x=0, y=0 only Axis width: 1.0 Axis extent: 1.30

Data Points: No Data Points Label % of points: 99 Label above val: Label All

Add Contours Contour width: 1.0 Contour interval: Default Contour Label: No Contour Label

Log Radius  Auto radius Min Radius: 2.0736 Max Radius: 18377

Log ColourScale  Auto ColourScale Min value: 0.25 Max value: 117760

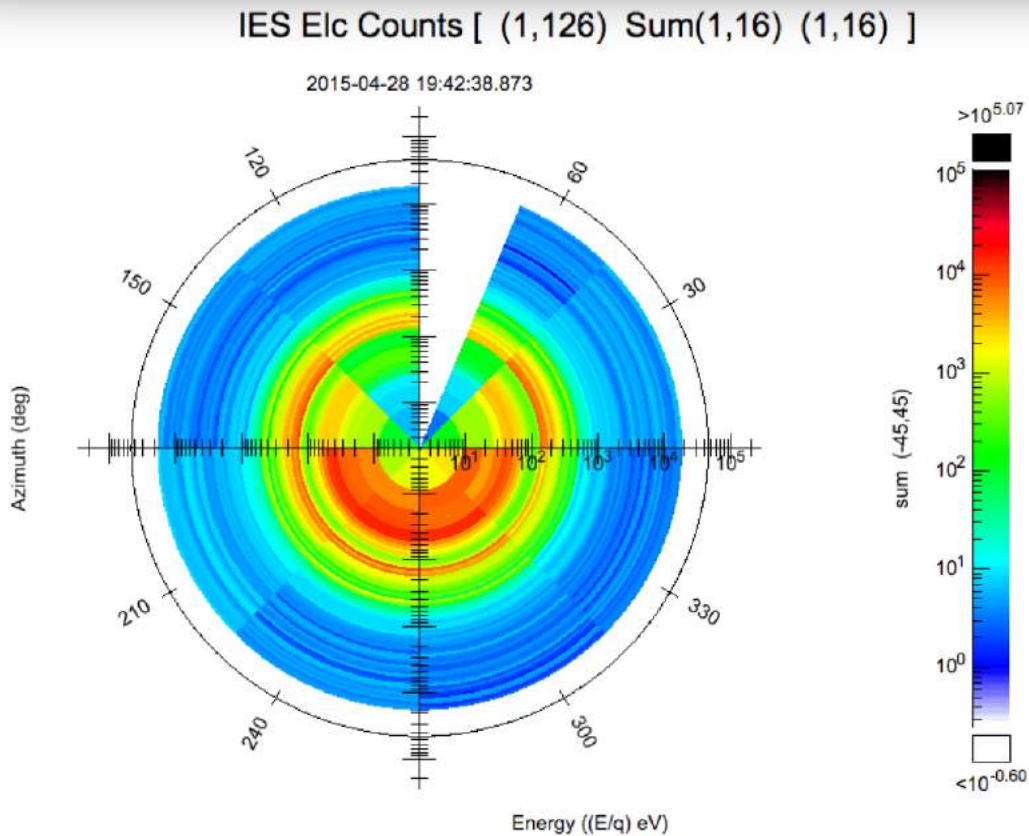
Colour Table: Rainbow Extended Colour bar label: sum (-45,45)

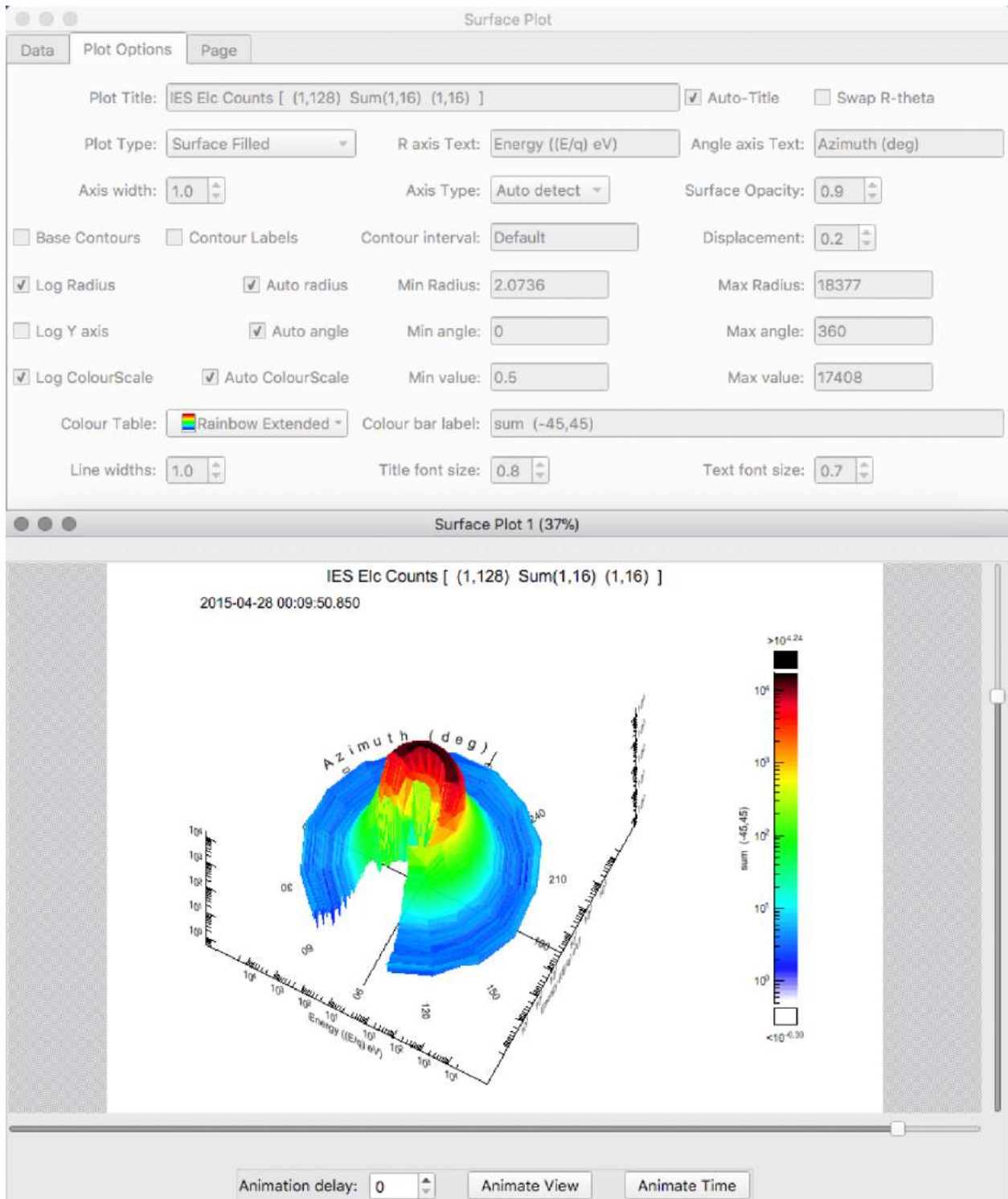
Title font size: 1.0 Text font size: 0.5  Phi as local time

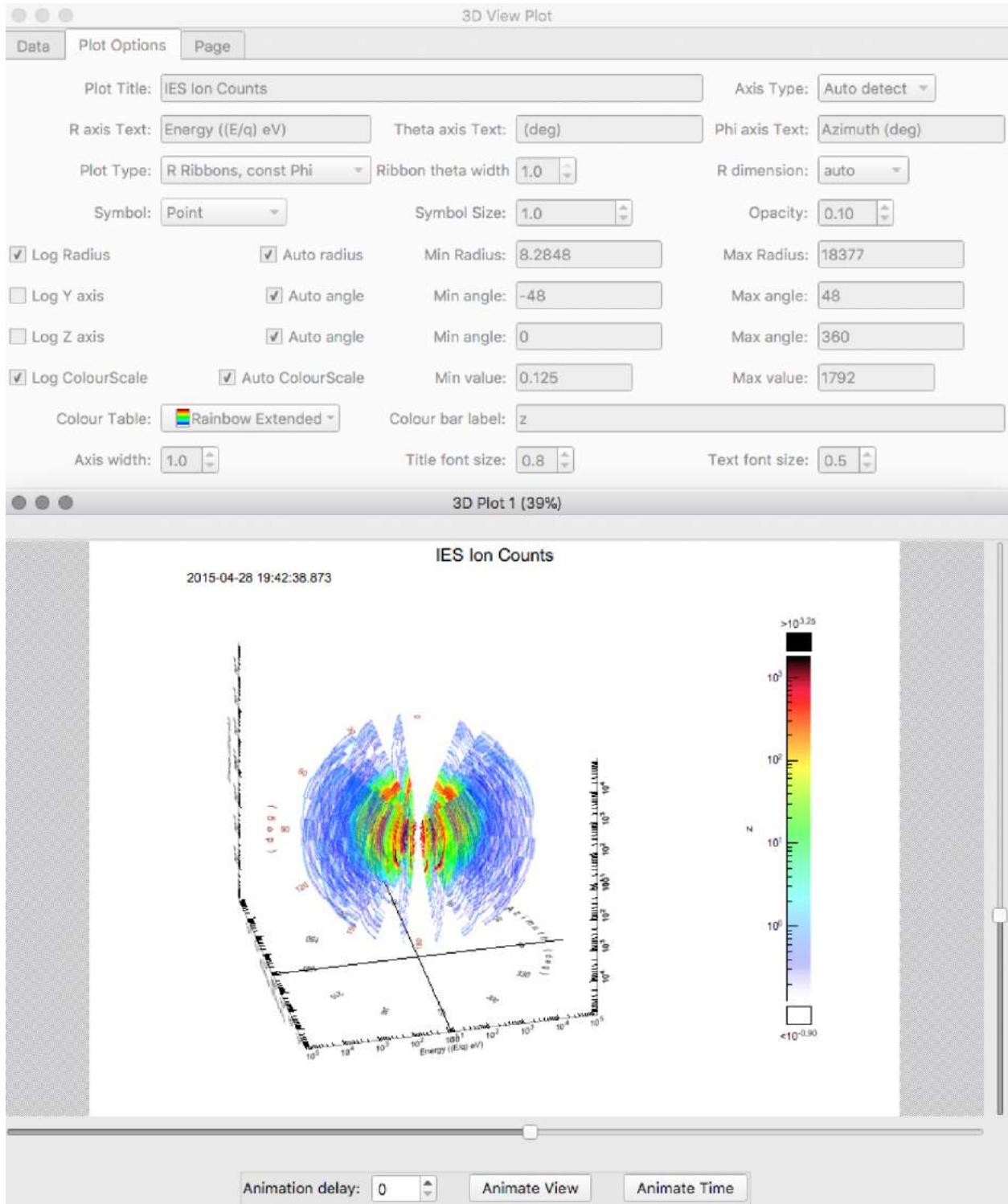
New Plot

New Plot

Plot Animate Time Dismiss



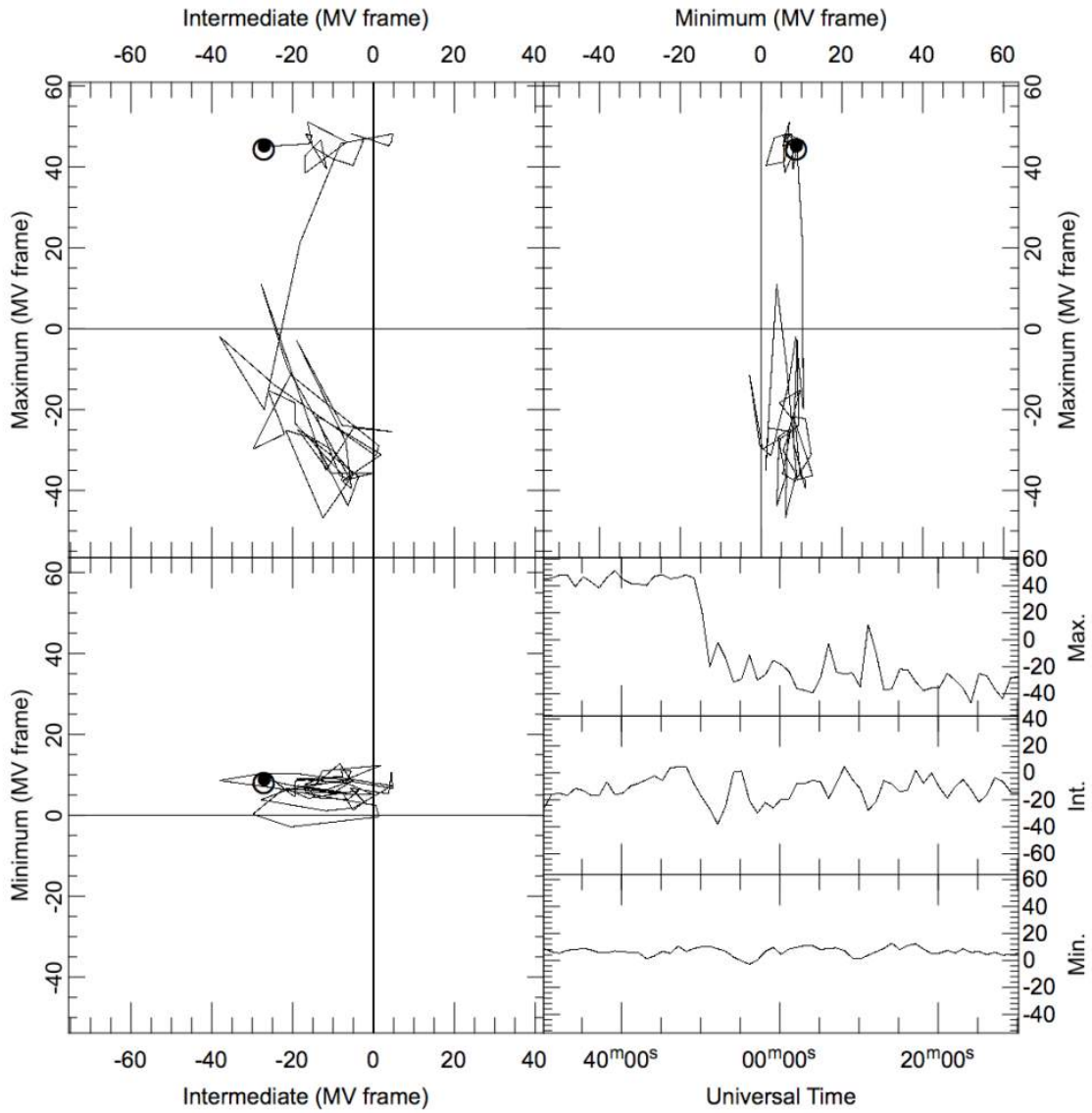




QSAS can also perform mathematical operations, combining data from different instruments to construct new parameters. The calculation shown below (for plasma beta) was constructed by drag-and-drop and click-and-place operations. Note that the pressures are converted to nPa before division to ensure the result is dimensionless. Common fundamental constants are



## Variance Analysis:



Time Interval (UT): 2015-10-15 00:30:09.520 - 01:30:09.520

Units: nT Frame: CSEQ\_xyz

$\lambda$	Direction
9.55	(-0.687, 0.169, -0.707)
85.4	(0.225, -0.876, -0.427)
1.22e+03	(-0.691, -0.452, 0.564)

QSAS can read several data formats, but to ensure compliant metadata is available to it, the option to download data from the PSA in CDF format should be used. QSAS will use this metadata to ensure units and coordinate frames are correct when manipulating data.

## Illumination maps

The purpose of the illumination maps is the visualisation of the conditions of illumination at 67P for a given configuration between the comet, the spacecraft and the Sun. The shape of the comet, so called shape model, has been reconstructed with the images acquired by the different instruments on board Rosetta. For this work, we have used the shape model from ESA/NAVCAM available [here](#).

The shape model is divided in two parts:

- the lines starting by the character "v": they are the positions (x,y,z) of the nodes considered for mapping the surface of the comet
- the lines starting by the character "f": these lines contain the nodes which you have to link together to make a facet. One facet, a triangle, requires three nodes.

For a given position of the Sun in the rotating frame of the comet, i.e. the longitude XXX and the colatitude YYY of the subsolar point, we calculate the cosine of the angle between the normal of the facet and the Sun direction. The values are set to 0 either they are lower than  $10^{-5}$  or if the facet is shadowed. They are sorted in the same order as the facets in the shape model.

We have generated maps for each degree in longitude (between 0 and 359) and colatitude (between 38 and 142 because of the obliquity of the comet). We preferred to use the colatitude instead of the latitude (colatitude= $90^\circ$ -latitude) for the convenience to be a positive value. As the same conditions of illumination are encountered several times due to the rotation of the comet, this is more relevant to provide illumination maps with respect to the configuration comet-Sun instead of the time. In total, we have produced 37800 maps.

The different products are available through different formats on the public portal VESPA.

- o VESPA: For visualization of illumination products

[VESPA](#) is a public portal regrouping different databases dedicated to planetary science. The illumination maps are available for the Target Name "67P" and the service is entitled "ILLU67P".

After selecting 67P and submitting, the user will reach the following page:

By clicking on ILLU67P, the user will access to the full database for the illumination maps.

**Results in service [ILLU67P](#)**

Show 10 entries

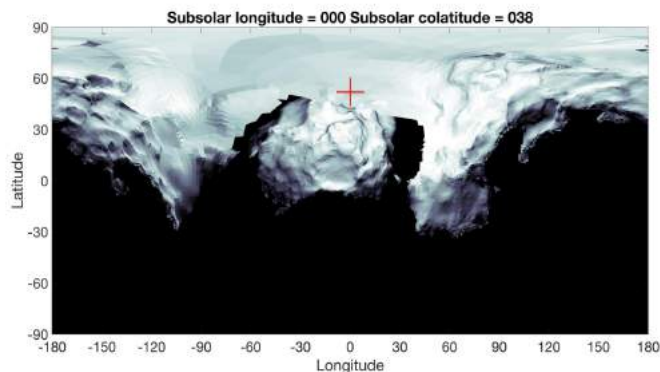
Column visibility Show all Hide all

Select All in current page Reset Selection

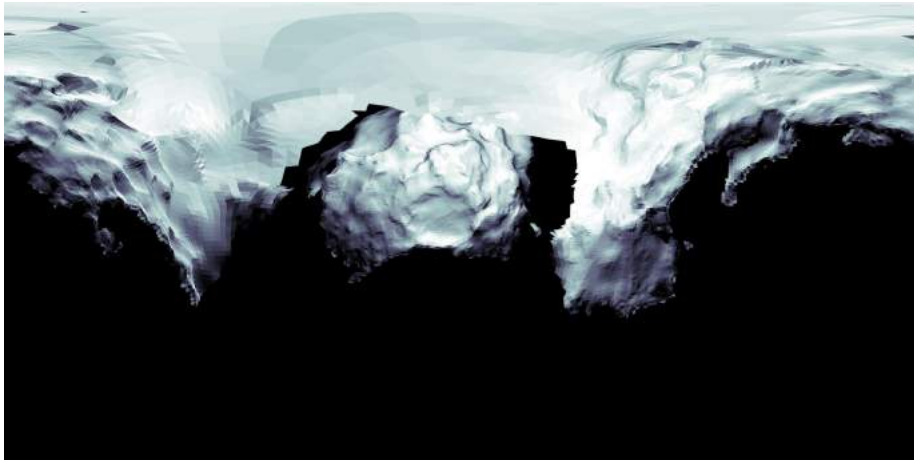
granule_uid	dataproduct_type	target_name	time_min (d)	time_max (d)	access_url
000-038-label	catalogue_item	67P	2014-01-01T00:00:30.239	2016-10-03T22:59:30.336	<a href="http://cdpp.irap.omp...">http://cdpp.irap.omp...</a>
000-038-map	map	67P	2014-01-01T00:00:30.239	2016-10-03T22:59:30.336	<a href="http://cdpp.irap.omp...">http://cdpp.irap.omp...</a>
000-038-preview	image	67P	2014-01-01T00:00:30.239	2016-10-03T22:59:30.336	<a href="http://cdpp.irap.omp...">http://cdpp.irap.omp...</a>
000-038-table	catalogue_item	67P	2014-01-01T00:00:30.239	2016-10-03T22:59:30.336	<a href="http://cdpp.irap.omp...">http://cdpp.irap.omp...</a>
000-038-votable	catalogue_item	67P	2014-01-01T00:00:30.239	2016-10-03T22:59:30.336	<a href="http://cdpp.irap.omp...">http://cdpp.irap.omp...</a>

Five different files are available:

- .TAB: these are the text files containing the cosines. The filenames are XXX-YYY-table.TAB.
- .VOT: same product as .TAB but in votable format
- .LBL: these are the text files containing the header of the corresponding .TAB files. The filenames are XXX-YYY-label.LBL. They have been designed to fulfil PSA requirements.
- .jpg: these are pictures in 2D of the illuminated surface of the comet, plotted in longitude and latitude. There are two versions with two different resolutions. The "preview" version has a low resolution, axes, title and the position of the subsolar point, represented by a red cross. The filenames are XXX-YYY-preview.jpg.



The "map" version is the raw version of the illuminated surface with higher resolution (4680x2340). The filenames are XXX-YYY-map.jpg.



The products can be directly reached with the following link:

<http://cdpp.irap.omp.eu/data/illu67p/labels/XXX-YYY-label.LBL>

<http://cdpp.irap.omp.eu/data/illu67p/votables/XXX-YYY-votable.xml>

<http://cdpp.irap.omp.eu/data/illu67p/tables/XXX-YYY-table.TAB>

<http://cdpp.irap.omp.eu/data/illu67p/previews/XXX-YYY-preview.jpg>

<http://cdpp.irap.omp.eu/data/illu67p/maps/XXX-YYY-map.jpg>

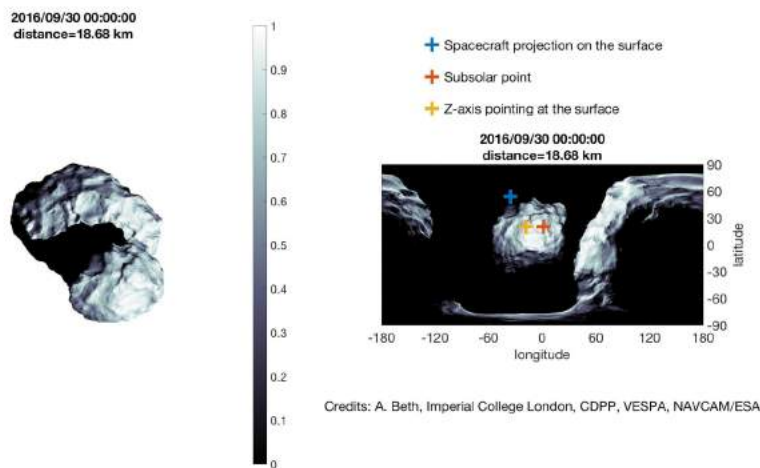
by replacing XXX and YYY with the corresponding longitude and colatitude, written with 3 digits (e.g. 001).

This feature is of particular interest if the user does not want to download/keep the maps on his computer and has a good internet connection (required a storage capacity of a few GB for the .TAB files). Some scripts have been written to exploit this particular aspect.

### o Matlab code for downloading directly from VESPA and visualizing

As the illumination maps are available through a public internet address, a few softwares allow to download them for a better, faster and easier utilisation. We have developed a computer program, written in MATLAB, to make the most of the illumination maps.

The MATLAB program, called `Illuminate_date.m`, plots for a given date the comet with the right illumination (or the closest configuration available) in 3D and 2D. It superimposes the subsolar point, the sub-spacecraft point and the coordinate of Rosetta Z-axis at the surface as well on the 2D map. Because the illumination maps are available every degree in longitude and latitude, we make a maximum error of  $0.5^\circ$  in longitude and latitude for the visualisation.



The function requires one input at least which is the time, float number corresponding to the number of days since Jan 0, 0000. The user can use the implemented "datenum" function to convert a date in the required format such as `Illuminate_date(datenum(2014,06,09))`. The time can be a scalar or a vector: `Illuminate_date(datenum(2014,06,09,0:12))` will plot the illumination every hour from Sep 09, 2014 for 12 hours.

The function requires to download in the same folder the file Illumination.mat containing the variables relative to the position of 67P and Rosetta: cometocentric distance, subsolar coordinate, etc...

The user does not have to care about it. Several features are available and are described in the MATLAB function and/or on the RPC wiki.

→ <http://chury.sp.ph.ic.ac.uk/rpcwiki/Archiving/XcalibrationSupport>

## **6. Guide on how to process the data including calibrations to be applied**

### RPC-ICA Data Processing

The RPC-ICA data format and a brief introduction to calibration are provided in the EAICD. Data format is also described in the data labels in the PSA archive. For instructions on how to use the data and how to apply calibration to raw data (if for any reason the provided calibrated data is not suitable) can be found in the RPC-ICA User Guide **[TO BE POSTED ON THE PSA in MARCH. PROVIDE FULL LINK when available]**.

### RPC-IES Data Processing

Formats and contents of all IES data files are described in the EAICD, and label files associated with the data files. Several other files and tables included in the datasets provide supplementary information required to understand the data and convert to physical quantities. These files are listed in the EAICD and also have descriptions in associated label files. All data and table files are in ASCII format and may be read, processed and analyzed using any tool or programming language capable of doing so. The format within the data file is a flat table of counts or flux values that can be converted to a multidimensional table representing time, energy, elevation and azimuth. Conversion of level two data to level three data is described in the FLUX\_CALCULATION\_V\*.PDF document in the DOCUMENT/FLUX\_CALCULATION directory on the PSA in RPCIES Level 3 datasets only.

## List of useful files

RPC – IES List of useful supplementary files within the datasets	
DOCUMENT/IES_EAICD/10991-IES-EAICD-*.PDF	The IES EAICD
CALIB/ENERGY_STEPS.TAB	Energy step to electron-volts mapping
CALIB/ELEVATION_ANGLES.TAB	Elevation step to angle (degrees) mapping
CALIB/AZIMUTH_ANGLES.TAB	Anode/azimuth number to angle (degrees) mapping
CALIB/IES_MODES.TAB	Detailed information about instrument operating modes
CALIB/POLAR_SECTORS.TAB	Polar sector in SPICE kernels to ion and electron elevation step mapping
CALIB/STEP_INTEGRATION.TAB	Cycle length to step integration time mapping
CALIB/ELC_FLIGHT_G.TAB	Geometric factor for electrons
CALIB/ION_FLIGHT_G.TAB	Flight geometric factor for ions
DOCUMENT/FLUX_CALCULATION/FLUX_CALCULATION.PDF	Procedure for converting level 2 products to level 3

## Geometry Reference Systems

IES field of view definitions, anode and elevation sizes, their orientations with respect to the spacecraft and frame definitions are described in the SPICE kernels defined and provided by Navigation and Ancillary Information Facility (NAIF) on the NASA website (files also available on the PSA side). At the time of writing of this document, the filenames for the latest versions of these instrument kernel and frame kernel files were ROS\_RPC\_V19.TI and ROS\_V31.TF, respectively.

These kernels can be loaded and used to determine the position and attitude of the spacecraft, orientation of the IES instrument, look directions of anodes and elevations in any coordinate system at any given time. The frame internal to the instrument is called ROS\_RPC\_IES. This can be used as a reference when converting pointing information to and from other reference frames such as the Rosetta spacecraft, comet-centric or heliocentric frames.

## RPC-LAP Data Processing

*XXX Input missing from LAP XXX*

## RPC-MAG Data Processing

### Generation of scientific usable Magnetic Field Data

The magnetic field data measured by the IB and OB sensor are originally given in raw ADC-counts in instrument coordinates. To generate the highest level data product - reaction wheel corrected magnetic field data in e.g. cometo centric solar equatorial coordinates (CSEQ) - a chain of sophisticated calibration steps is needed. This chain is described partly in the “*RPC-MAG Experiment to Archive Interface Control Document (EAICD)*” RO-IGEP-TR0009. In depth details can be found in the “*Step by Step Calibration Procedure for RPC-MAG data*” RO-IGEP-TR0028 [[ftp://psa.esac.esa.int/pub/mirror/INTERNATIONAL-ROSETTA-MISSION/RPCMAG//RO-X-RPCMAG-4-CVP-RESAMPLED-V3.0/DOCUMENT/CALIBRATION/RO\\_IGEP\\_TR0028.PDF](ftp://psa.esac.esa.int/pub/mirror/INTERNATIONAL-ROSETTA-MISSION/RPCMAG//RO-X-RPCMAG-4-CVP-RESAMPLED-V3.0/DOCUMENT/CALIBRATION/RO_IGEP_TR0028.PDF)].

## RPC-MIP Data Processing

RPC-MIP guides on how to process the data including calibrations to be applied

The calibration of RPC-MIP mutual impedance spectra (L3) is described in the RPC-MIP user guide [NEED A LINK].

The derivation of RPC-MIP plasma density (L5) from the RPC-MIP mutual impedance spectra is described in the RPC-MIP user guide.

The cross-calibration of RPC-MIP and RPC-LAP data to produce the cross-calibrated MIPLAP\_HTR [TBD] plasma densities are described in the MIP-LAP cross calibration report. [Future plan when dataset products generated]

## 7. Example dataset time period which can be used to learn processing steps

**To all teams: to illustrate dataset for 30 July 2016.**

### RPC-ICA Data

As discussed in more detail in the RPC-ICA User Guide the instrument initially suffered from automatic shut-downs and associated restricted operating hours, as well as data corruption giving frequent shorter time period data gaps. The situation improved with time, so to get started it may be better to look at data from perihelion and onward. In particular data is better after 1 November 2014 when the energy tables were updated. The overview given in Nilsson et al. (2017) can be used to find the type of data one wish to study. An example used in the RPC-ICA User manual is 2016-03-09 which consists of standard 3D data with full energy range. The data show  $H^+$ ,  $He^{2+}$  and  $He^+$  of solar wind origin as well as cometary ions accelerated up to approximately the energy of the solar wind ions.

### RPC-IES Data

The data from 1 October 2014 is a good place to start. The solar wind protons and alphas are in the field of view except for ~2 hrs near noon when Rosetta performed a turn. This is obvious in the ion data but not in the electron data, except perhaps for some interference at ~13:00 UT. The ion signal at the lowest energies is the result of ions newly created by photoionization and attracted to the negative potential of the S/C. During this period Rosetta was ~18 km from the comet and ~3.3 AU from the Sun. See the references listed in a previous section and the EAICD for more details.

### RPC-LAP Data

*Input missing for LAP XXXXX*

### RPC-MAG Data

For scientific use the data with the highest available time resolution should be used. Furthermore the magnetic field should initially be analyzed in a celestial coordinate system; therefore data are provided in ECLIPJ2000 system for the pre-comet phase and in the CSEQ-System (comet centric solar equatorial coordinates) for the comet phase. This means that CALIBRATED Burst mode data (M3) of LEVEL\_C (CLC) should be the first choice. Data are disturbed by reaction

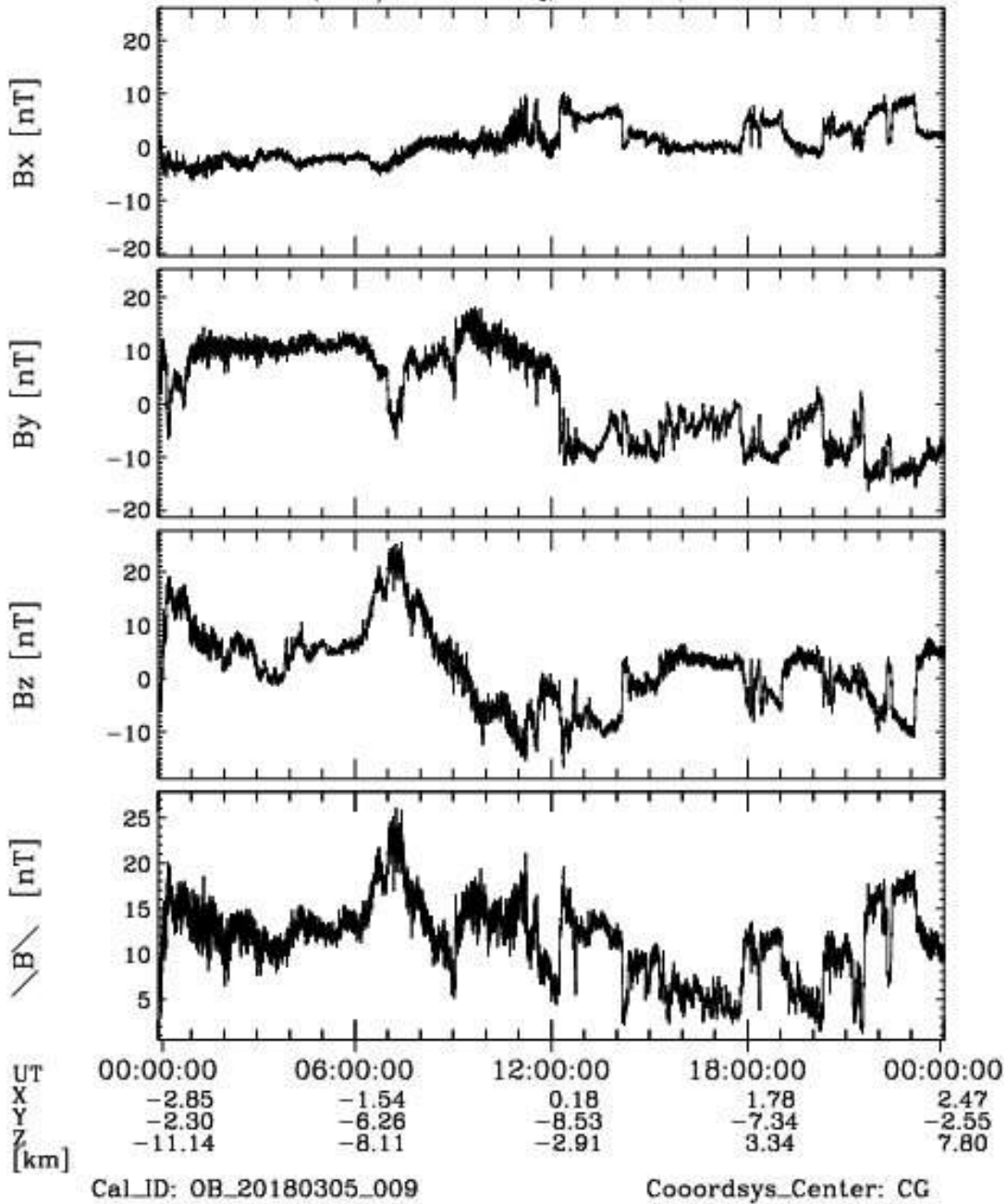
wheels, therefore a huge effort has been taken to eliminate this impact from the data. Thus for intervals where this correction was successful, RESAMPLED LEVEL\_Hdata are provided and should be used preferentially. All these datafiles contain the s/c-position as well. Thus full geometry information is available.

In order to use the right instrument offset and the s/c-residual field, observations close to magnetic cavities are best, as the external field should per definition be identical to zero in the cavity (see Goetz et al. 2016b MNRAS).

On the other hand, phases characterized by huge external magnetic fields are valuable as well, as during these intervals the offset and s/c-residual fields are playing a negligible role.

As an example of data, observations from July 30, 2016 are shown in the following picture. The MAG-instrument was in normal mode all the day. The observations taken are displayed in CSEQ-coordinates. Besides the three magnetic field components also the magnitude is plotted as well. At the bottom of the plot the coordinates of ROSETTA with respect to the comet are displayed in the CSEQ frame accordingly.

July 30, 2016 RPC-MAG-OB 1.0 s  
 CAL.DATA,67P/C-G\_CSEQ,LEVEL\_C, MODE:SID2



## RPC-MIP Data

The plasma density (L5) are obtained from the MIP active spectra (L3) under certain plasma conditions, that enable to identify the plasma frequency line on the MIP spectrograms.

Users are encouraged to check that the plasma frequency line is clearly visible on the MIP active electric spectrograms (L3) [*graph to be shown for example with disparition of plasma frequency line - TBD*]. Time intervals [*example to be given - TBD*] when the plasma frequency line is not visible in the MIP active electric spectrograms are such that the MIP density (L5) is not retrieved. The users are therefore encouraged to start learning how to use the MIP data using the period **May-September 2016**, during which an almost complete coverage of plasma density is provided. During this interval, users are encouraged to start with time periods during which MIP is operated in burst mode and in LDL and/or in SDL phased mode.

The figure below shows MIP data acquired in active SDL mode for July 30, 2016. Some instrument operational parameters are shown in the top panel as color bars, giving information on the transmission configuration. The second panel shows the color-coded frequency-time spectrogram of active mutual impedance spectra between 0 dB and 30 dB. Note that an operating mode change occurred around 13:30, resulting in variation in the instrument frequency range. While the plasma frequency line is clearly observed on the spectrogram, it is contaminated by some interferences (appearing as high amplitude horizontal line(s)) and by a fluctuating signal-to-noise ratio along the day. To bypass these issues when analysing the plasma line, it can be useful to process RPCMIP spectra by removing the strongest interference(s) and normalizing spectra individually to better highlight the resonance or the cut-off around the plasma frequency. This is illustrated in the third panel, where the plasma line is highlighted as the blue-to-red sharp transition. The fourth panel gives the phase of the mutual impedance spectra, normalized individually as in the previous panel. While the interpretation of RPCMIP phase data is somehow intricate and requires some level of modelling, the information contained there is usually valuable to validate results obtained on the power spectra. As active measurements only are used to derive the plasma density, the passive MIP measurements are not shown here. They usually contain less information to extract the the plasma density and cannot be interpreted without a dedicated processing step. The bottom panel gives the result from an automatic plasma line derivation from the power active spectra, converted to density and shown as grey diamonds, with a moving median density overplotted as a red line.



## 8. List of caveats - problems with data contents, format

### RPC-ICA Data Caveats

RPC-ICA data may contain a few types of known problems. The most notable as yet unexplained types of data include a real-looking signal below the spacecraft potential, possibly sometimes at invalid energy analyser settings which should not yield any external signal. These signals were mentioned in Nilsson et al. (2017) and are described in more detail in the RPC-ICA User Guide [\[Add link to the User Guide when available on PSA\]](#).

### RPC-IES Data Caveats

There are several issues that the user of IES data needs to be aware of and understand before processing and interpreting the data. These are described in section 2.5, “Data Caveats” within the EAICD.

Additionally, data are marked with quality flags that describe either specific characteristics of data, the non-nominal state of the instrument at that time or spacecraft pointing with regards to IES. The quality flags are described in each label file associated with data files and relate to (1) MCP Voltage (2) Sun Pointing (3) Interference from the RPC-ICA instrument (4) Transition Cycle (5) Enhanced counts due to possible penetrating radiation.

#### Blockage of Some Elevation Angle Bins

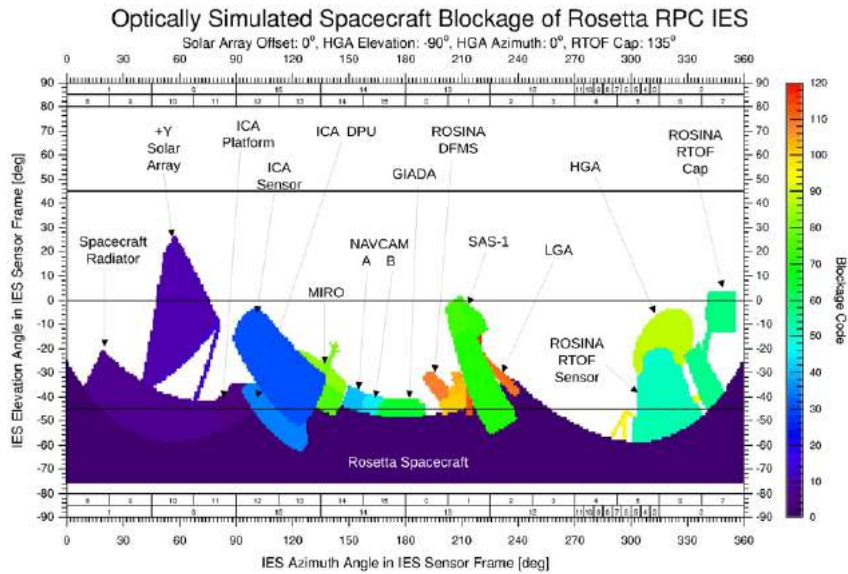
Several S/C structures and parts of other instruments block the IES FOV in portions of the most negative elevation angles. See the accompanying figure for an example. In particular, note that the positions of the solar arrays and the HGA in the IES FOV vary throughout the mission.

#### Geometric Factor

The documented IES geometric factor was obtained by combining results of ray tracing, flight calibration, and laboratory measurements.

#### Geometric Factor

The documented IES geometric factor was obtained by combining results of ray tracing, flight calibration, and laboratory measurements.



### Individual Anode (Azimuth) Characteristics

Sometimes anode data are combined on board in certain operating modes because of telemetry limitations. In those cases each of the anodes is given identical values (sum/number of anodes).

#### *Ions*

Anodes 13 and 14 are often noisy so caution is recommended when using data from them.

The so-called "fine anodes" (3 - 11) are sometimes combined on board in certain operating modes because of telemetry limitations. In those cases each of these 9 anodes are given identical values (the sum/9).

The data from individual fine anodes, when provided, suffer from crosstalk between these anodes and thus may not be reliable.

It was discovered after launch, apparently as a result of a light leak, that when the sun is incident between anodes 2 and 3, a high count rate is seen in anode 12. It is also seen in anode 13 when counts in 12 and 13 are combined.

#### *Electrons*

Occasionally the electron data exhibit a signal at narrow energy ranges between 200-2000 eV, appearing as short dashes in spectrograms, as a result of interference from a neighboring instrument (ICA). The occurrences are indicated in the flag column.

Anode 11 became noisy shortly after launch and since 16 September 2007 data from that anode have not been downloaded. In those operating modes for which data from 2 or more anodes are combined will result in the absence of data from one or more anodes adjacent to number 11.

## RPC-LAP Data Caveats

*Input missing from LAP XXXX*

## RPC-MAG Data **Caveats**

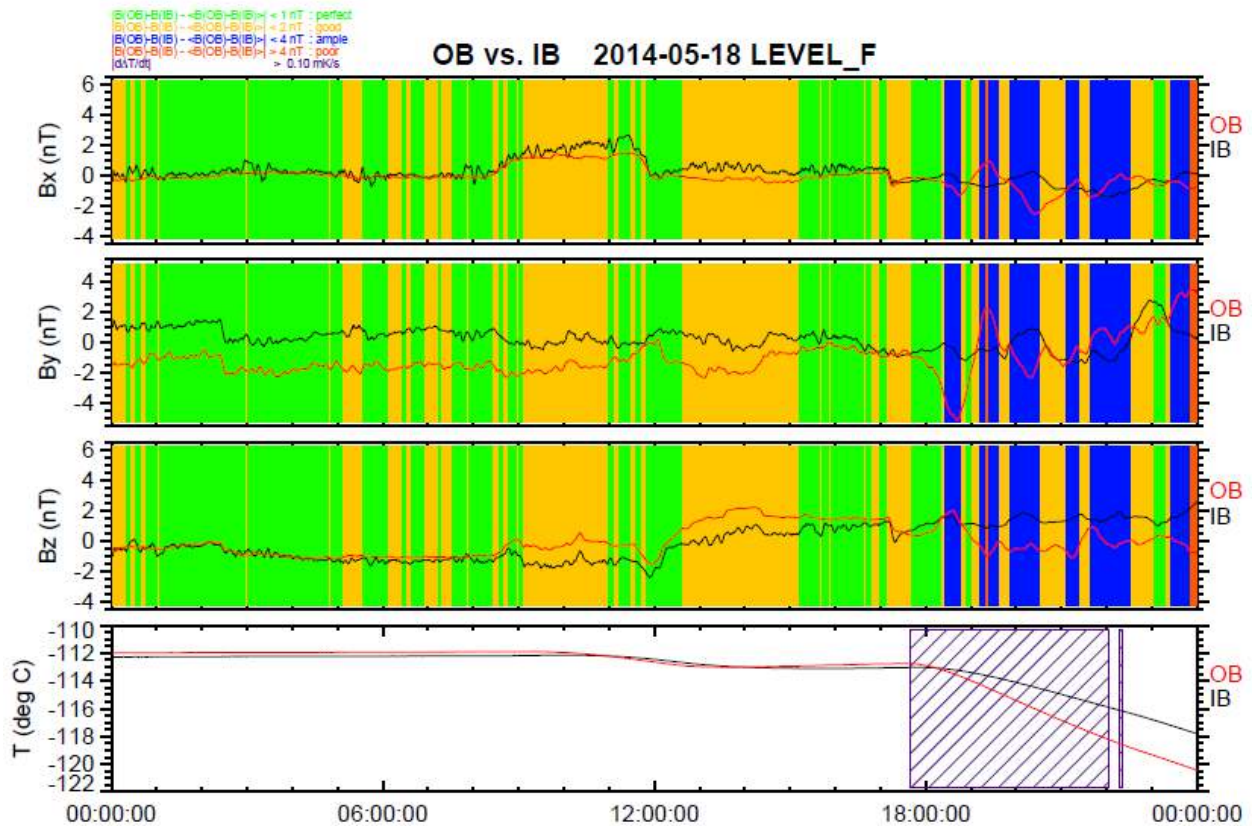
The data from 1 October 2014 is a good place to start. The solar wind protons and alphas are in the field of view except for ~2 hrs near noon when Rosetta performed a turn. This is obvious in the ion data but not in the electron data, except perhaps for some interference at ~13:00 UT. The ion signal at the lowest energies is the result of ions newly created by photoionization and attracted to the negative potential of the S/C. During this period Rosetta was ~18 km from the comet and ~3.3 AU from the Sun. See the references listed in a previous section and the EAICD for more details.

The magnetic field sensors are very sensitive to various disturbance sources located on the spacecraft. Main disturbers are :

- Thrusters (movable magnetic valves), critical during phases of Wheel off-Loading (WOL) and Orbit Correction Manoeuvres (OCM)
- Currents (e.g. Lander power ESS, Heaters )
- Reaction wheels (rotating magnets, signatures appear aliased in the magnetic field data)

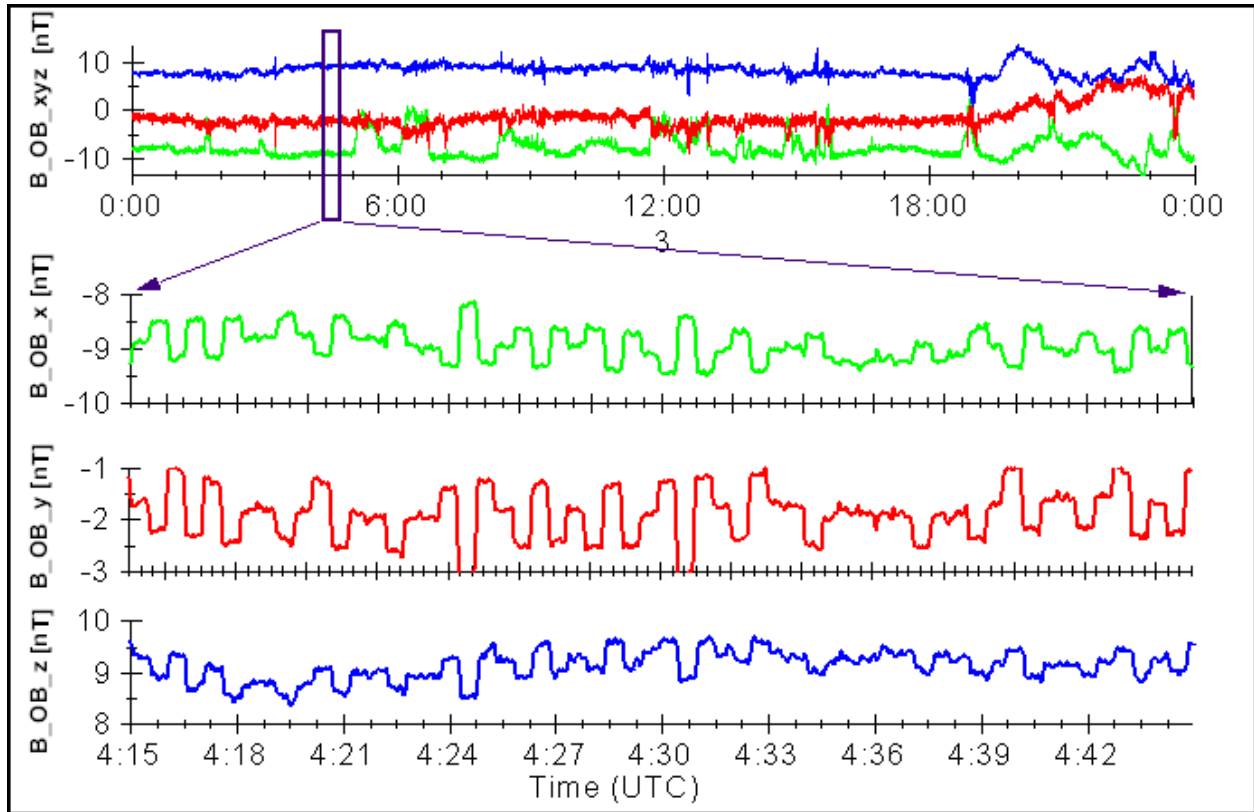
Furthermore s/c attitude changes can cause non equilibrium temperature changes on both magnetic field sensors shifting the sensors offsets. In general this is considered in an advanced sensor temperature model but remaining offset residual can occur.

The next figures show examples of disturbed data by different sources:



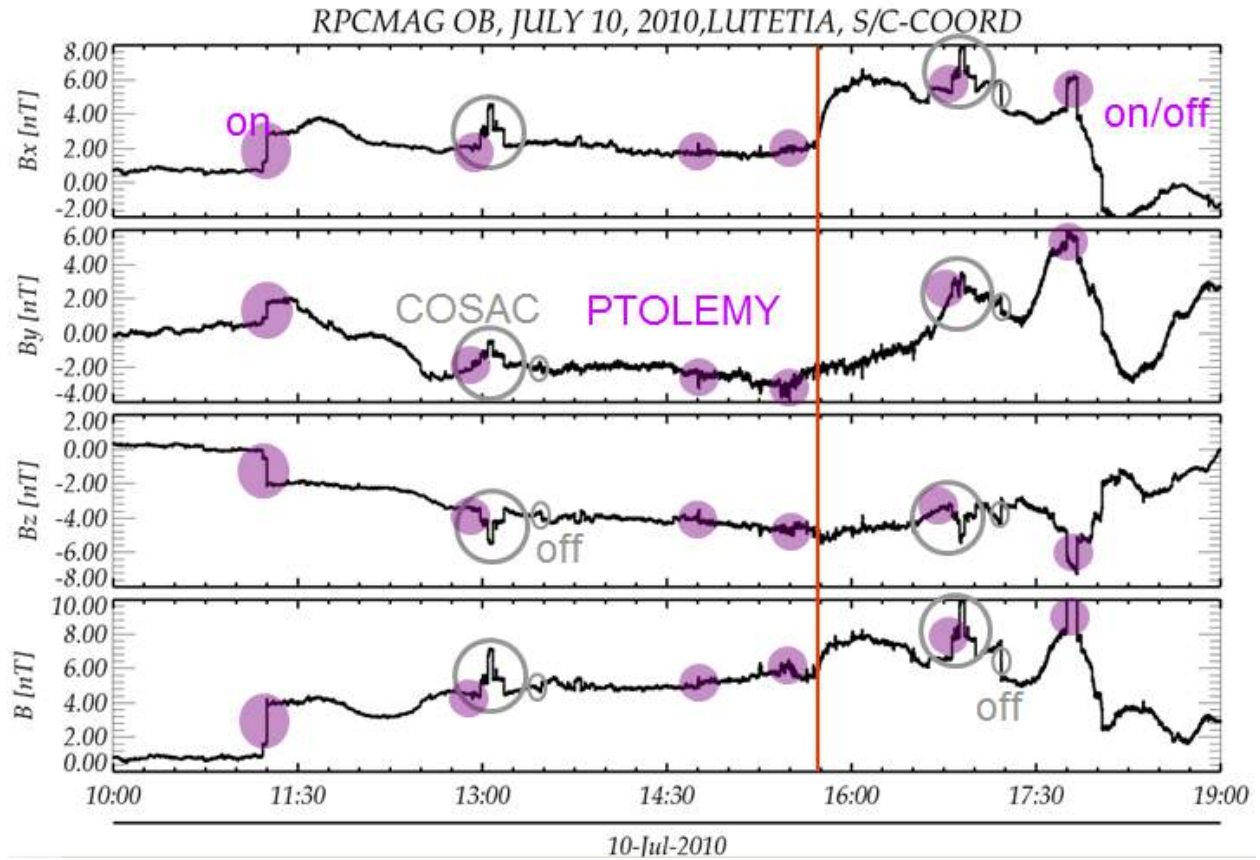
This Figure shows OB and IB data for a whole day. In times where the sensor temperature is stable, the magnetic field data of both sensor show similar behavior as expected (IB is always more influenced by s/c disturbance and noise due to a closer location to the s/c body.) Attitude changes can cause different temperature changes and ,therefore, different magnetic field readings due to limited H/W temperature correction possibilities and a limited temperature calibration model. The color coding reflects the quality of the data. E.G. green means that the difference between the OB and IB data and the mean difference of OB and IB over the whole day are less than 1 nT which means an excellent quality. For orange flagged data, however, the difference is more than 4 nT due to s/c effects or temperature drifts.

Remark: The new calibration model (V9.0) of 2018 generates much better data than the older models used temporarily during the mission.

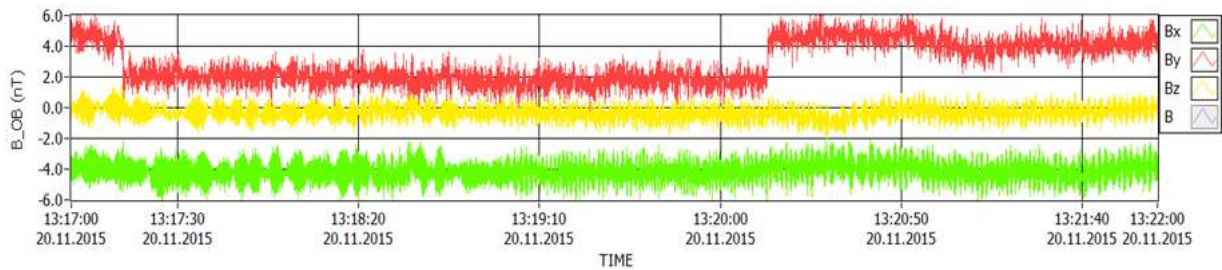


2005-03-01

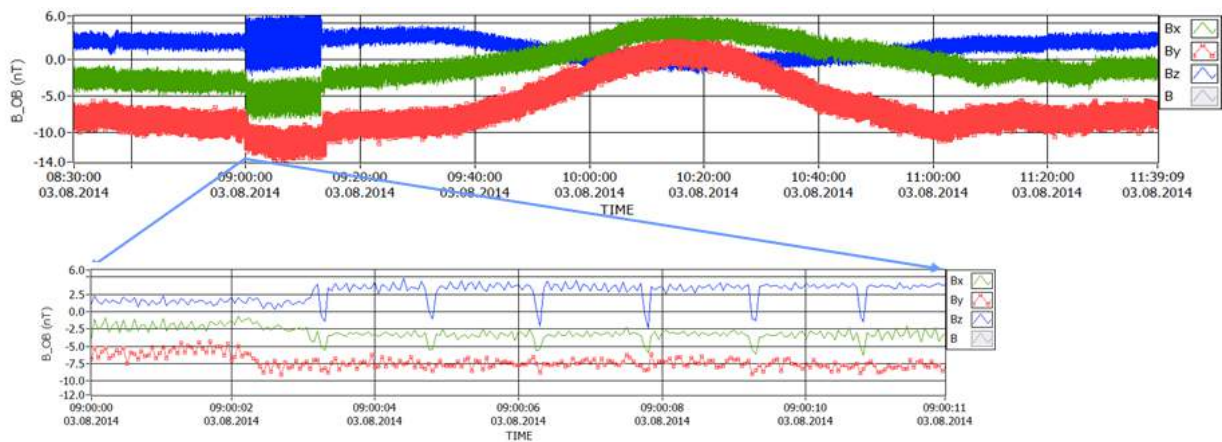
Influence of PHILAE Heater currents. During the first Earth Fly by heaters on the Lander were activated with ~1 min period. The heater current are causing magnetic field disturbances in the order of 1 nT.



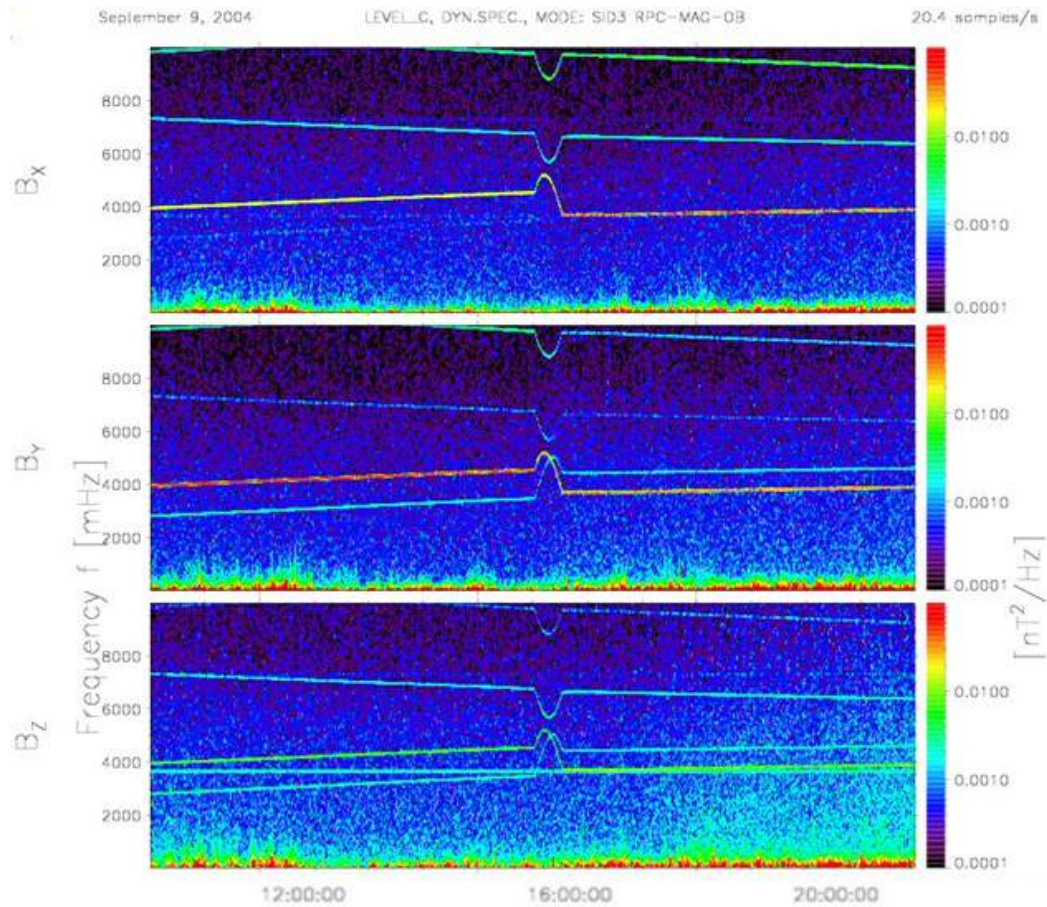
Influence of supply currents drawn by the PTOLEMY and COSAC experiments. The figure shows specific disturbance patterns in the order of 2 nT caused by the operation of the mentioned instruments.



This figure displays the disturbance by thruster activation during WOLs. A clear shift of the s/c residual field in the order of ~3nT can be seen while the latch valves of the thrusters are activated. The WOL activation is deterministic and known, thus these periods can be flagged as bad data.

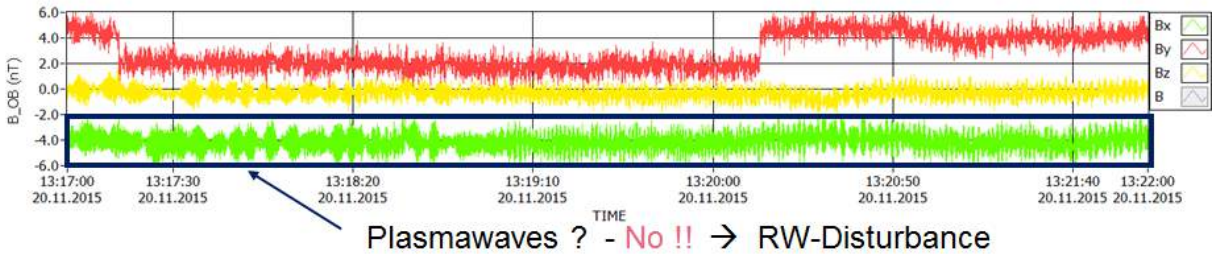


Disturbance by thruster activation during OCMs. Besides DC-jumps of  $\sim 2\text{nT}$  additional AC spikes of  $\sim 6\text{nT}_{\text{pp}}$  Spikes, at  $\sim 625\text{ mHz}$ , and  $\sim 200\text{ ms}$  width appear. An automatic cleaning of these structures is hardly possible, but the data in these intervals will be flagged as bad data in the final datasets.

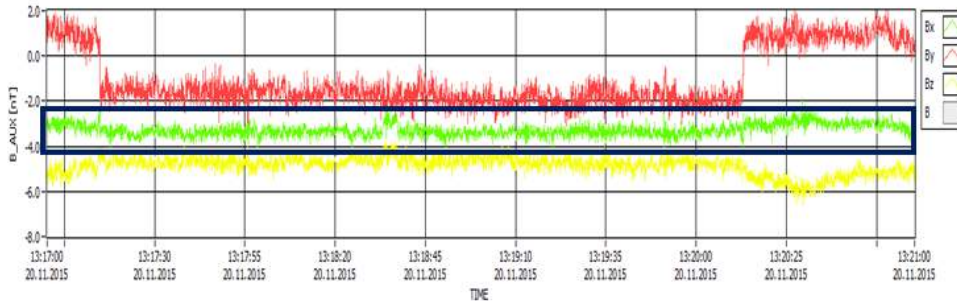


Here a typical dynamic power density spectrum of the magnetic field is shown for 16 hours of data. The tilted traces in the spectra represent the impact of the 4 s/c reaction wheels rotating at variable frequencies. They are causing dynamic disturbances in the 1-10 Hz range at amplitudes of  $\sim 2$ nT. As these frequencies are known at any time, an automatic elimination is possible. Data without reaction wheel impact are delivered for the OB sensor in burstmode as RESAMPLED LEVEL\_H data.

LEVEL\_C : CALIBRATED Data



LEVEL\_H: RESAMPLED, Reaction Wheel Corrected data



This figure shows the impact of the reaction wheels in the timeseries. On the upper panel a nice plasma wave structure might be hypothesized. However, a view to the reaction wheel impact eliminated LEVEL\_H data in the lower panel clearly depicts, that there are no plasma waves present but only higher frequent disturbances.(data shifted due to enhanced visibility).

All the examples above show that there is a lot of s/c influence diminishing the quality of the magnetic field data. As is it in many cases not possible to eliminate these effects automatically the data will only be flagged by certain designators. Each magnetic field vector in the calibrated data files is flagged with a string of digits. The meaning of these digits is explained in the related label files \*.lbl, and the EAICD. In general, the lower the value of such a digit (0..9) the better the quality. Furthermore, an "x" means that there is no quality assessment of that specific property.

**Thus, a user of the data - YOU! - has to be aware of the specific quality of the present data before doing any serious science analyses using these data!**

Special care must be exercised calculating the field magnitude or derived angles.

For the magnitude

$$|B| = \sqrt{\sum_i (B_i + Off_i)^2}$$

the root of the sum of squared offset and s/c-residual afflicted magnetic field components has to be calculated. With uncertain s/c-residual field- and offset-components the magnitude becomes uncertain in a non-linear way, possibly depicting a strange trend. This is not only a simple additive shift but a variable displacement, possibly leading to misinterpretation.

When calculating angles of the magnetic field

$$\alpha = \arctan \left( \frac{B_i + Off_i}{B_j + Off_j} \right)$$

the same care has to be exercised. The division of entities of the same order which are afflicted by errors can produce very uncertain results, especially if the error are in the order of the actual field components. Thus be careful when calculating and interpreting angles!

An additional point which should be mentioned here is the filtering of the data. Burst mode OB data are sampled with 20 Hz and pass all the processing chain unchanged from the instrument via telemetry to the calibration pipeline. The normal mode data, however, show an effective vector rate of 1Hz, which is accomplished by digital filtering inside PIU, using a two stage FIR decimator with -3 dB cutoff at 0.3 Hz and final damping of about -130 dB starting at ~1.8 Hz. This very steep filter characteristic was also used for the generation of 1s averaged data for the RESAMPLED datasets, in order to keep the spectral characteristics of the normal mode data also for the averaged burst mode data. Otherwise the noise properties would have changed within one datafile at the transitions from one mode to another. Therefore, RESAMPLED data are good for quicklook purposes, but should not be used for wave investigations as the amplitudes in the 0.1 - 0.5 Hz range are damped much more as if have been filtered by a standard - even higher order - 1Hz Butterworth lowpass. Thus for spectral analyses the original burst mode data should be used if available.

### RPC-MIP Data Caveats

The plasma density (L5) are obtained from the MIP active spectra (L3) under certain plasma conditions, that enable to identify the plasma frequency line on the MIP spectrograms. The known caveats on the MIP L3 and L5 data are described in the RPC-MIP user guide [[NEED TO ADD LINK ON THE PSA](#)].

Note also that a quality value is associated with each density value given in the PSA archive. The user is strongly encouraged to consider using it.

## 9. List of science papers where further information can be found

*To re-order in alphabetic order of the sensors.*

RPC Science Papers where RPC sensors are presented or dataset is discussed	
Full Reference	RPC sensors concerned
PAPERS LED BY PIU or KEY PIU papers (but not led by another RPC sensor team, as those papers are cited under the relevant sensor team)	
Carr, C., Cupido, E., G. Y. Lee, C., Balogh, Andre., Beek, T., L. Burch, J., Dunford, C., Eriksson, A., Gill, R., Glassmeier, K-H., Goldstein, R., Lagoutte, D., Lundin, R., Lundin, K., Lybekk, B., L. Michau, J., Musmann, G., Nilsson, H., Pollock, C., G. Trotignon, J. (2007), RPC: The Rosetta plasma consortium, <i>Space Science Reviews</i> , 128, 629-647, doi: 10.1007/s11214-006-9136-4.	PIU, ICA, IES, LAP, MAG, MIP
M. Galand, K. L. Héritier, E. Odelstad, P. Henri, T. W. Broiles, A. J. Allen, K. Altwegg, A. Beth, J. L. Burch, C. M. Carr, E. Cupido, A. I. Eriksson, K.-H. Glassmeier, F. L. Johansson, J.-P. Lebreton, K. E. Mandt, H. Nilsson, I. Richter, M. Rubin, L. B. M. Sagnières, S. J. Schwartz, T. Sémon, C.-Y. Tzou, X. Vallières, E. Vigren, P. Wurz; Ionospheric plasma of comet 67P probed by <i>Rosetta</i> at 3 au from the Sun, <i>Monthly Notices of the Royal Astronomical Society</i> , Volume 462, Issue Suppl_1, 16 November 2016, Pages S331–S351, <a href="https://doi.org/10.1093/mnras/stw2891">https://doi.org/10.1093/mnras/stw2891</a> .	PIU illumination maps (Figures), IES, LAP, MAG, MIP
E. Grün, J. Agarwal, N. Altobelli, K. Altwegg, M. S. Bentley, N. Biver, V. Della Corte, N. Edberg, P. D. Feldman, M. Galand, B. Geiger, C. Götz, B. Grieger, C. Güttler, P. Henri, M. Hofstadter, M. Horanyi, E. Jehin, H. Krüger, S. Lee, T. Mannel, E. Morales, O. Mousis, M. Müller, C. Opitom, A. Rotundi, R. Schmied, F. Schmidt, H. Sierks, C. Snodgrass, R. H. Soja, M. Sommer, R. Srama, C.-Y. Tzou, J.-B. Vincent, P. Yanamandra-Fisher, M. F. A'Hearn, A. I.	LAP, MIP, IES, MAG

<p>Erikson, C. Barbieri, M. A. Barucci, J.-L. Bertaux, I. Bertini, J. Burch, L. Colangeli, G. Cremonese, V. Da Deppo, B. Davidsson, S. Debei, M. De Cecco, J. Deller, L. M. Feaga, M. Ferrari, S. Fornasier, M. Fulle, A. Gicquel, M. Gillon, S. F. Green, O. Groussin, P. J. Gutiérrez, M. Hofmann, S. F. Hviid, W.-H. Ip, S. Ivanovski, L. Jorda, H. U. Keller, M. M. Knight, J. Knollenberg, D. Koschny, J.-R. Kramm, E. Kührt, M. Küppers, P. L. Lamy, L. M. Lara, M. Lazzarin, J. J. López-Moreno, J. Manfroid, E. Mazzotta Epifani, F. Marzari, G. Naletto, N. Oklay, P. Palumbo, J. Wm. Parker, H. Rickman, R. Rodrigo, J. Rodriguez, E. Schindhelm, X. Shi, R. Sordini, A. J. Steffl, S. A. Stern, N. Thomas, C. Tubiana, H. A. Weaver, P. Weissman, V. V. Zakharov, M. G. G. T. Taylor; The 2016 Feb 19 outburst of comet 67P/CG: an ESA Rosetta multi-instrument study, <i>Monthly Notices of the Royal Astronomical Society</i>, Volume 462, Issue Suppl_1, 16 November 2016, Pages S220–S234, <a href="https://doi.org/10.1093/mnras/stw2088">https://doi.org/10.1093/mnras/stw2088</a>.</p>	
<p>K. L. Heritier, P. Henri, X. Vallières, M. Galand, E. Odelstad, A. I. Eriksson, F. L. Johansson, K. Altwegg, E. Behar, A. Beth, T. W. Broiles, J. L. Burch, C. M. Carr, E. Cupido, H. Nilsson, M. Rubin, E. Vigren; Vertical structure of the near-surface expanding ionosphere of comet 67P probed by Rosetta, <i>Monthly Notices of the Royal Astronomical Society</i>, Volume 469, Issue Suppl_2, 21 July 2017, Pages S118–S129, <a href="https://doi.org/10.1093/mnras/stx1459">https://doi.org/10.1093/mnras/stx1459</a>.</p>	<p>PIU illumination maps (Video), IES, LAP, MIP</p>
<p>M. Hoang, K. Altwegg, H. Balsiger, A. Beth, A. Bieler, U. Calmonte, M. R. Combi, J. De Keyser, B. Fiethe, N. Fougere, S. A. Fuselier, A. Galli, P. Garnier, S. Gasc, T. Gombosi, K. C. Hansen, A. Jäckel, A. Korth, J. Lasue, L. Le Roy, U. Mall, H. Rème, M. Rubin, T. Sémon, D. Toublanc, C.-Y. Tzou, J. H. Waite, P. Wurz; The heterogeneous coma of comet 67P/ Churyumov-Gerasimenko as seen by ROSINA: H<sub>2</sub>O, CO<sub>2</sub>, and CO from September 2014 to February 2016 A&amp;A 600 A77 (2017) DOI: 10.1051/0004-6361/201629900</p>	<p>PIU illumination maps (figures)</p>
<p>A.D. Morse, K. Altwegg, D.J. Andrews, H.U. Auster, C.M. Carr, M. Galand, F. Goesmann, S. Gulkis, S. Lee, I. Richter, S. Sheridan,</p>	<p>MAG</p>

<p>S.A. Stern, M.F. A'Hearn, P. Feldman, J. Parker, K.D. Retherford, H.A. Weaver, I.P. Wright, The Rosetta campaign to detect an exosphere at Lutetia, Planetary and Space Science, Volume 66, Issue 1, 2012, Pages 165-172, ISSN 0032-0633, <a href="https://doi.org/10.1016/j.pss.2012.01.003">https://doi.org/10.1016/j.pss.2012.01.003</a>.</p>	
<p>PAPERS LED BY MAG</p>	
<p>K.-H. Glassmeier, I. Richter A. Diedrich, G. Musmann, U. Auster, U. Motschmann, A. Balogh, C. Carr, E. Cupido, A. Coates, M. Rother, K. Schwingenschuh, K. Szegoe, B. Tsurutani: RPC-MAG - The fluxgate magnetometer in the ROSETTA plasma consortium, Space Sci. Rev., 128, 649, 2007, doi: 10.1007/s11214-006-9114-x</p>	<p>MAG</p>
<p>C. Goetz, C. Koenders, I. Richter, K. Altwegg, J. Burch, C. Carr, E. Cupido, A. Eriksson, C. Güttler, P. Henri et al.: First detection of a diamagnetic cavity at comet 67P/Churyumov-Gerasimenko, A&amp;A, 588, 2016</p>	<p>MAG, LAP, IES, MIP, PIU</p>
<p>I. Richter, C. Koenders, H.U. Auster, D. Frühauff, C. Götz, P. Heinisch, C. Perschke, U. Motschmann, B. Stoll, K. Altwegg et al.: Observation of a new type of low frequency waves at comet 67P/Churyumov-Gerasimenko, Ann. Geophys., 33, 2015, doi:10.5194/angeo-33-1031-2015</p>	<p>MAG, PIU, ROMAP</p>
<p>I. Richter, H.U. Auster, G. Berghofer, C. Carr, E. Cupido, K.H. Fornacon, C. Goetz, P. Heinisch, C. Koenders, et al.: Two-point observations of low-frequency waves at 67P/ Churyumov-Gerasimenko during the descent of PHILAE: comparison of RPC-MAG and ROMAP, Ann. Geophys., 34, 2016</p>	<p>MAG, PIU, ROMAP</p>
<p>M. Volwerk, I. Richter, B. Tsurutani, C. Götz, K. Altwegg, T. Broiles, J. Burch, C. Carr, E. Cupido, M. Delva, M. Dósa, N. J. T. Edberg,</p>	<p>MAG, IES, LAP, MIP, ICA, PIU</p>

A. Eriksson, P. Henri, C. Koenders, J.-P. Lebreton, K. E. Mandt, H. Nilsson, A. Opitz, M. Rubin, K. Schwingenschuh, G. Stenberg Wieser, K. Szegő, C. Vallat, X. Vallieres, and K.-H. Glassmeier: Mass-loading, pile-up, and mirror-mode waves at comet 67P/Churyumov-Gerasimenko, <i>Ann. Geophys.</i> , 34, 2016, doi: 10.5194/angeo-34-1-2016	
C. Koenders, C. Perschke, C. Goetz, I. Richter, U. Motschmann, K.-H. Glassmeier: Low-frequency waves at comet 67P/Churyumov-Gerasimenko-Observations compared to numerical simulations, <i>A&amp;A</i> , 594, 2016	MAG, PIU
Glassmeier KH: Interaction of the solar wind with comets: a Rosetta perspective, <i>Philos Trans A Math Phys Eng Sci.</i> ;375(2097), 2017,doi: 10.1098/rsta.2016.0256	MAG, ICA, IES, PIU
C. Goetz, C. Koenders, K.C. Hansen, J. Burch, C. Carr, A. Eriksson, D. Frühauff, C. Güttler, P. Henri, H. Nilsson, et al.: Structure and Evolution of the Diamagnetic Cavity at Comet 67P/Churyumov-Gerasimenko, <i>MNRAS</i> , 2016	MAG, IES, LAP, ICA, PIU
C. Koenders, C. Goetz, I. Richter, U. Motschmann, K.-H. Glassmeier: Magnetic field pile-up and draping at intermediately active comets: results from comet 67P/Churyumov-Gerasimenko at 2.0 AU, <i>MNRAS</i> , 462, 2016	MAG, PIU
F. Plaschke, C. Goetz, M. Volwerk, I. Richter, D. Frühauff, Y. Narita, K.-H. Glassmeier and M. K. Dougherty; Fluxgate magnetometer offset vector determination by the 3D mirror mode method, <i>MNRAS</i> , 469, 2017, doi:10.1093/mnras/stx2532	MAG, PIU
M. Volwerk, G. Jones, T. Broiles, J. Burch, C. Carr, A. Coates, E. Cupido, M. Delva, N. Edberg, A. Eriksson, et al.: Current sheets in comet 67P/Churyumov-Gerasimenko's coma, <i>JGR</i> , 122, 2017	MAG, IES, LAP, PIU
Philip Heinisch, H.-U. Auster, I. Richter, G. Haerendel, I. Apathy, K.-H. Fornacon, E. Cupido, K.-H. Glassmeier: Joint two-point observations of LF-waves at 67P/Churyumov—Gerasimenko, <i>MNRAS</i> , 469, 2017, doi.org/10.1093/mnras/stx1175	MAG, PIU, ROMAP
Charlotte Goetz, Martin Volwerk, Ingo Richter, Karl-Heinz Glassmeier: Evolution of the magnetic field at comet	MAG, PIU

67P/Churyumov– Gerasimenko,MNRAS,469,2017, <a href="https://doi.org/10.1093/mnras/stx1570">doi.org/10.1093/mnras/stx1570</a>	
M. Volwerk, C. Goetz, I. Richter, M. Delva, K. Ostaszewski, K. Schwingenschuh, K.-H. Glassmeier: A tail like no other: RPC-MAG's view of Rosetta's tail excursion at comet 67P/Churyumov-Gerasimenko, A&A, 2017, <a href="https://doi.org/10.1051/0004-6361/201732198">doi.org/10.1051/0004-6361/201732198</a>	MAG, PIU
PAPERS LED BY ICA	
E. Behar, H. Nilsson, G. Stenberg Wieser, Z. Nemeth, T. W. Broiles, and I. Richter, Mass loading at 67P/Churyumov-Gerasimenko: A case study, Geophys. Res. Lett., 43, <a href="https://doi.org/10.1002/2015GL067436">doi:10.1002/2015GL067436</a> , 2016a	ICA, MAG
E. Behar, J. Lindkvist, H. Nilsson, M. Holmström, G. Stenberg-Wieser, R. Ramstad, C. Götz, Mass-loading of the solar wind at 67P/Churyumov-Gerasimenko-Observations and modeling, Astronomy & Astrophysics, 596, A42, <a href="https://doi.org/10.1051/0004-6361/201628797">doi: 10.1051/0004-6361/201628797</a> , 2016b	ICA, MAG
E. Behar, H. Nilsson, M. Alho, C. Goetz, B. Tsurutani, The birth and growth of a solar wind cavity around a comet - Rosetta observations, Monthly Not. Roy. Astr. Soc., 469, S396 – S403, 2017	ICA, MAG
Laura Berčič, Cometary ion dynamics observed in the close vicinity of comet 67P/CG during the intermediate activity period, Astronomy & Astrophysics, accepted, 2018	ICA, MAG
K. C. Hansen, K Altwegg, J-J Berthelier, A Bieler, N Biver, D Bockelée-Morvan, U Calmonte, F Capaccioni, MR Combi, J De Keyser, B Fiethe, N Fougere, SA Fuselier, S Gasc, TI Gombosi, Z Huang, L Le Roy, S Lee, H Nilsson, M Rubin, Y Shou, C Snodgrass, V Tennishev, G Toth, C-Y Tzou, C Simon Wedlund, Evolution of water production of 67P/Churyumov-Gerasimenko: An empirical model and a multi-instrument study, Monthly Not. Roy. Astr. Soc., <a href="https://doi.org/10.1093/mnras/stw2413">doi: 10.1093/mnras/stw2413</a> , 2016	ICA, Rosina

<p>G. Nicolaou, E. Behar, H. Nilsson, M. Wieser, M. Yamauchi, L. Berčič, G. Stenberg Wieser, Energy – angle dispersion of accelerated heavy ions at 67P/Churyumov-Gerasimenko: Implication in the mass-loading mechanism, Monthly Not. Roy. Astr. Soc., 469, S339-S345, 2017</p>	<p>ICA</p>
<p>Nilsson, H., G. Stenberg Wieser, E. Behar, C. Simon Wedlund, H. Gunell, M. Yamauchi, R. Lundin, S. Barabash, M. Wieser, C. Carr, E. Cupido, J. L Burch, A. Fedorov, J.-A. Sauvaud, H. Koskinen, E. Kallio, J.-P. Lebreton, A. Eriksson, N. Edberg, R. Goldstein, P. Henri, C. Koenders, P. Mokashi, Z. Nemeth, I. Richter, K. Szego, M. Volwerk, C. Vallat, M. Rubin, Birth of a comet magnetosphere: A spring of water ions, Science, 347, 6220, doi: 10.1126/science.aaa0571, 2015a</p>	<p>ICA, LAP</p>
<p>Nilsson, H., G. Stenberg Wieser, E. Behar, C. Simon Wedlund, E. Kallio, H. Gunell, N. Edberg, A. I. Eriksson, M. Yamauchi, C. Koenders, M. Wieser, R. Lundin, S. Barabash, K. Mandt, J. L. Burch, R. Goldstein, P. Mokashi, C. Carr, E. Cupido, P. T. Fox, K. Szego, Z. Nemeth, A. Fedorov, J.-A. Sauvaud, H. Koskinen, I. Richter, J.-P. Lebreton, P. Henri, M. Volwerk, C. Vallat, B. Geiger, Evolution of the ion environment of comet 67P/Churyumov-Gerasimenko – Observations between 3.6 and 2.0 AU, Astronomy and Astrophysics, <a href="http://dx.doi.org/10.1051/0004-6361/201526142">http://dx.doi.org/10.1051/0004-6361/201526142</a>, 2015b</p>	<p>ICA</p>
<p>Hans Nilsson, Gabriella Stenberg Wieser, Etienne Behar, Herbert Gunell, Martin Wieser, Marina Galand, Cyril Simon Wedlund, Markku Alho, Charlotte Goetz, Masatoshi Yamauchi, Pierre Henri, Elias Odelstad, Erik Vigren; Evolution of the ion environment of comet 67P during the Rosetta mission as seen by RPC-ICA, Monthly Notices of the Royal Astronomical Society, Volume 469, Issue Suppl_2, 21 July 2017, Pages S252–S261, <a href="https://doi.org/10.1093/mnras/stx1491">https://doi.org/10.1093/mnras/stx1491</a></p>	<p>ICA</p>
<p>Elias Odelstad, G. Stenberg-Wieser, M. Wieser, A. I. Eriksson, H. Nilsson and F. L. Johansson, Measurements of the electrostatic potential of Rosetta at comet 67P, Monthly Not. Roy. Astr. Soc., 469, S568-S581, 2017</p>	<p>ICA, LAP</p>

<p>C Simon Wedlund, E Kallio, M Alho, H Nilsson, G Stenberg Wieser, H Gunell, E Behar, J Pusa, G Gronoff, The atmosphere of comet 67P/CG diagnosed by charge-exchanged solar wind alpha particles, <i>Astronomy and Astrophysics</i>, 587, A154, doi: 10.1051/0004-6361/201527532, 2016</p>	<p>ICA</p>
<p>Gabriella Stenberg Wieser, Elias Odelstad, Martin Wieser, Hans Nilsson, Charlotte Goetz, Tomas Karlsson, Mats André, Leif Kalla, Anders I Eriksson, Georgios Nicolaou, Cyril Simon Wedlund, Ingo Richter, and Herbert Gunell, Investigating short time-scale variations in cometary ions around comet 67P, <i>Monthly Not. Roy. Astr. Soc.</i>, 469, S522-S534, 2017</p>	<p>ICA, MAG, LAP</p>
<p>PAPERS led by LAP</p>	
<p>M. André, E. Odelstad, D. B. Graham, A. I. Eriksson, T. Karlsson, G. Stenberg Wieser, E. Vigren, C. Norgren, F. L. Johansson, P. Henri, M. Rubin, I. Richter. Lower Hybrid Waves at Comet 67P/Churyumov-Gerasimenko. <i>Monthly Notices of the Royal Astronomical Society</i>, 469, S29-S38, 2017. <a href="https://doi.org/10.1093/mnras/stx868">doi:10.1093/mnras/stx868</a></p>	
<p>N. J. T. Edberg, A. I. Eriksson, U. Auster, S. Barabash, A. Bößwetter, C.M. Carr, S.W.H. Cowley, E. Cupido, M. Fränz, K.-H. Glassmeier, R. Goldstein, M. Lester, R. Lundin, R. Modolo, H. Nilsson, I. Richter, M. Samara, J.G. Trotignon. Simultaneous measurements of the Martian plasma environment by Rosetta and Mars Express. <i>Planetary and Space Science</i>, 57, 1085-1096, 2008. <a href="https://doi.org/10.1016/j.pss.2008.10.016">doi:10.1016/j.pss.2008.10.016</a></p>	
<p>N. Edberg, A. I. Eriksson, E. Odelstad, P. Henri, J.-P. Lebreton, S. Gasc, M. Rubin, M. André, R. Gill, E. P. G. Johansson, F. Johansson, E. Vigren, J. E. Wahlund, C. M. Carr, E. Cupido, K.-H. Glassmeier, R. Goldstein, C. Koenders, K. Mandt, Z. Nemeth, H. Nilsson, I. Richter, G. Stenberg Wieser, K. Szego, M. Volwerk.</p>	

<p>Spatial distribution of low-energy plasma around comet 67P/CG from Rosetta measurements.  <i>Geophysical Research Letters</i>, 42, 4263-4269, 2015.  <a href="https://doi.org/10.1002/2015GL064233">doi:10.1002/2015GL064233</a>  Preprint: <a href="https://arxiv.org/abs/1608.06745">arXiv:1608.06745</a></p>	
<p>A. I. Eriksson, R. Boström, R. Gill, L. Åhlén, S.-E. Jansson, J.-E. Wahlund, M. André, A. Mälkki, J. A. Holtet, B. Lybekk, A. Pedersen, L. G. Blomberg and the LAP team.  RPC-LAP: The Rosetta Langmuir probe instrument.  <i>Space Science Reviews</i>, 128, 729-744, 2007.  <a href="https://doi.org/10.1007/s11214-006-9003-3">doi:10.1007/s11214-006-9003-3</a></p>	
<p>A. I. Eriksson, I. A. D. Engelhardt, M. André, R. Boström, N. J. T. Edberg, F. L. Johansson, E. Odelstad, E. Vigren, J.-E. Wahlund, P. Henri, J.-P. Lebreton, W. J. Miloch, J. J. P. Paulsson, C. Simon Wedlund, L. Yang, T. Karlsson, R. Jarvinen, T. Broiles, K. Mandt, C. M. Carr, M. Galand, H. Nilsson, C. Norberg.  Cold and warm electrons at comet 67P.  <i>Astronomy and Astrophysics</i>, 605, A14, 2017.  <a href="https://doi.org/10.1051/0004-6361/201630159">doi:10.1051/0004-6361/201630159</a></p>	
<p>H Gunell, H Nilsson, M Hamrin, A Eriksson, E Odelstad, R Maggiolo, P Henri, X Vallieres, K Altwegg, C-Y Tzou, M Rubin, K-H Glassmeier, G Stenberg Wieser, C Simon Wedlund, J De Keyser, F Dhooghe, G Cessateur, A Gibbons.  Ion acoustic waves at comet 67P/Churyumov-Gerasimenko-Observations and computations.  <i>Astronomy and Astrophysics</i>, 600, A3, 2017.  <a href="https://doi.org/10.1051/0004-6361/201629801">doi:10.1051/0004-6361/201629801</a></p>	
<p>H. Gunell, C. Goetz, A. Eriksson, H. Nilsson, C. Simon Wedlund, P. Henri, R. Maggiolo, M. Hamrin, J. De Keyser, M. Rubin, G. Stenberg Wieser, G. Cessateur, F. Dhooghe, A. Gibbons.  Plasma waves confined to the diamagnetic cavity of comet 67P/Churyumov-Gerasimenko.  <i>Monthly Notices of the Royal Astronomical Society</i>, 469, S84-S92, 2017.  <a href="https://doi.org/10.1093/mnras/stx1134">doi:10.1093/mnras/stx1134</a></p>	

<p>F. L. Johansson, P. Henri, A. Eriksson, X. Vallieres, J.-P. Lebreton, C. Beghin, G. Wattieaux, E. Odelstad.          Simulations of the Rosetta spacecraft interaction with comet plasma. In <i>Proceedings of the 14th International Spacecraft Charging Technology Conference</i>, European Space Agency, 2016.</p>	
<p>F. L. Johansson, E. Odelstad, J. J. P. Paulsson, S. S. Harang, A. I Eriksson, T. Mannel, E. Vigren, N. J. T. Edberg, W. J. Miloch, C. Simon Wedlund, E. Thiemann, F. Eparvier, L. Andersson.          Rosetta photoelectron emission and solar ultraviolet flux at comet 67P.  <i>Monthly Notices of the Royal Astronomical Society</i>, 469, S626-S635, 2017.  <a href="https://doi.org/10.1093/mnras/stx2369">doi:10.1093/mnras/stx2369</a>          140</p>	
<p>T. Karlsson, A. I. Eriksson, E. Odelstad, M. André, G. Dickeli, K.-H. Glassmeier, A. Kullen, P.-A. Lindqvist, H. Nilsson, I. Richter.          Rosetta measurements of lower hybrid frequency range electric field oscillations in the plasma environment of comet 67P.  <i>Geophysical Research Letters</i>, 44, 2017.  <a href="https://doi.org/10.1002/2016GL072419">doi:10.1002/2016GL072419</a></p>	
<p>E. Odelstad, A. I. Eriksson, N. J. T. Edberg, F. Johansson, E. Vigren, M. André, C.-Y. Tzou, C. Carr, E. Cupido.          Evolution of the plasma environment of comet 67P from spacecraft potential measurements by the Rosetta Langmuir probe instrument.  <i>Geophysical Research Letters</i>, 42 , 10126-10134, 2015.  <a href="https://doi.org/10.1002/2015GL066599">doi:10.1002/2015GL066599</a></p>	
<p>E. Odelstad, G. Stenberg Wieser, M. Wieser, A. I Eriksson, H. Nilsson, F. L. Johansson.          Measurements of the electrostatic potential of Rosetta at comet 67P.  <i>Monthly Notices of the Royal Astronomical Society</i>, 469, S568-S581, 2017.  <a href="https://doi.org/10.1093/mnras/stx2232">doi:10.1093/mnras/stx2232</a>  <a href="https://arxiv.org/abs/1708.08803">https://arxiv.org/abs/1708.08803</a></p>	

<p>A. Sjögren, A. I. Eriksson and C. M. Cully. Simulation of potential measurements around a photoemitting spacecraft in a flowing plasma <i>IEEE Transactions on Plasma Science</i>, 40, 1257-1261, 2012. <a href="https://doi.org/10.1109/TPS.2012.2186616">doi:10.1109/TPS.2012.2186616</a></p>	
<p>E. Vigren, K. Altwegg, N. J. T. Edberg, A. I. Eriksson, M. Galand, P. Henri, F. Johansson, E. Odelstad, C.-Y. Tzou, X. Vallières. Model-Observation Comparisons of Electron Number Densities in the Coma of 67P/Churyumov-Gerasimenko during January 2015. <i>Astronomical Journal</i>, 152, 59, 2016. <a href="https://doi.org/10.3847/0004-6256/152/3/59">doi:10.3847/0004-6256/152/3/59</a></p>	
<p>E. Vigren, M. André, N. J. T. Edberg, I. A. D. Engelhardt, A. I. Eriksson, M. Galand, C. Goetz, P. Henri, K. Heritier, F. L. Johansson, H. Nilsson, E. Odelstad, M. Rubin, G. Stenberg-Wieser, C.-Y. Tzou, X. Vallières. Effective ion speeds at ~200-250 km from comet 67P/Churyumov-Gerasimenko near perihelion. <i>Monthly Notices of the Royal Astronomical Society</i>, 469, S142-S148, 2017. <a href="https://doi.org/10.1093/mnras/stx1472">doi:10.1093/mnras/stx1472</a></p>	

PAPERS LED BY IES	
<p>Broiles, T. W., J. L. Burch, G. Clark, C. Koenders, E. Behar, R. Goldstein, S. A. Fuselier, K. E. Mandt, P. Mokashi, and M. Samara (2015). Rosetta observations of solar wind interaction with the comet 67P/Churyumov-Gerasimenko. <i>Astronomy &amp; Astrophysics</i>, 583, A21, doi: 10.1051/0004-6361/201526046.</p>	IES, PIU, MAG, ICA
<p>Burch, J. L., et al., (2007), The Ion and electron Sensor of the Rosetta plasma consortium, <i>Space Sci. Rev.</i>, 128 (1-4), 697-712, doi:10.1007/s11214-006-9002-4.</p>	IES, PIU

Burch, J. L., T. E. Cravens, K. Llera, R. Goldstein, P. Mokashi, C.-Y. Tzou, and T. Broiles (2015), Charge exchange in cometary coma: Discovery of H <sup>+</sup> ions in the solar wind close to comet 67P/Churyumov-Gerasimenko, <i>Geophys. Res. Lett.</i> , 42, 5125–5131, doi:10.1002/2015GL064504.	IES, PIU, ROSINA
Burch, J.L., et al., (2015) Observation of charged nanograins at comet 67P/Churyumov-Gerasimenko, <i>Geophys. Res. Lett.</i> , 42, 6575-6581, doi:10:1002/2015GL065177.	IES, PIU
Clark, G., et al. (2015), Suprathermal electron environment of comet 67P/Churyumov-Gerasimenko: Observations from the Rosetta Ion and Electron Sensor, <i>Astron. Astrophys.</i> , 583, A24, doi:10.1051/0004-6361/201526351.	IES, MAG, ROSINA, PIU
Goldstein, R. et al. (2015). The Rosetta Ion and Electron Sensor (IES) measurement of the development of pickup ions from comet 67P/Churyumov-Gerasimenko, <i>Geophys. Res. Lett.</i> , 42, 3093–3099, doi: 10.1002/2015GL063939.	IES, ROSINA, PIU
Goldstein, R. et al. (2017). Two years of solar wind and pickup ion measurements at Comet 67P/Churyumov-Gerasimenko, <i>MNRAS</i> 469, S262–S267, doi:10.1093/mnras/stx1571.	IES, PIU
Madanian, H., et al., (2016), Suprathermal electrons near the nucleus of comet 67P/Churyumov-Gerasimenko at 3 AU: Model comparisons with Rosetta data, <i>J. Geophys. Res. Space Physics</i> , 121, doi:10.1002/2016JA022610.	IES, MAG, ROSINA
Madanian, H. et al., (2017), Plasma environment around comet 67P/Churyumov-Gerasimenko at perihelion: Model comparison with Rosetta data, <i>Astrophysical J.</i> , 153:30, doi:10.3847/1538-3881/153/1/30.	IES, MAG, ROSINA, PIU
Mandt, K. E., et al., RPC observation of the development and evolution of plasma interaction boundaries at 67P/Churyumov-Gerasimenko, <i>MNRAS</i> , 2016, 462, S9, doi:10.1093/mnras/stw1736	IES, ICA, MAG, ROSINA, PIU

PAPERS LED BY MIP or KEY PAPERS PRESENTING MIP DATASET	
Trotignon, J.-G., J. L. Michau, D. Lagoutte, M. Chabassière, G. Chalumeau, F. Colin, P. M. E. Décréau, J. Geiswiller, P. Gille, R. Grard, T. Hachemi, M. Hamelin, A. Eriksson, H. Laakso, J. P. Lebreton, C. Mazelle, O. Randriamboarison, W. Schmidt, A. Smit, U. Telljohann, P. Zamora, RPC-MIP: the Mutual Impedance Probe of the Rosetta Plasma Consortium, <i>Space Science Reviews</i> , 128, 713-728, doi: 10.1007/s11214-006-9005-1.	MIP
Gilet, Henri, Wattieaux, Cilibrasi and Beghin, Electrostatic potential radiated by a pulsating charge in a two-electron temperature plasma, <i>Radio Science</i> , 52, 1432 (2017)	MIP
Henri et al., Diamagnetic region(s): Structure of the Unmagnetised Plasma around Comet 67P/CG, <i>Mon. Not. R. Astron. Soc.</i> , 469, 372 (2017)	MIP, MAG
Hajra et al., Impact of a cometary outburst on its ionosphere: Rosetta Plasma Consortium observations of the comet 67P/CG outburst on 19 February 2016, <i>Astronomy and Astrophysics</i> , 607, A34 (2017).	MIP, LAP, MAG, IES
Héritier et al., Vertical structure of the near-surface ionosphere of comet 67P probed by Rosetta: the birth of a cometary ionosphere, <i>Mon. Not. R. Astron. Soc.</i> , 469, 118 (2017)	MIP, LAP, IES
Galand et al., Ionospheric plasma of comet 67P probed by Rosetta at 3 au from the Sun, <i>Mon. Not. R. Astron. Soc.</i> , 462, 331 (2016)	MIP, LAP, IES

<p>Grün et al., The 2016 Feb 19 outburst of comet 67P/CG: an ESA Rosetta multi-instrument study, <i>MNRAS</i>, 462, 220 (2016)</p>	<p>MIP, LAP, IES, MAG</p>
<p>Vigren et al., Model-observations Comparisons of Electron Number Densities in the Coma of 67P/Churyumov-Gerasimenko during January 2015, <i>The Astronomical Journal</i>, 152, 59, 2016.</p>	<p>LAP, MIP</p>
<p>Gunell et al., Plasma waves confined to the diamagnetic cavity of comet 67P/Churyumov-Gerasimenko. <i>Mon. Not. R. Astron. Soc.</i>, 469, 84, (2017)</p>	<p>LAP, ICA, MIP</p>
<p>Gunell et al.; Ion acoustic waves at comet 67P/Churyumov-Gerasimenko-Observations and computations. <i>Astronomy and Astrophysics</i>, 600, A3 (2017)</p>	<p>LAP, ICA, MIP</p>
<p>André et al., Lower Hybrid Waves at Comet 67P/Churyumov-Gerasimenko. <i>Mon. Not. R. Astron. Soc.</i>, 469, S29 (2017)</p>	<p>LAP, MIP</p>
<p>Edberg et al., Solar wind interaction with comet 67P: Impacts of corotating interaction regions, <i>Journal of Geophysical Research (Space Physics)</i>, 121, 949 (2016)</p>	<p>LAP, MIP, MAG, IES, ICA</p>
<p>Edberg et al., Spatial distribution of low-energy plasma around comet 67P/CG from Rosetta measurements, <i>Geophysical Research Letters</i>, 42, 4263 (2015)</p>	<p>LAP, MIP</p>

Edberg et al., CME impact on comet 67P/CG, <i>MNRAS</i> , 462, S45 (2016)	LAP, MIP, MAG, IES, ICA
---	-------------------------

=====

**SCHEDULE: All teams have agreed to the timetable**

<b>Schedule for the RPC Science User Guide</b>	
<b>Action Items</b>	<b>Deadline</b>
Input from all RPC teams regarding all sections [except 3 &, if not relevant, 6] - Hard, final deadline for RPC-IES input	Jan 31, 2018
<b>First version of the guide to deliver to ESA (Version 1)</b>	<b>April 15, 2018</b>
<b>Updated input from all RPC teams</b>	<b>June 30, 2018</b>
<b>End of IES funding: End of contribution</b>	<b>Sept 2018</b>
<b>Updated version of the guide to deliver to ESA (Version 2)</b>	<b>Aug 31, 2018</b>
<b>Updated input from all RPC teams</b>	<b>Nov 30, 2018</b>
<b>Final updated input from all RPC teams</b>	<b>April 15, 2019</b>
<b>Final version of the guide to provide to ESA (Final)</b>	<b>May 31, 2019</b>